ISBN 978-82-326-2964-0 (printed ver.)
ISBN 978-82-326-2965-7 (electronic ver.)
ISSN 1503-8181

Doctoral theses at NTNU, 2018:87

Erlend Liavåg Grotle

THERMODYNAMIC RESPONSE ENHANCED BY SLOSHING IN MARINE LNG FUEL TANKS

Experimental Work and Numerical Modelling

Erlend Liavåg Grotle

Doctoral thesis

Doctoral theses at NTNU, 2018:87

NTNU
Norwegian University of Science and Technology
Thesis for the Degree of
Philosophiae Doctor
Faculty of Engineering
Department of Ocean Operations and Civil Engineering

NTNU
Norwegian University of Science and Technology

NTNU

NTNU
Norwegian University of Science and Technology

Erlend Liavåg Grotle

THERMODYNAMIC RESPONSE ENHANCED BY SLOSHING IN MARINE LNG FUEL TANKS

Experimental Work and Numerical Modelling

Thesis for the Degree of Philosophiae Doctor

Trondheim, April 2018

Norwegian University of Science and Technology
Faculty of Engineering
Department of Ocean Operations and Civil Engineering

NTNU
Norwegian University of
Science and Technology

NTNU
Norwegian University of Science and Technology

Thesis for the Degree of Philosophiae Doctor

Faculty of Engineering
Department of Ocean Operations and Civil Engineering

ISBN 978-82-326-2964-0 (printed ver.)
ISBN 978-82-326-2965-7 (electronic ver.)
ISSN 1503-8181

Doctoral theses at NTNU, 2018:87

Printed by NTNU Grafisk senter

Abstract

This thesis presents studies of sloshing and how it influences thermodynamic conditions in liquefied natural gas (LNG) fuel tanks. Liquid in a moving tank mixes more efficiently with the gas, which condenses and is followed by a drop in pressure. This issue is relevant for the operation of LNG-fuelled vessels, where the system pressure may drop rapidly under severe motion. To compensate for the pressure loss, it may become necessary to derate the engines, or, in the worst case, perform a complete shutdown of the gas-fuel system. The long-term objective of the research is to improve the operational reliability of LNG-fuelled vessels by performing design improvements or operational measures.

LNG has become increasingly popular as a marine fuel due to its low emissions compared to those from conventional fuels like heavy fuel oil (HFO) and marine diesel oil (MDO). Low-pressure LNG fuel systems are designed similarly to land-based storage facilities. The storage tanks are vacuum-insulated and pressurised such that heat ingress is minimal. But when the tank is pressurised, the liquid may be significantly colder relative to the saturated condition. The thermal equilibrium is controlled in the short term by the liquid due to its large mass. The sloshing enhances the internal energy transfer, and the final state corresponds to a state that is closer to the initial liquid temperature.

This research is based on experimental work, analysis, modelling, and simulations. An experimental facility was designed and constructed, experimental tests were conducted separately, with a transparent tank for hydrodynamic studies and a pressurised steel tank for analysis of the thermodynamic response. Hydrodynamic sloshing tests were conducted with both rectangular and cylindrical tanks. Computational fluid dynamics (CFD) simulations of sloshing hydrodynamics were carried out with both tank geometries with the aim of replacing the hydrodynamic experiments to investigate any tank shape, inner structure, or motion. The resulting sloshing regimes were categorized and used systematically when preparing tests involving the thermodynamic response. Experiments with a pressurized steel

tank were conducted using both liquid nitrogen (LIN) and water. A theoretical framework was developed and implemented into a lumped capacity model. The model provides a good starting point for development of correlations between motion parameters and the enhanced heat transfer. It can also be combined with other submodels into a system model.

CFD simulations were found to represent sloshing with acceptable accuracy. New sloshing characteristics inside LNG fuel tanks are described. The thermodynamic response is influenced significantly by the severity of the sloshing. The final state depends on the initial liquid temperature and tank pressure, but the time to reach the final state depends on the sloshing intensity. The largest pressure drop rate occurs close to the primary resonance, $f/f_{1,0} = 1$. The PBU power needed to maintain the pressure was estimated from the measured pressure. It corresponds well with the PBU power used in the experiments. An existing CFD solver was modified to take into account the transport of thermal energy. The pressure drop was predicted with this model, and the result was found to correspond well with the experimental results for resonant sloshing. A case study is presented in which anticipated motion of a full-scale ship were used to simulate sloshing inside the LNG fuel tank. The L/D ratio is found to have a prominent effect on the sloshing, even at low frequencies.

Acknowledgements

A special thanks goes to my main supervisor, Vilmar Æsøy. He always takes great responsibility for his students, and no less with me. Completing this thesis would not have been possible without his support. I hope that in the future Vilmar and the other employees at the Institute of Ocean Operations and Civil Engineering will allow the students to become even more dedicated by combining hands-on work in the labs with theoretical work. This approach has great learning value.

Thanks also to Eilif Pedersen at the Department of Marine Technology at Tyholt. Eilif was my main supervisor until the merger of the Norwegian University of Science and Technology and the Aalesund University College. I had many good conversations with him early in the project. He is a great guy with a lot of knowledge. Many thanks to Hans Bihs and his team for supporting me with the analysis performed with REEF3D. Hans also deserves credit for helping me publish my first journal article. I also received great support from Erling Næss at the Department of Energy and Process Engineering by participating in his PhD course and also through our later conversations. Thanks also to Tor Ytrehus for sharing his knowledge about multiphase flow.

Thanks to all of the staff at the Department of Ocean Operations and Civil Engineering (formerly the Department of Maritime Operations and Technology) at NTNU in Ålesund. Special thanks to Andrè Tranvåg and his apprentices for their outstanding support in designing and building the experimental facility. I am sorry that I filled up the lab with so many tanks of different shapes and sizes. Thanks to Houxiang Zhang for reading the manuscript and providing useful feedback.

This work would not have been possible without my family and friends. Thanks to my dad for taking care of me at Lerstad, thanks to my mother and Pea for taking care of kids, and my brother for the mental support.

Nomenclature

Abbreviations

CFD	computational fluid dynamics
COG	center of gravity
ESD	emergency shutdown
FDM	finite-difference method
FVM	finite-volume method
HFO	heavy fuel oil
IMO	International Maritime Organization
LIN	liquefied nitrogen
LNG	liquefied natural gas
MDO	marine diesel oil
PBU	pressure build up unit
PSD	process shutdown
PVT	pressure-volume-temperature
RAO	response amplitude operator
RO	research objective
RPM	rotations per minute
RQ	research question
US	ultra-sonic
VOF	volume of fluid

List of Symbols

α	volume fraction
Δ	difference
η	free-surface elevation $[m]$
η_a	motion amplitudes $[m]$
ϕ	scalar
ρ	density $[kg/m^3]$

σ_0	wave circular frequency $[rad/s]$
σ_e	encounter frequency $[rad/s]$
θ	angle $[degrees]$
ν	kinematic viscosity $[m^2/s]$
A	area $[m^2]$; motion amplitude $[degrees]$; wave amplitude $[m]$
B	tank breadth $[m]$
CO_2	carbon dioxide
c_v	specific heat capacity @ constant volume $[J/kg \cdot K]$
c_p	specific heat capacity @ constant pressure $[J/kg \cdot K]$
D	diameter $[m]$
E	energy $[J]$
f	frequency $[Hz]$
$f_{1,0}$	natural frequency of the first mode $[Hz]$
g	gravity acceleration $[m/s^2]$
H	tank height $[m]$
h	filling depth $[m]$
h_{fg}	specific enthalpy of formation $[J/kg]$
h_L	liquid side heat transfer coefficient $[W/m^2 \cdot K]$
k	thermal conductivity $[W/m \cdot K]$
L	length $[m]$
L_s	length of crank arm; cylindrical length of tank $[m]$
m	mass $[kg]$
$\dot{m}$	mass flow $[kg/s]$
$\dot{m}''$	mass flux $[kg/s \cdot m^2]$
NO_2	nitrogen dioxide
NO_x	nitrogen oxides
P	pressure $[Pa]$
Pr	Prandtl number
Q	heat energy $[J]$
$\dot{Q}$	heat flow $[W]$
$\dot{Q}''$	heat flux $[W/m^2]$
R	crank radius $[m]$
R_k	crown radius $[m]$
r	evaporation constant $[1/s]$
S	wave energy spectrum $[m^2 \cdot s]$
s	location of sensor $[m]$
SO_x	sulphur oxides
T	temperature $[^\circ C]$, $[K]$
T	period $[s]$
T_{10}	natural period of the first mode $[s]$

t	time $[s]$
$t_{\Delta P}$	time from maximum to minimum pressure $[s]$
U	internal energy $[J]$; velocity $[m/s]$
u	specific internal energy $[J/kg]$
W	work $[J]$
x	spatial coordinate $[m]$

Subscripts

0	initial
abs	absolute
c; $cond.$	condensation
e	encounter
$eff.$	effective
G	gas
i	interface; point *i*
j	wave component *j*
k	kinetic
L	liquid
m	motor
p	potential
s	ship
sat	saturated
$syst.$	system
t	tank; turbulence
$vap.$	vapour
w	wall

Contents

Chapter 1

Introduction

1.1 Background

The use of liquefied natural gas (LNG) as a marine fuel is mainly motivated by its reduced emissions compared to those from conventional fuels like heavy fuel oil (HFO) and marine diesel oil (MDO). The NO_x emissions may be reduced as much as 90% and the CO_2 emissions by as much as 25% ([1], [10]). There is no sulphur content in natural gas so, its SO_x emissions are zero. Financial support from sources like the Norwegian NO_x fund, has resulted in an increasing number of LNG-fuelled ships in operation over the past 15-20 years. The growing demand for energy, creating expectations of lower gas prices compared to oil prices has also been a driving factor for the choice of LNG as a marine fuel.

The main challenges of using LNG as a fuel have traditionally been related to infrastructure, safety issues, and investment costs [2]. Infrastructure has improved significantly in emission-controlled areas, like the Norwegian coast. The investment costs for LNG fuel systems and engines are higher than those for conventional fuels, but may be reduced with subsidies, as mentioned. Challenges related to handling and operations are *bunkering and fuel transfer operations*, *transient load conditions* such as manoeuvring, and *operations in heavy sea states* [15]. Natural gas has a boiling point of -163 [$^{\circ}C$] at standard atmospheric conditions, which makes it a cryogenic liquid. Handling the cold liquid requires additional safety measures, and bunkering of LNG is subject to strict procedures. It starts with purging the pipelines, checking for leakage, and cooling the piping. Both tank bottom fill and spraying from the top of the tank are done to control pressure under bunkering. Successful control of pressure and efficient filling depends on the temperature of the LNG.

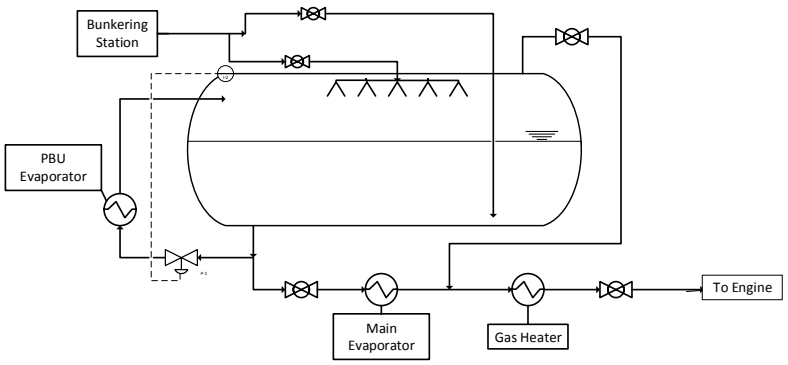

Figure 1.1: Low-pressure LNG fuel system.

Storing natural gas in liquid form requires very high pressure, insulated tanks, or a combination of the two. LNG storage tanks are roughly divided into vacuum insulated pressure tanks (IMO C-type) or atmospheric pressure membrane tanks (A-type). A significant difference between these types of tanks is that the C-type may be pressurized by maximum 10 [barg], while the membrane tanks are atmospheric. There is no need for a pump in pressurized tanks, because the pressure acts as the driving force to transport the fuel. A disadvantage of pressurized tanks is the requirement of a specific geometry due to the possibility of overpressure. The tanks must be cylindrical with spherical heads. This makes their design and placement onboard quite limited. The tanks may be placed longitudinally, transversally, or even vertically.

The system philosophy for *low-pressure fuel systems* is similar to that for land-based storage of LNG. The gas volume increases as the tank is emptied, and a *pressure build-up unit* vaporizes liquid into gas in a closed loop to maintain the pressure (Fig. 1.1). The tank pressure acts as the driving force to create flow through the fuel system, into the gas regulating unit, and finally into the engines. The mechanical pump is thus replaced by the supply of heat. The gas engines can be operated only with sufficient pressure in the fuel system. The consequence of too low pressure may be process- or emergency shutdown (PSD/ESD).

1.2 Problem Description

One major difference between land-based facilities and those for ships is the motion due to waves. Experience has shown that the tank pressure is sensitive to the liquid level, the LNG bunkering temperature, and the ship's motion. Chief engineers report a loss of more than 1 [bar] within seconds, depending on the conditions. As already explained, loss of pressure is an unwanted situation, with shutdown the worst consequence. The PBU is supposed to maintain the pressure as the tank is emptied, but is not dimensioned for the pressure collapse due to sloshing.

The only way to reduce pressure inside the tank is to remove the mass, increase the volume, or reduce the temperature. Considering the entire tank as a closed thermodynamic system, only heat input is possible becuase the ambient temperature is always higher than the temperature inside the tank. The only cooling source is the liquid, which has a lower temperature relative to the gas. The existing literature suggests that the pressure drop is caused by condensation of gas due to cooling by the liquid ([30], [26], [3], [27]). All of the aforementioned studies consider vertically aligned cylindrical tanks for aerospace applications, in which sloshing characteristics are well known ([21]).

The pressure in the fuel system is normally 5-7 [barg], and the liquid may be significantly colder relative to this pressure. This is illustrated in Fig. 1.2. The bunkered LNG temperature is lower than the saturated temperature determined by the operation pressure, such that $T_{0,L} - T_{sat}\left(P_{op}\right) < 0$. The approximate temperature profile after bunkering is represented by the blue curve in Fig. 1.3. The final equilibrium temperature after sloshing is illustrated by the stippled yellow line in Fig. 1.3. As the liquid is much more dense, it will dominate the process and the equilibrium temperature must be closer to the initial liquid temperature than the gas temperature. The pressure-temperature line in Fig. 1.2 represents the conditions at the interface. Excluding heat ingress, the final state depends solely on the desired tank pressure during operation and the bunkered LNG temperature.

This introduction should leave no doubt that the loss of pressure is an unwanted situation. It may seem obvious that the liquid cools the gas and that sloshing enhances this process. However, the detailed mechanisms are not well understood. It is our belief that understanding is required to remedy the problem in a sustainable way. It may be resolved by modification of the design, for example by installation of a cryogenic pump. However, this would increase maintenance costs. The installation of baffles dampens sloshing motion, but it is not known whether the baffles prevent pressure collapse due to mixing.

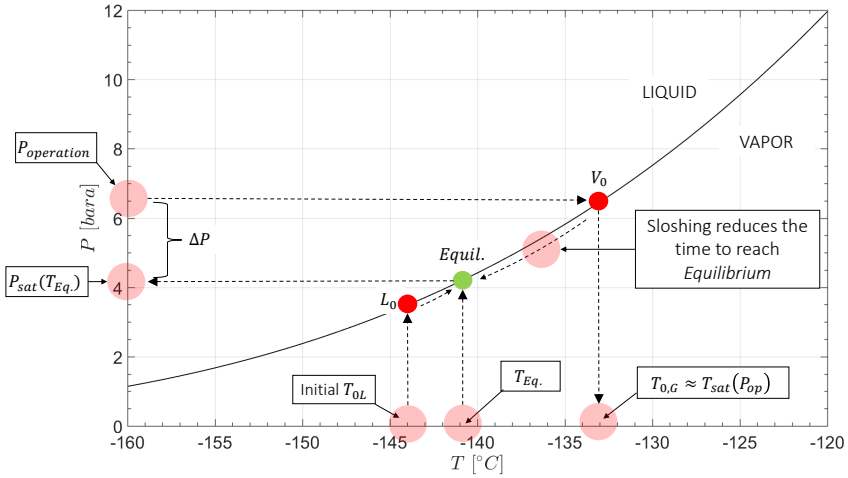

Figure 1.2: Methane coexistence curve and and explanation of the change of thermodynamic state. The p-T data was generated using REFPROP v9.1 [25].

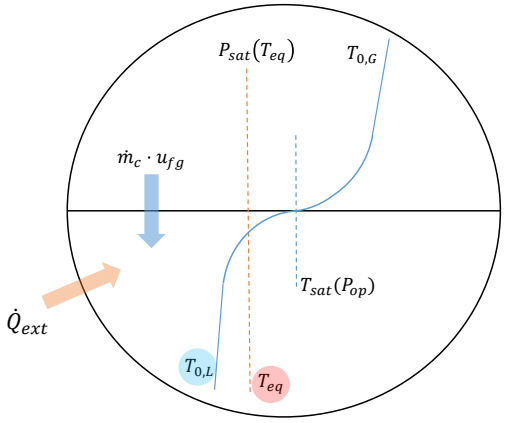

Figure 1.3: Heat transfer mechanisms in the tank. Internal mixing due to sloshing must lead to a final temperature, T_{eq}. The final pressure must correspond to the equilibrium saturation temperature.

If the internal heat transfer mechanisms were well understood, theories and models could be developed to estimate pressure drop, improve design, and map conditions that should be avoided during operation of the ship. Solving these aforementioned challenges would clearly be a contribution to improve the reliability of the ship's operability.

1.3 Research Questions

The main hypothesis in this work is that the pressure in the tank drops due to the condensation of gas. The liquid acts as a thermal reservoir to the gas and cools it. Sloshing enhances the transport of thermal energy and therefore reduces the time needed to reach temporary thermal equilibrium inside the tank. The detailed mechanisms are not known.

The introduction arises a number of research questions. These are formulated as follows:

RQ1: *Which research methods can be employed to study the influence of sloshing on the thermodynamic response?*

RQ2: *Can numerical software tools provide information about sloshing hydrodynamics in LNG fuel tanks?*

RQ3: *How does sloshing enhance the thermodynamic response, and which variables are important?*

RQ4: *Can the PBU power compensate for the sloshing-enhanced pressure loss?*

RQ5: *Does the thermodynamic response correlate with the tank motion?*

RQ6: *Is it possible to predict the thermodynamic response enhanced by sloshing using CFD?*

1.4 Objectives

The research is structured by formulating a set of objectives developed from the given research questions. The objectives are related to the contributions given at the end of the thesis.

The main objective of this thesis is to improve understanding of the mechanisms that lead to the rapid pressure loss experienced in fuel-gas supply systems onboard LNG-fuelled vessels. The long-term objective is to improve the operational reliability of LNG-fuelled ships through design and operational measures.

Considering the main objective, a set of sub-objectives are formulated. The following ones apply to this thesis:

RO1: *Develop research methods to perform studies of both hydrodynamic and thermodynamic responses due to sloshing.*

RO2: *Improve knowledge about sloshing hydrodynamics through experimental and numerical work, especially in LNG fuel tanks.*

RO3: *Study the thermodynamic response due to sloshing and find out which parameters are influencing the pressure drop.*

RO4: *Estimate the necessary PBU power.*

RO5: *Correlate the thermodynamic response with the tank motion.*

RO6: *Use CFD tools to predict the thermal response and provide the necessary input data to perform dynamic simulations based on correlations.*

1.5 Scope of Work

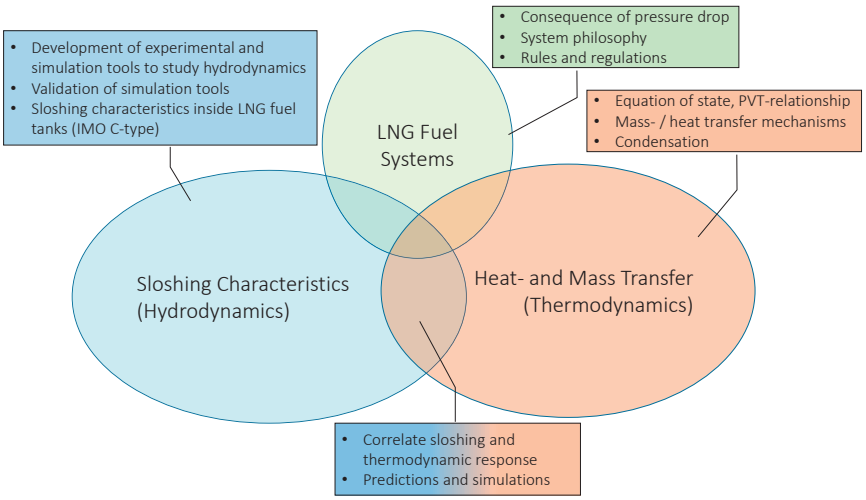

Figure 1.4: Scope of work and different fields of study relevant to the project.

The scope of work in this thesis is illustrated in Fig. 1.4. It consists of three individual fields of study: *Sloshing characteristics*, *heat- and mass transfer*, and *marine LNG fuel systems*. Each element constitutes a part of the scope domain. The essential part is where the different elements overlap. This area must be investigated as deeply as possible, which requires individual study of each of the three elements shown in Fig. 1.4.

The study of sloshing hydrodynamics has a long tradition in the maritime industry ([11], [21]). The typical concern is sloshing-induced forces and moments. Sloshing may be useful because it prevents destabilization of a ship by the application

of anti-roll tanks. Although these concerns are still important for LNG fuel tanks, they are of less importance in this thesis. They still need to be considered in the design and construction of LNG fuel tanks. The thermodynamic response seems to be related to typical variables that characterize the severity of the sloshing. One example is the excitation frequency and its proximity to the first mode of natural frequency, $f/f_{1,0}$. Few studies exist that deal with sloshing characteristics in LNG fuel tanks, so the hydrodynamic studies are also relevant.

Heat- and mass transfer is an essential part of this project. Condensation transforms gas into liquid. Energy may be transferred by direct contact between liquid and gas, via the tank walls, or a combination of the two ([35], [23]). The objective of the thesis is to investigate these mechanisms and how they are affected by sloshing. It is important to discover which of the variables are actually causing the pressure drop. Is it the change in internal energy, or is it the mass? Development of a theoretical framework has been done based on the energy conservation laws. This is needed to analyse experimental results and improve understanding of the heat- and mass transfer.

Relating sloshing with heat- and mass transfer is a fairly new approach. The physical mechanisms of sloshing can be visualized and studied qualitatively. Condensation may also be observed, but the mechanisms are more difficult to study, which makes measurement of thermodynamic variables like temperature and pressure necessary. Natural gas consists of several substances, the major one being methane ([28]). Methane is the lightest component with the lowest boiling point. The heavier components have been left out of this work because the methane content is greater than 90 $\%$. This means that methane will dominate the gas phase and also the region around the interface. The condensation process is therefore assumed to be entirely controlled by temperature gradients. No enrichment of other species is assumed to affect the process. It may be necessary to investigate the influence of other substances in future work.

Relevant variables in this study, and how they are assumed to influence the thermodynamic response, are presented in Fig 1.5. These were briefly mentioned in section 1.2. Blue boxes show variables that are assumed to influence the thermodynamic state indirectly by affecting the sloshing. The remaining boxes in yellow indicate variables that are assumed to influence the thermodynamic response directly.

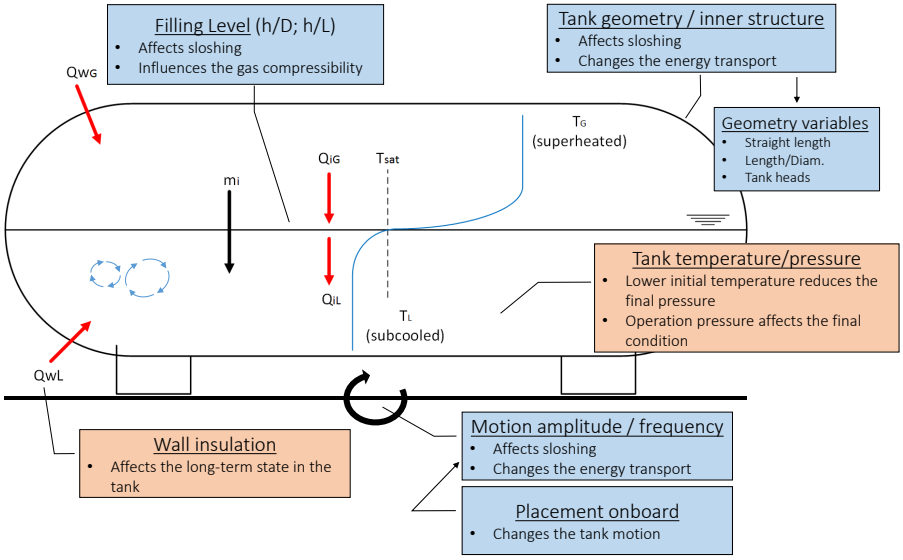

Figure 1.5: Variables that are relevant to the thermodynamic response, either directly or indirectly, by influencing sloshing.

1.6 Structure of the Thesis

The introduction in chapter 1 is divided into several sections, including background information and problem description. The first part should answer *why* this research has been performed. Research questions and objectives are pursued from the problem description, and the scope of work describes the fields of study relevant to the objectives.

The research approach is presented in chapter 2 and includes a description of the research methods. The research is based on experiments, analytical methods, and numerical simulations.

All relevant results are presented in chapter 3. The most important results have been selected from the papers. More details can be found in the publications, but there should be no need to look them up while reading the thesis. All of the papers are referenced in the text, and may be found in Appendix A. The objectives are also referenced in the results.

The research is summarized in chapter 4. It contains a list of the papers and an overview with keywords. This section also lists the main research contributions and relates them to the research objectives. Concluding remarks and suggestions for future work are given at the end of the chapter.

Chapter 2

Research Approach

The research methods used in this thesis are *analytical, experimental*, and *CFD simulations*. How they are applied is illustrated in Fig. 2.1. Data and observations are collected from the experimental work. Results are analysed, and theory is further developed. Models are implemented and simulation results are analysed, followed by changes in the experimental setup or in the models. Experimental data, especially the hydrodynamic tests, are compared with the CFD results for validation purposes.

A description of each individual research method is presented in the following.

2.1 Analytical Methods

The analytical methods conducted in the thesis consist mainly of analysis of experimental results and development of mathematical simulation models. The process of performing analytical work may be of equal importance to the final results. It should be performed in parallel with the experimental work to efficiently gather knowledge.

Analysis of experimental data begins with the collection and structuring of measurement data as well as comparing videos from experiments, CFD results, and measurements. Raw data from experiments are plotted with Microsoft Excel or Matlab. This gives an overview of the results. The data that contains relevant results are further analysed. The amount of data from experiments and simulations can be rather extensive. Several built-in functions have been employed for this purpose.

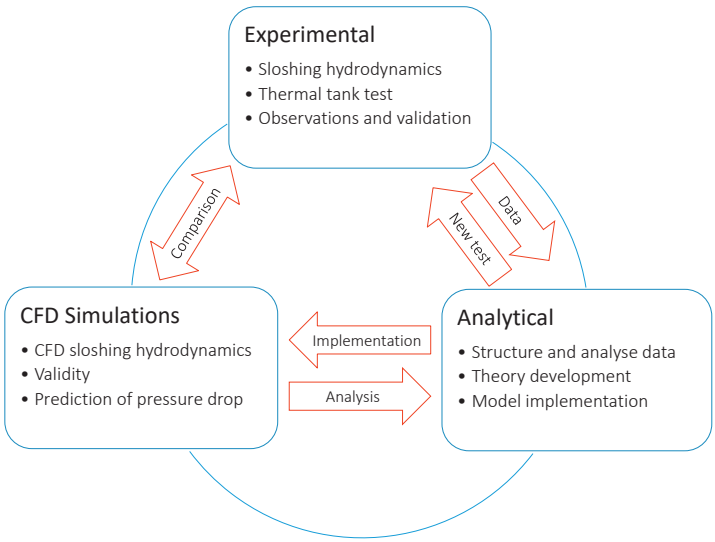

Figure 2.1: Research approach.

2.1.1 Theoretical framework

A theoretical framework was constructed, starting with the energy balance for a closed system. Equations have been derived from the basic theory, and the results are analysed together with experimental data. Simplifications and improvements of the theoretical framework depend on proper experimental results and analysis.

The energy balance for a closed system states that the total energy change of the system must equal the net heat and work transferred to the system. The system comprises the entire tank, and the energy balance reads [31]

$$\Delta E = \Delta U + \Delta E_k + \Delta E_p = \delta Q + \delta W. \tag{2.1}$$

The work term is usually split up into compression work and work transferred across the control volume border. Here it is assumed that all transferred work (tank excitation) equals the change of kinetic and potential energy, and transferred work does not influence the internal energy (compression work and friction). Eq. 2.1 is then simplified to

$$\Delta U_{syst.} = \delta Q. \tag{2.2}$$

Assumption 1: *There is no generation of internal energy due to friction.*

The internal energy is an extensive variable and may thus be divided into a contribution of each phase such that

$$\Delta U_L + \Delta U_G = \delta Q. \tag{2.3}$$

The external heat transfer, Q, certainly includes the heat transfer to the PBU. This equals the mass flow of condensed gas times the specific enthalpy of formation, such that

$$\delta Q_{PBU} = \Delta m_{PBU} \cdot h_{fg}. \tag{2.4}$$

Assuming that heat ingress is negligible and excluding the PBU heat for now, this gives us

$$\Delta U_L + \Delta U_G = \Delta(mu)_L + \Delta(mu)_G, \tag{2.5}$$

where $U = mu$ is absolute internal energy, mass, and specific internal energy respectively. Subscripts, L and G are liquid and gas, respectively.

Assumption 2: *Heat ingress is negligible during the sloshing event unless the PBU is active.*

The mass balance simply states that the change in mass of liquid must equal the change in mass of gas, such that

$$\Delta m_L + \Delta m_G = 0. \tag{2.6}$$

Separating the variables in Eq. 2.5 and using the differential notation gives us

$$m_L \cdot du_L + m_G \cdot du_G = dm_L \cdot (u_G - u_L). \tag{2.7}$$

By using the relation $du = c_v dT$ this can be further rewritten to

$$(c_v m \cdot dT)_L + (c_v m \cdot dT)_G = dm_L \cdot [u_{fg} + c_{v,G}(T_G - T_{sat}) - c_{v,L}(T_L - T_{sat})]. \tag{2.8}$$

Here $u_{fg} = u_g - u_f$ is the specific saturation internal energy. T_{sat} is the saturation temperature. c_v is the specific heat capacity.

Assumption 3: *The relation $du = c_v dT$ is valid for the liquid (incompressible substance) and the gas (ideal gas).*

The gas can in many cases be considered as saturated without any particular influence on the tank pressure. The superheating was found to be minor, or it had no influence on the pressure. At least for the experiments with the PBU this was found to be true, because the PBU power and residence time in the vaporizer are not enough to superheat the gas. Eq. 2.8 reduces to

$$c_{v,L} m_L \cdot \frac{dT_L}{dt} + c_{v,G} m_G \cdot \frac{dT_{sat}}{dt} \approx \dot{m}_L \left[u_{fg} - c_{v,L} \left(T_L - T_{sat} \right) \right], \tag{2.9}$$

where it is divided by dt to introduce the time rate of change. $\dot{m}_L$ is then the time rate of change of condensation mass.

Assumption 4: *The amount of superheated gas is assumed to be negligible relative to the subcooled liquid. The gas may therefore be assumed to be saturated without influencing the tank pressure.*

It has been found from analysis of experimental data and sensitivity analysis that the pressure is influenced mainly by the mass of gas. The simplest equation of state of the gas is the ideal gas law. Assuming constant gas volume, the time rate of change in pressure is given as

$$\frac{dP}{dt} = -\frac{P}{m_G} \frac{dm_L}{dt} + \frac{P}{T_G} \frac{dT_G}{dt}. \tag{2.10}$$

Assumption 5: *The gas volume is considered constant during the sloshing event. This is the same as excluding pressure-volume work, as mentioned initially.*

Supported by the results from simulations and sensitivity studies, the change in gas temperature has minor influence on the pressure. Thus,

$$\frac{dP}{dt} \approx -\frac{P}{m_G} \dot{m}_L. \tag{2.11}$$

The change in pressure results from the change in mass. This is true if assumption 4 is true.

Another variable difficult to model is the condensation mass. Existing literature ([13]) suggests that the condensation energy is balanced by the heat fluxes on each side of the gas-liquid interface (see P6 for more information). This can be expressed as

$$\dot{m}_L = \frac{\dot{Q}_{iG} + \dot{Q}_{iL}}{u_{fg}}, \tag{2.12}$$

where $\dot{Q}_{iG}$ and $\dot{Q}_{iL}$ [W] are the sensible heat transfer on each side of the interface and may also be expressed by Fourier's law of heat conduction. This is illustrated in Fig. 2.2.

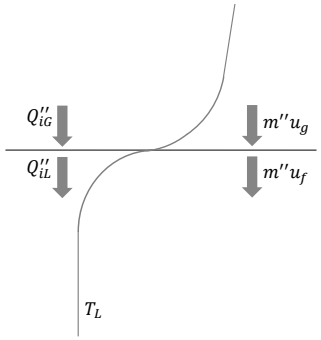

Figure 2.2: Energy balance at the liquid-gas interface.

One of the necessary conditions for condensation is the exchange of cold bulk and saturated liquid close to the interface. The energy transport is enhanced by sloshing. Considering assumption 4, the gas contribution to Eq. 2.12 is negligible, such that only the heat flux on the liquid side corresponds to the condensation energy.

A way to express the heat flow on the liquid side, $\dot{Q}_{iL}$, is by the use of Newton's cooling law, which states that the heat flux equals a convective heat transfer coefficient times the interface area and the temperature difference. This gives us

$$\dot{m}_L \cdot u_{fg} \approx \dot{Q}_{iL} \approx h_L A_i \left(T_L - T_{sat}\right), \tag{2.13}$$

where the liquid temperature, T_L, is the bulk temperature. The saturation temperature, T_{sat}, is given by the tank pressure. h_L is a heat transfer coefficient and A_i is the interface area. The results show that keeping the product $h_L \cdot A_i$ constant for a

specific motion frequency gives a fairly good representation of the thermodynamic response. The product is considered to be an averaged value. It is not clear at this time the contribution by each factor, if there are more factors, and how the factors are weighted. The expression in Eq. 2.12 is valid as an interface condition, but it is here considered to be an overall convective heat transfer coefficient. The heat flow $\dot{Q}_L$ represents the net sensible heat flow on the liquid side, which is enhanced by sloshing.

The theoretical framework is a conceptual approach simply applying Newton's law of cooling. The condensation mass flow rate must be balanced by the renewal of cold liquid close to the interface.

2.1.2 Implementation of a lumped capacity model

The analytical method outlined in the previous section can easily be solved numerically. This has been helpful when analysing experimental results. The model development is simple, but provides us with many answers.

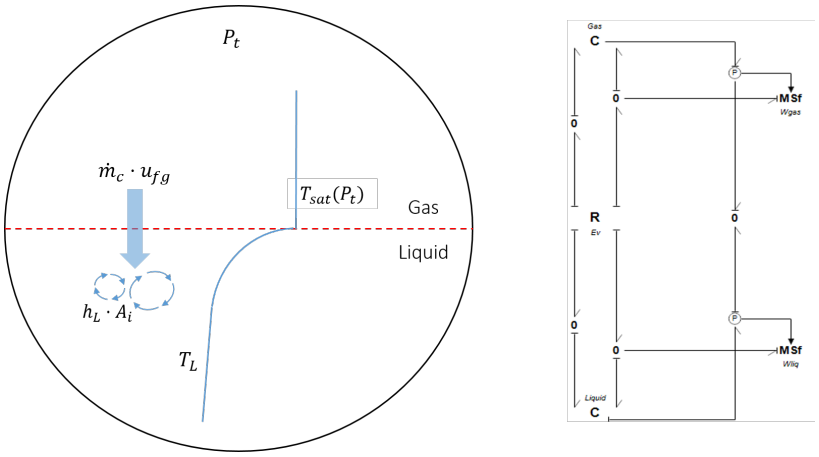

Figure 2.3: Illustration of the lumped capacity model. Physical assumptions to the left and bond graph model to the right (from paper 6).

The outline of the modelling approach is given here, while the results are presented in chapter 3. The following procedure was implemented in Matlab, solving the equations by performing simple numerical integration (see Fig. 2.3 for an illustration):

1. Set the constant $h_L \cdot A_i$.
2. Initialize variables like start temperature, pressure, and mass of liquid and

gas. The mean liquid temperature must be approximated. The gas temperature is ignored here.

3. Calculate the saturation temperature from the present tank pressure, $T_{sat}\,(P_t)$ (it may be necessary to consider air content).

4. Find the specific internal energy of formation, u_{fg}, from P_t.

5. Calculate $\dot{m}_c \cdot u_{fg} = h_L \cdot A_i \cdot (T_L - T_{sat})$.

6. Perform a numerical time integration to get the new mass of liquid and gas, such that $m_G \approx \dot{m}_c \cdot \Delta t + m_{G,0}$.

7. Calculate the new pressure, $P_t = P_0 \cdot exp\left[log_n\left(\frac{m_{gas}}{m_{gas,0}}\right)\right]$.

8. Find the new saturation temperature, $T_{sat}\,(P_t)$, and calculate $\frac{dT_{sat}}{dt}$ numerically.

9. Calculate the new liquid temperature numerically with Eq. 2.9.

So far, the model has only been used to tune the results to make a best fit with the experiments. Hence, the model cannot predict the thermodynamic response at the present. The model gives us unknown variables that otherwise must have been calculated by a steady-state approach. Among them is the constant $h_L \cdot A_i$. The model may be used to develop correlations between $f/f_{1,0}$ and $h_L \cdot A_i$ by performing a best-fit approximation with the experiments. The model could later be combined with other system models to represent an independent thermodynamic sloshing model.

2.2 Experimental Methods

As we are faced with a complex physical problem in which the mechanisms are not well understood, there is a need to perform experimental work. This is the most realistic method by which to study these mechanisms, albeit at model scale. The drawback is the difficulty of measuring and tracking all relevant variables, like temperature and velocity profiles. It has not been possible to visualise the mechanisms that take place because the test tank is made of steel. The experiments are therefore divided into two parts: one main test to investigate hydrodynamics in a transparent tank, and a second test to study the thermodynamic response. Observations are possible only in the first case, while in the second case measurements of temperature and pressure are collected and analysed with no visibility. The experimental facility and procedures are presented in the following.

2.2.1 Experimental test rig

The experimental rig consists of a movable platform with one degree of freedom, as illustrated in Fig. 2.4. The tank rotates around the bottom centerplane of the tank in all tests, and the angle amplitude is constant and equal to 3 degrees. The motion is created by a crank mechanism driven by an electro motor. As the crank arm is long, $L_s >> R$, the angle of the platform is $\theta(t) \approx A \cdot sin\,(2\pi f \cdot t)$, where A is the amplitude, f is the frequency, and t is time. How the angle varies in time is shown in Fig. 2.5. The frequency is controlled by the speed of the electro motor. A gear reduces the rotational speed by 1:50 such that $f = RPM_m/60/50$. Sensors are installed to measure both the motion angle and the force on the crank arm, L_s.

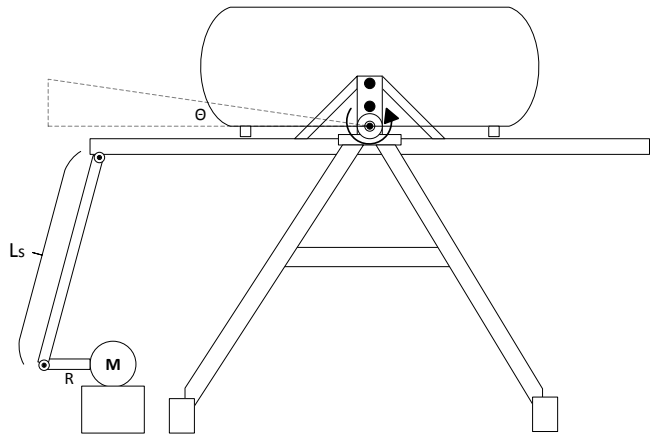

Figure 2.4: The movable platform and tank setup.

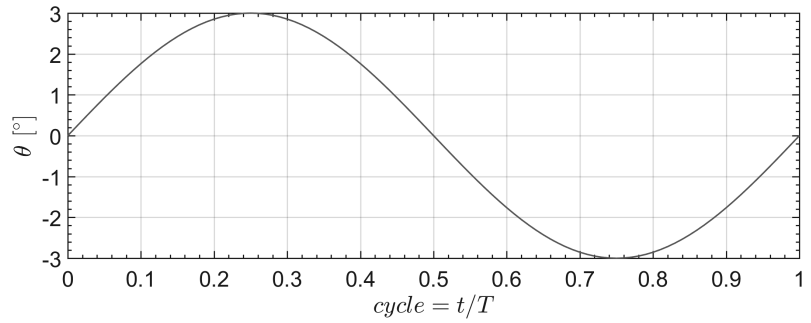

Figure 2.5: Motion angle of the platform during one cycle. t is time [s] and T is motion period, equal to $1/f$ (here $T = 1$ [s]).

2.2.2 Tank geometries

Both rectangular and cylindrical tanks were investigated experimentally and with simulations. The purpose of testing with the rectangular tank is to validate CFD simulations and investigate the limitations of the simulation models. They are also used to test the experimental facility and to check the instruments. Sloshing inside a cylindrical tank geometry is almost unexplored, and tests have been conducted to investigate the sloshing characteristics and prepare the thermal experiments.

The rectangular tank geometry is shown in Fig. 2.6. The ultrasonic sensor is located $S = 408$ [mm] from the left towards the middle as shown.

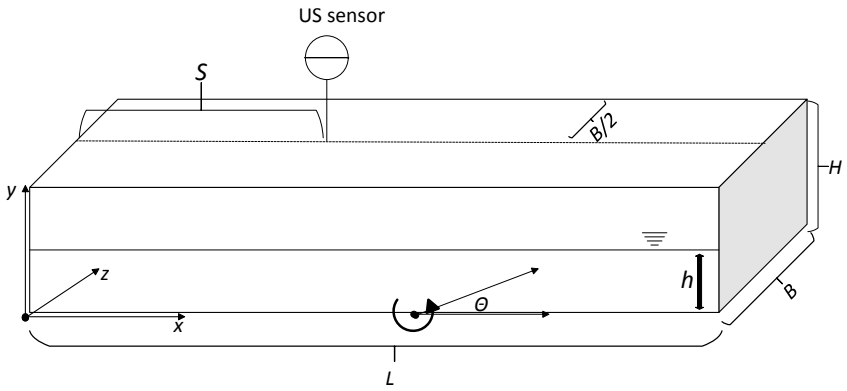

Figure 2.6: Rectangular tank geometry.

For more information about the setup of the rectangular tank tests, the reader is referred to paper 4 ([18]).

The model-scaled LNG fuel tank has been horizontally aligned in all tests. The geometry consists of a straight cylindrical section and 2:1 semi-elliptic heads, which are commonly installed on pressure tanks. Fig. 2.7 shows the geometrical definitions of the tank heads. The transparent tank consists of a straight plastic pipe, as shown in Fig. 2.8. The tank heads were constructed by the use of casting made of polyurethane, and the plastic glass was constructed by vacuum-pulling techniques. The geometrical properties are the same as those of the steel tank, shown in Fig. 2.10.

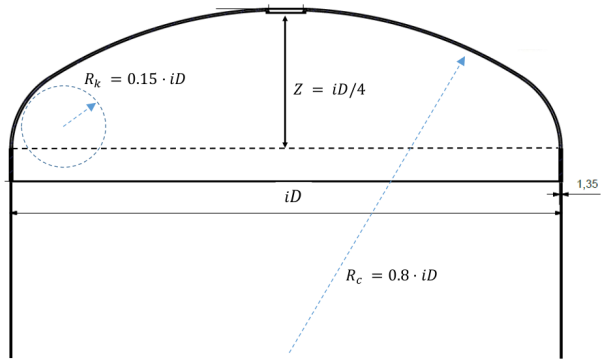

Figure 2.7: Semi-elliptic tank heads.

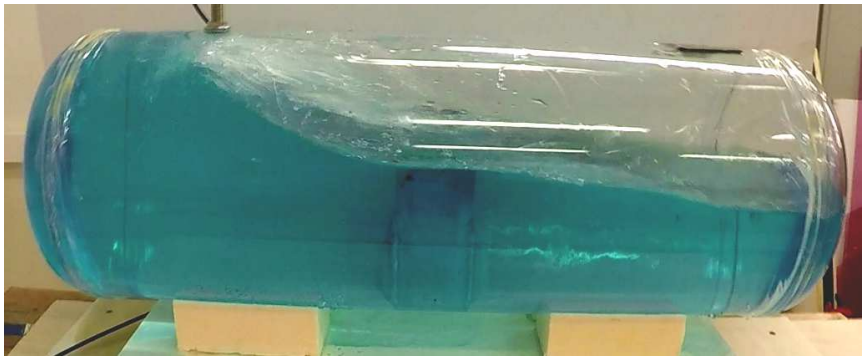

Figure 2.8: Transparent tank used in hydrodynamic studies.

2.2.3 Sloshing hydrodynamics

Experiments involving sloshing hydrodynamics were performed to study sloshing characteristics and to validate CFD simulations. The transparent tanks provided information about the sloshing characteristics, which is necessary to decide the test parameters for the thermal tank tests.

To perform a comparison between the simulations and the experiments, the free-surface elevation was measured with an ultrasonic sensor, type Sick UM12. The accuracy of this sensor is $\pm 1\%$ with a repeatability of $\pm 0.15\%$. It was mounted on the top of the straight cylindrical section. Videos of all the sloshing tests were recorded using a GoPro Hero4 camera. The free-surface elevation was possible to measure only when the liquid depth was low, because the sensor does not work in

contact with water. The location of the sensor is 0.122 [m] from the left-hand side of the straight cylindrical section (see Fig. 2.8).

The test sequence is described in Fig. 2.9. Preparation consists of making sure that the tank and platform are horizontal and that the crank arm is correctly adjusted. Sensors must be calibrated and standby. The test starts with the lowest filling depth, and the US sensor is employed to find the correct level. A ruler is used as additional assurance. The electro motor is prepared by setting the number of rotations and the frequency. The sensors and camera are then turned on. Once the sensor and the other equipment are ready, the electro motor may be started. It runs a prescribed number of rounds. When it stops, the waves must cease before the sensors are turned off. Sometimes it is unnecessary to film the entire sequence, just a part of the sloshing event.

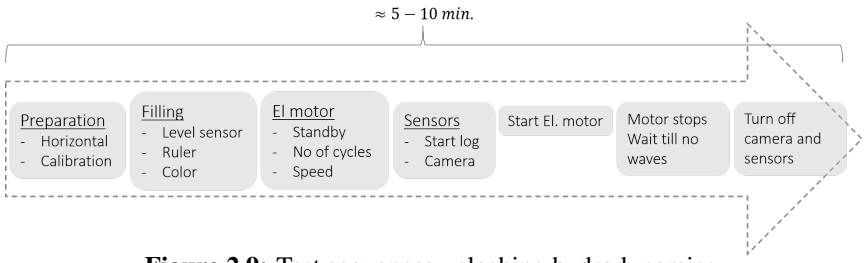

Figure 2.9: Test sequences - sloshing hydrodynamics.

2.2.4 Thermodynamic tank tests

Performing experiments with LNG or methane is not an option due to potential hazards. LNG is a cryogenic liquid with temperatures below -150 [$^{\circ}C$], and its properties are very different from those of water. Experiments were conducted with liquefied nitrogen (LIN), but it was found difficult to control due to extensive heat ingress. Solid materials are also vulnerable to the extreme temperatures. The test medium was therefore changed to water. The experimental work to study the thermodynamic response was performed with a cylindrical pressure tank made of steel. The inner tank was insulated with a 15 [cm] layer of polyurethane foam. The setup is shown in Fig. 2.10. The geometry of the inner tank is the same as that of the transparent tank. Instrumentation consists of a pressure sensor and several thermocouples placed vertically in the middle of the tank. Not all of the probes are active at the same time. This depends on the filling. The given setup was prepared for $h/D = 0.25$, $h/D = 0.50$, and $h/D = 0.70$. The first option was performed with nitrogen, while the 50% filling was tested with water.

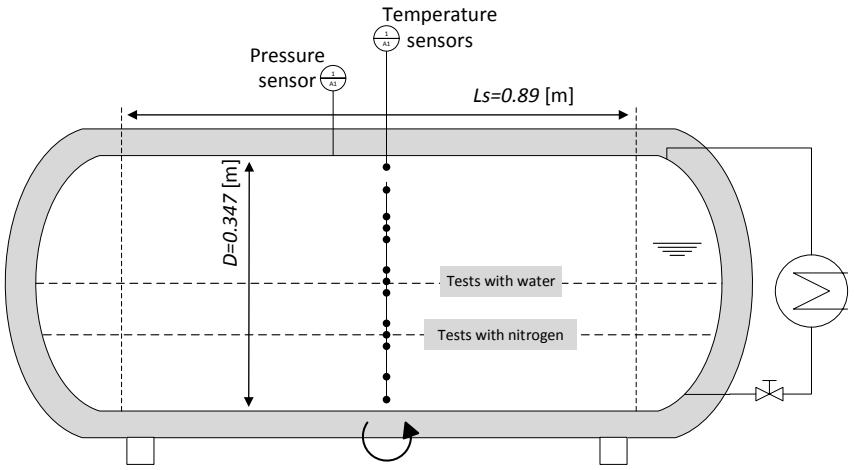

Figure 2.10: Pressure tank and instrumentation. A PBU is installed to the right to vaporize liquid water.

Table 2.1: Specifications of instrumentation and devices.

Device	Type	Range	Accuracy
Temperature sensor	Thermocouple type T	-270-370 [°C]	$\pm$1.0 [°C]
Pressure sensor	P8AP	0-20 [bar]	0.3 %
Heating element	Høiax	0-1460 (max. 3000) [W]	-
Voltage supply	Philips 2422 530 05401	0-260 [V]	-
Electro motor	MAC800-D2	750 [W] @ 3000 RPM	$\pm$0.5 % (speed)

The instruments and their specifications are given in Table. 2.1. At the right side of the tank in Fig. 2.10, a PBU has been installed. It was used to build up pressure when testing with water. A heating element warms the liquid and vaporizes it. The heater is placed lower than the mean depth, and the flow of water and vapour is driven by the hydrostatic pressure difference. The relationship between mass flow and power supply was measured in advance to know the mass flow of vapour for a given voltage supply.

The experimental facility is not really suitable for cryogenic liquids. It was difficult to control the heat ingress due to the extreme temperatures. However, the tests provided us new information about the influence that sloshing has on the thermodynamic response.

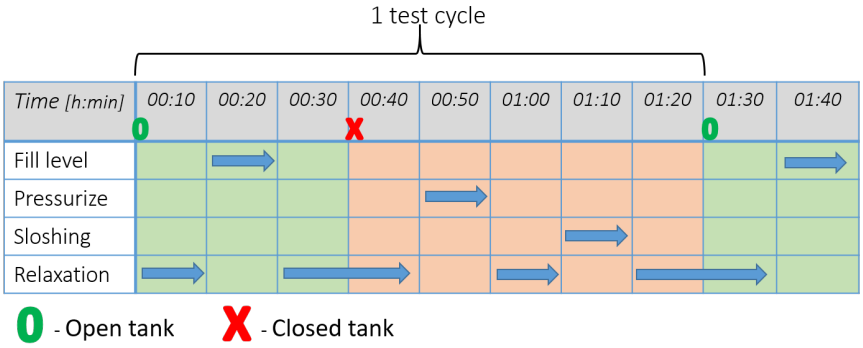

Figure 2.11: Test sequence LIN.

The test sequence with nitrogen is summarized in Fig. 2.11. Initial cooling of the tank is not included. A tremendous amount of nitrogen vapour is generated in the beginning, and the cooling of the system takes 1-2 hours. During this period, the tank must be partly closed to suppress boiling at atmospheric pressure. But eventually the tank must be opened to add more LIN, which results in enhanced evaporation due to reduced pressure. Of particular importance is the relaxation of the system in between the sequences. Registration of the correct level was possible only by reading the sensor values. Once the correct level was found, the tank was closed. Nitrogen gas may then be injected to increase pressure before sloshing. After sloshing, the waves has to cease before the measurements stop. The tank may then be opened, followed by evaporation and decrease of the liquid level. After some time, the tank may be filled to the same level and the sequence repeated.

The test sequence with water starts with an initial heating of the system. This depends on how long a time the system has been left unused. It may stay warm for 1-2 days. Cooling in between the sloshing periods must be done in every test. The initial heating sequence is illustrated in Fig. 2.12. The liquid is heated from approximately 15-20 [$^{\circ}C$] to 120 [$^{\circ}C$]. The PBU power used to generate vapour was limited to 1460 [W] in these tests. The tank is initially left open to remove air. However, some minor air content was still present. Switching between sloshing and heating efficiently increases the temperature and enhances the mixing inside the tank. The resulting temperature-history during a heating process is shown in Fig. 2.13.

Figure 2.12: Test sequence with water - heating of the system.

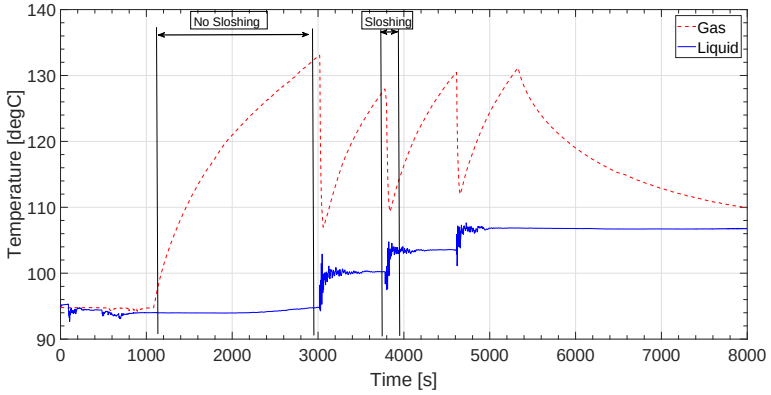

Figure 2.13: Temperature plot during a heating process with water.

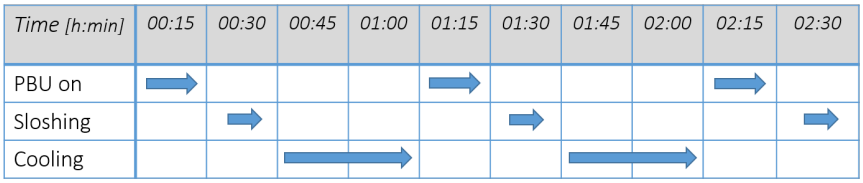

Figure 2.14: Test sequence with water - sloshing tests.

When the system is ready for sloshing tests, the pressure is increased to approximately 3 [bara]. The heater is turned off and the electro motor starts with a specified frequency and number of periods. The sequence is illustrated in Fig. 2.14. Cooling in between the tests is time consuming, but necessary to ensure the correct initial conditions.

2.3 Computational Fluid Dynamics (CFD)

A more detailed analysis can be performed with CFD. Existing simulation models were used to analyse sloshing hydrodynamics, and a new model was implemented to investigate thermal mixing.

Simulation models may be based on correlations between sloshing hydrodynamics and heat transfer. This approach was considered in the theory outlined in section 2.1.1. Simulating the detailed mechanisms of phase change is not a part of the scope, but rather by combining CFD and simple assumptions to predict the thermodynamic response. In line with the main objective, the pressure drop should be estimated for any tank geometry and inner structure.

Different CFD methods have been applied in this thesis, and it is found to predict sloshing characteristics well for a range of conditions. Hence, CFD may replace the experimental tests, and tank inner structures may easily be included with CFD. A method has been developed that extends the existing solver to simulate thermal mixing. The pressure drop rate is closely connected to the mixing time and transport of thermal energy.

The equations that describe the physical behaviour of fluids are solved numerically with CFD. It may include heat transfer, chemical reactions, and other applications. The Navier-Stokes equations cannot be solved analytically other than for simplified cases. Modern computers solve algorithms with increasing speed, and have made it possible to simulate complex cases with acceptable accuracy. The typical CFD workflow is illustrated in Fig. 2.15.

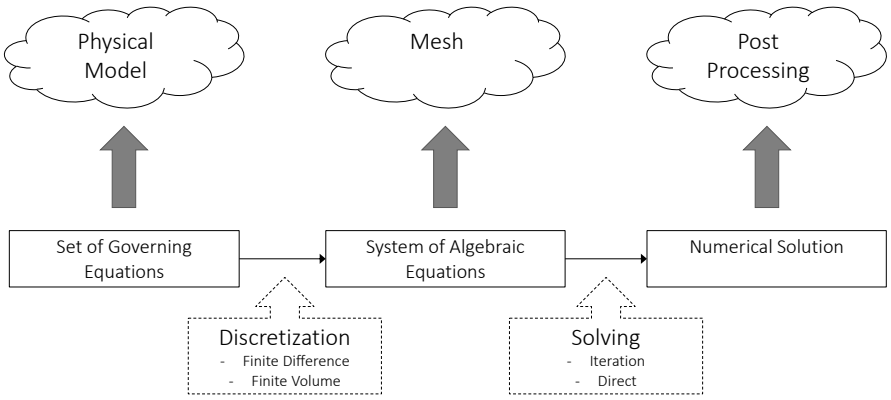

Figure 2.15: CFD workflow.

The set of governing equations depends on the physical aspects of the problem being analysed. They can be equations for incompressible or compressible flow, heat transfer, turbulence or laminar flow, and so on. The governing equations are discretised on a numerical grid which gives systems of algebraic equations. These are solved by iterations to determine variables like velocity and pressure.

Simulations with both finite difference and finite volume methods were conducted with the software packages REEF3D ([5], [6]) and OpenFOAM ([14], [34], [32]) respectively. REEF3D was used to simulate sloshing in rectangular tanks. This is a finite difference code, and solves the Reynolds-averaged Navier-Stokes equations on a structured grid. The tool is relatively easy to use, and ideally suited for simple geometries, like a rectangular tank. It is capable of both 2D and 3D simulations. The starting point with the finite difference method is the conservation equations on differential form. The partial differentials are approximated by finite differences between nodal values on a structured grid ([12]). Taylor series expansion or polynomial fitting is used to obtain approximations of the first and second derivatives.

The idea is borrowed directly from the definition of the derivative,

$$\left(\frac{\partial \phi}{\partial x}\right)_{x_i} = \lim_{\Delta x \to 0} \frac{\phi\left(x_i + \Delta x\right) - \phi(x_i)}{\Delta x}. \tag{2.14}$$

The limiting condition of $\Delta x \rightarrow 0$ is replaced by finite differences equal to the grid spacing. This is illustrated in Fig. 2.16.

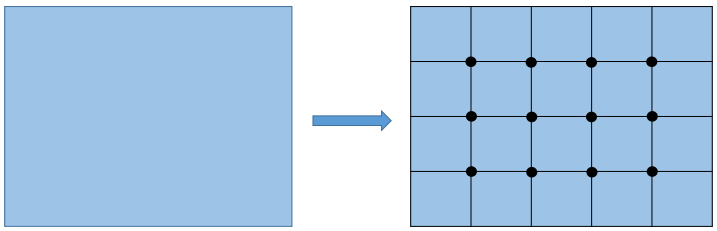

Figure 2.16: Finite differences.

The finite difference method (FDM) has traditionally been combined with a structured grid because it is easy and effective. Unfortunately it is then limited to simple geometries. A ghost cell technique ([4]) has been implemented in REEF3D to account for boundaries and irregular geometry, which gives fewer limitations. A disadvantage with the FDM approach is that conservation is not enforced unless a special care is taken ([12]).

With the finite volume method (FVM), discretisation starts by integration of the local differential equations over a control volume. The mesh consists of several control volumes. Employing Gauss' theorem from the integral equations is an important principle with FVM. The volume integral of fluxes is transformed such that the net value equals the sum of the fluxes over the control volume faces. This is illustrated in Fig. 2.17 and by Eq. 2.15. Since integration is the first step, the method is said to be conservative. The FVM method still relies on approximations, because the values on the control volume faces are interpolated from the neighbour nodal values. FVM is easily applied to all type of grids and thus is suitable for complex geometries. A disadvantage is the difficulty in achieving better accuracy than second order of 3D simulations.

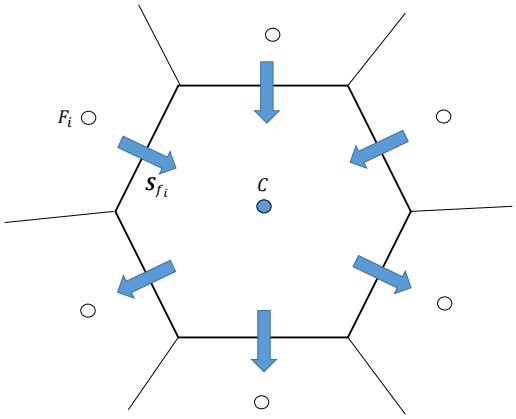

Figure 2.17: The sum of fluxes with the finite volume method.

$$\int_{V_C} \nabla \cdot (\rho \mathbf{v} \phi)\, dV = \int_{S_C} d\mathbf{S} \cdot (\rho \mathbf{v} \phi) \approx \sum_{f_i} \mathbf{S}_{f_i} \cdot (\rho \mathbf{v})_{f_i} \phi_{f_i}. \tag{2.15}$$

$\mathbf{S}$ is the surface area vector of the cell face of cell C. The solution of Eq. 2.15 requires interpolation of the cell face value, ϕ_{f_i}, as well as the velocity vector.

A particular problem in simulating sloshing is the presence of two phases. This requires special treatment of the numerical model. The principle with the VOF and level-set methods is that both phases are solved as if they were *one* phase with *one* set of equations. The different properties in each phase result in different momentum which incorporate the physical behaviour of gas and liquid respectively. The method handles the large deformations of the free surface and reproduces the

sloshing characteristics well. The fluid properties of the liquid-gas mixture are defined using a volume fraction of liquid, α_L, such that

$$\rho_{mix} = \alpha_L \rho_L + (1 - \alpha_L)\rho_G, \tag{2.16}$$

$$\nu_{mix} = \alpha_L \nu_L + (1 - \alpha_L)\nu_G. \tag{2.17}$$

ν is the kinematic viscosity. The volume fraction of liquid in a cell is equal to 1 when the cell is filled with liquid and 0 when it contains only gas. The volume fraction of liquid is advected by solving a transport equation,

$$\frac{\partial \alpha_L}{\partial t} + \nabla \cdot (\mathbf{U}\alpha_L) = 0. \tag{2.18}$$

U is the velocity vector. Using the VOF method generally requires a low time step, because the volume fraction cannot be moved more than a cell length during the time step. Special numerical treatment is necessary to prevent diffusion.

An existing CFD solver in OpenFOAM was modified to include internal energy. The transport equation includes a source term that is proportional to $T_L - T_{sat}$, and activated only where the volume fraction is $0 < \alpha_L < 1$. This term is the condensation mass flow multiplied by the specific enthalpy of formation. The saturation temperature is here taken as the average of the gas temperature. This is reasonable because it has been observed in experiments that the gas temperature is nearly saturated. Sensitivity studies also reveal that the gas superheating has negligible effect on the pressure. The pressure drop rate may thus be calculated from the corresponding saturation temperature. The main assumption is that the pressure drop rate depends directly on the rate of cooling of the gas by the liquid. Initial temperatures found in the experiments are used as starting values by interpolating the sensor values onto the grid.

The first step is to implement a thermal transport equation in the *interDyMFoam* solver. The following version has been used:

$$\frac{\partial (\rho T)}{\partial t} + \nabla \cdot (\rho \mathbf{U} T) = \nabla \cdot [(k_{eff}/c_p)\, \nabla T] + \dot{S}_T. \tag{2.19}$$

ρ is the mixture density. The thermal conductivity k_{eff} in Eq. 2.19 contains the molecular conductivity as well as the contribution from turbulence, k_t.

$\dot{S}_T$ is the heat source activated only at the free surface. k and c_p are mixture properties found with the volume fraction, and given as

$$\alpha_L k_L + (1 - \alpha_L) k_G, \tag{2.20}$$

$$\alpha_L c_{p,L} + (1 - \alpha_L) c_{p,G}. \tag{2.21}$$

The turbulent thermal conductivity is given in a classical manner as

$$k_t = \frac{\rho c_p \nu_t}{Pr_t}. \tag{2.22}$$

ν_t is the turbulent kinematic viscosity. The turbulent Prandtl number, Pr_t, needs to be taken as constant. Here we have used $Pr_t = 2$, which is slightly larger than normal. This is because turbulence is overproduced at the surface with VOF-based two-phase calculations ([19], [18]).

The source term in Eq. 2.19 is activated only at the interface and equal to ([17]):

$$\dot{S}_T = r\, \rho\, 2\alpha_L\, (1 - \alpha_L)\, \frac{T - T_{sat}}{T_{sat}}\, h_{fg}/c_p. \tag{2.23}$$

r is a constant equal to 0.1 $[s^{-1}]$. The term $2\alpha_L\,(1 - \alpha_L)$ is a harmonic mean value of the liquid volume fraction. It is zero everywhere other than the interface. It ensures a smooth transition between the phases. The saturation temperature is updated with each time step. A prerequisite for this assumption is that the thermal energy in the gas relative to the saturated conditions is negligible compared to the liquid. The pressure is estimated from the saturation temperature, $P(T_{sat})$. This is done by the use of Teten's equation [33],

$$P_{sat} = 0.61078 \cdot exp\left(\frac{17.27\, T}{T + 237.3}\right). \tag{2.24}$$

The units of pressure P and temperature T are here $[kPa]$ and $[^\circ C]$ respectively.

Chapter 3

Results and Discussion

Relevant results from the papers are presented in this chapter. There should be no need to look them up while reading. If the readers wish to learn more details, the papers can be found in Appendix A. The research methods used to obtain these results were described in chapter 2.

The chapter starts by presenting experimental results and simulations involving sloshing hydrodynamics (see section 2.2.3). The rectangular tank geometry is studied first, followed by the LNG fuel tank. The second part presents experimental results considering the thermodynamic response with sloshing of liquefied nitrogen and water in a cylindrical pressure tank (see section 2.2.4). It has the same geometry as a full-scale LNG fuel tank. Predictions of the pressure drop using CFD are then presented (see the section about CFD, 2.3). In the last section, sloshing inside a full-scale tank has been studied by simulating the anticipated tank motion.

3.1 Sloshing Hydrodynamics (RO1, RO2)

Experimental work and numerical simulations involving only sloshing hydrodynamics are presented in this section. The rectangular tank geometry is considered in the first part. The purpose of testing this geometry is to investigate the applicability of CFD to simulate sloshing hydrodynamics, as stated in RO1 and RO2 (see also section 2.2.2). It also serves as a test of the experimental facility. The second part deals with experimental work and simulations of the LNG fuel tank. Wave elevation is compared, and characteristic sloshing regimes are presented.

3.1.1 Numerical simulations of sloshing in rectangular tanks

This work was presented in paper 2 ([19]) and paper 4 ([18]). Research objectives 1 and 2 state that the knowledge about sloshing hydrodynamics should be improved and research methods should be developed. CFD is considered to have great potential in studying sloshing characteristics because there are few limitations on the tank shapes, inner structures and motion parameters that are possible to investigate with CFD. Several more variables can also be visualized compared to experiments. Despite the advantages of applying simulation models, the results must be carefully considered and properly validated. The studies of the rectangular tank were found necessary to prepare for the studies of the LNG fuel tank geometry. The geometry is simple; it is easy to model and build and thus provides a good starting point to investigate our experimental test facility and simulation tools.

Comparison of free-surface elevation between simulations with the open-source CFD tool REEF3D and a limited number of external experiments ([24],[7]) was done in paper 2 (P2) [19]. The agreement was good for linear and resonant sloshing cases. Increased deviation was seen when rapid oscillating waves were present, typically beyond the bifurcation point. Limitations with numerical simulations involving free-surface flow were pointed out in P2. Over-production of turbulence energy close to the interface occurs because of rapid change in fluid properties. A nice feature with REEF3D is the limition of turbulence production ([9]), which dampens the eddy viscosity close to the interface.

By constructing our own experimental rig, several more experiments could be conducted. These are presented in paper 4 (P4) ([18]). The motion frequencies and filling levels are listed in Table 3.1. The test run with each filling were performed continuously by adjusting the frequency at small steps after several cycles with each frequency. The frequencies range from below resonant sloshing and passed the bifurcation point.

The free surface elevation is compared between experiments and simulations performed with REEF3D in Fig. 3.1, which corresponds to test 4 in Table 3.1. As can be seen, the agreement is good. The sloshing is resonant in Fig. 3.1(a), while the last figure represents sloshing past the bifurcation point. The bifurcation point at shallow depth sloshing occurs at around $f/f_{1,0} = 1.40$. Several more comparisons can be found in [18].

Table 3.1: Test parameters, minimum and maximum frequencies at each filling level.

Test no.	h/L	$f\ [Hz]$	$f/f_{1,0}$	Tank config.
1	0.030	0.233-0.483	0.861-1.785	1
2	0.040	0.300-0.500	0.960-1.601	1
3	0.050	0.300-0.533	0.860-1.529	1/2
4	0.060	0.300-0.600	0.787-1.573	1
5	0.070	0.333-0.633	0.811-1.541	1/2
6	0.080	0.300-0.633	0.684-1.445	1
7	0.090	0.333-0.617	0.719-1.330	1
8	0.100	0.367-0.627	0.752-1.287	1/2
9	0.125	0.500-0.633	0.926-1.173	2

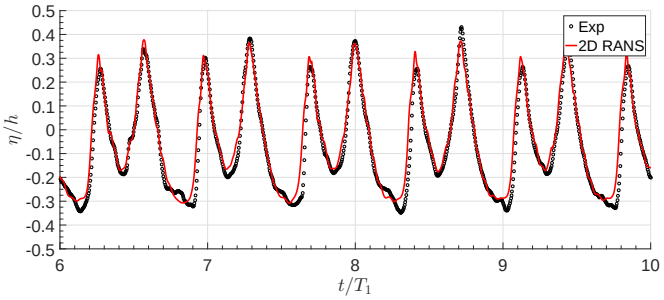

(a) $h/L = 0.06$ and $f/f_{1,0} = 1.40$.

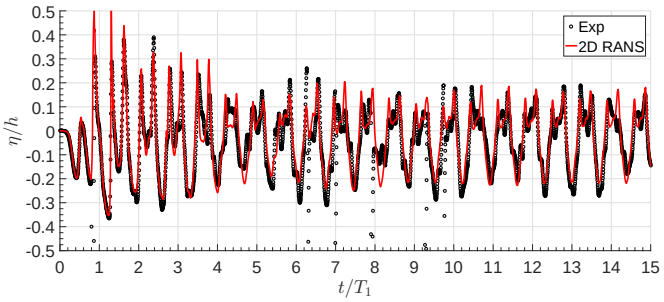

(b) $h/L = 0.06$ and $f/f_{1,0} = 1.44$.

Figure 3.1: Non-dimensional free-surface elevation at forced sloshing, η/h, where h is the mean filling depth. Comparison between experiments and simulations at four different frequencies.

As seen in Fig. 3.1(b), the deviation increases when several oscillating waves are present. It occurs when the wave motion is less constrained by the tank motion. At resonance, a single wave is forced to travel in-tact with the excitation frequency, such that the wave speed is $2L/T$. But when the frequency increases beyond the bifurcation point, the motion becomes less constrained, and the damping of motion

depends more on turbulence and dissipation.

To investigate this further, experiments and simulations of free sloshing were performed. This was done by running the platform for half a period and then turning off the motion, as shown in Fig. 3.2. The frequency in the first half of the cycle is $f = 0.167$ [Hz]. What happens is that waves start to oscillate with the natural frequency. The wave amplitude decreases, and the wave number increases. The damping is minimized. The result is shown in Fig. 3.3. The deviation is greater in this case than with forced sloshing. The deviation found in this condition seems to be related to the damping of the eddy viscosity as mentioned.

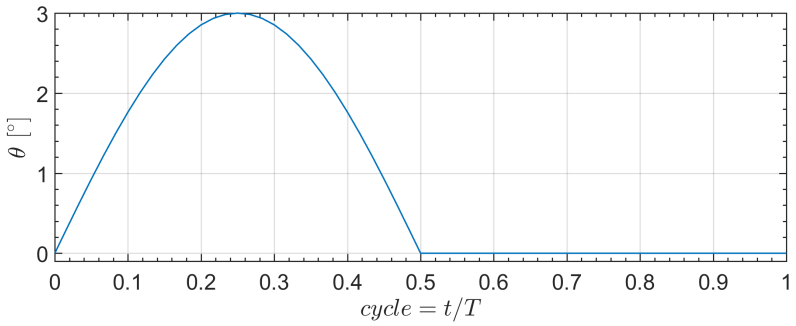

Figure 3.2: Motion turned off after half a period, $T = 6$ [s].

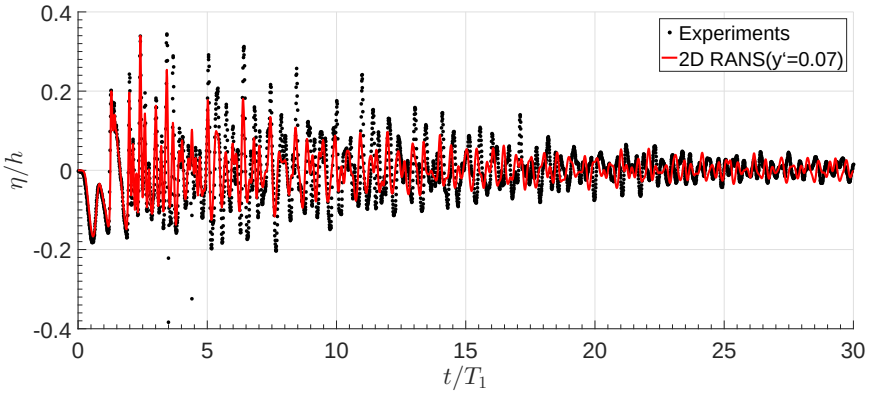

Figure 3.3: Comparison of free-surface elevation at free sloshing. Motion is turned off after half a period with $f/f_{1,0} = 0.437$. The filling is $h/L = 0.06$.

The paradox is that the damping is more sensitive to the turbulence settings when the damping is small. When a single wave is forced to travel at resonance, the moving wall boundary acts as a constraint to the motion. At free sloshing, there are just minor constraints, which is dissipation of kinetic energy in the free stream and due to wall friction. A comparison of 2D and 3D in P4 ([18]) also shows

that the influence of the wall friction is of minor importance, which indicates that the major dissipation is in the free stream. It must be mentioned that although the free-surface elevation is accurately determined for resonant sloshing, this condition would still require a tremendously fine mesh to capture the break-up of the liquid surface. This is not reflected in the measured free-surface elevation.

The accuracy thus depends on the level of detail required in the analysis. These studies have provided knowledge about the limitations using CFD to analyse sloshing. Although deviations were found, they are relatively small. The accuracy is good enough to study sloshing characteristics for any condition.

3.1.2 Sloshing characteristics in LNG fuel tanks

These results were presented in paper 5 ([16]). Research objective 2 states that sloshing characteristics in LNG fuel tanks should be investigated. Comparison between experiments and CFD was performed in order to fulfil RO1.

Several experiments with a model scale LNG fuel tank were conducted, and the different test conditions are summarized in Table 3.2. The minimum and maximum non-dimensional frequencies are given in columns 3 and 4. Several frequencies in between the minimum and maximum given in the table were tested as well. The excitation frequency is divided by $f_{1,0}$ for a rectangular tank because the natural modes are unknown for cylindrical tanks with spherical heads.

Table 3.2: Experimental test data LNG fuel tank.

h/D	h/L	$[f/f_{1,0}]_{min}$	$[f/f_{1,0}]_{max}$	No. of cycles
0.210	0.080	0.640	1.134	20
0.255	**0.097**	**0.833**	**1.066**	**25**
0.340	0.129	0.657	1.023	20
0.500	**0.190**	**0.570**	**1.032**	**20**
0.578	0.220	0.547	1.015	25
0.619	0.235	0.609	1.028	25
0.702	0.266	0.657	1.058	25

Some results from video recordings are shown in Fig. 3.4 (a, c, e, g) representing resonant sloshing at different fillings. At low filling, a single wave rolls up at each end, with pronounced 3D effects.

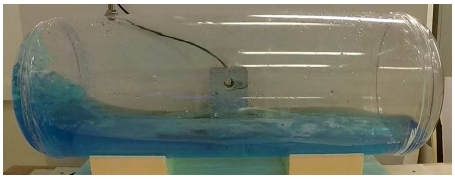

a) $f/f_{1,0} = 0.916$. $h/D = 0.255$.

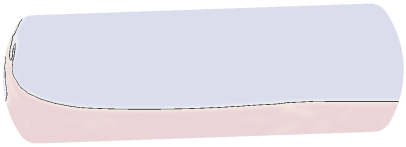

b) Simulation corresponds to a).

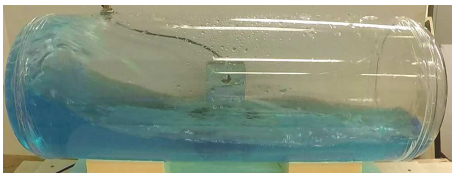

c) $f/f_{1,0} = 0.979$. $h/D = 0.340$.

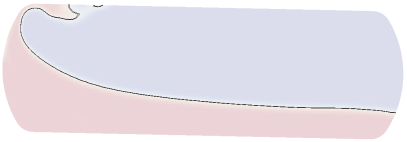

d) Simulation corresponds to c).

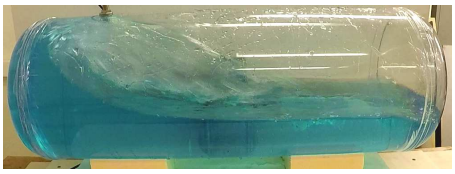

e) $f/f_{1,0} = 0.842$. $h/D = 0.500$.

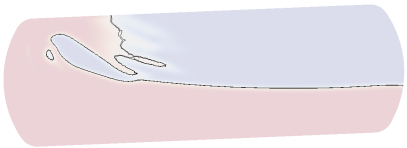

f) Simulation corresponds to e).

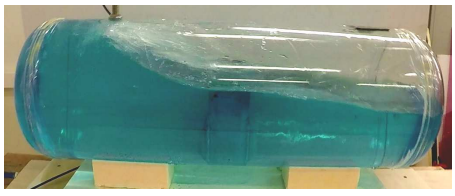

g) $f/f_{1,0} = 0.985$. $h/D = 0.702$.

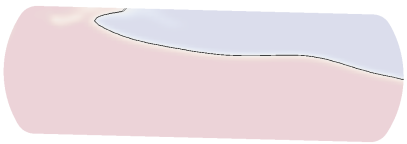

h) Simulation corresponds to g).

Figure 3.4: Snapshots from experiments presented in paper 5 ([16]). Resonant motion inside LNG fuel tanks at different fillings. Comparison between experiments and CFD results.

The spherical form of the heads makes the water concentrate in the middle and increase the vertical momentum. When increasing the filling to $h/D = 0.3 - 0.4$, the water starts to hit the roof. At $h/D = 0.340$ this results in a collapse, and the water falls back down. By increasing the filling to $h/D = 0.500$, a characteristic jet is formed, as seen in the second to last picture. The frequency range for the jet to occur is broadened as the filling gets larger. At $h/D = 0.702$, the jet occur almost on the entire range of frequencies due to the proximity of the roof. CFD simulations with OpenFOAM were performed to investigate sloshing hydrodynamics in LNG fuel tanks. To the right in Fig. 3.4 (b, d, f, h), contours of the liquid volume fraction are presented that corresponds to the time instances on the left. 3D simulations were performed, but presented as 2D contours made by cutting a plane of the tank longitudinally in the middle ($D/2$). The simulations reproduce the characteristics quite well, but resolving the violent jet would require even better grid refinement.

The non-dimensional wave elevation from the simulations is compared with the experimental measurements in Fig. 3.5. Both 2D and 3D simulations are presented. The sensor was only used at the lowest filling. It can be seen that the 3D effects are pronounced. 3D simulation results are in close agreement with the experiments. A consequence of the 3D effects is that simulations cannot be simplified with a 2D model to investigate sloshing as with the rectangular tank. This is easier to see from the contour plots of sloshing with two different fillings in Fig. 3.6. The low filling to the left results in a wave with strong 3D effects. In the first time instance, the water is concentrated in the middle and creates something similar to a fountain. When the column of water collapses and falls down again, it pushes the liquid to the side, which results in a complex wave system. A wave rolls up on each side perpendicular to the main wave in the middle. When the filling is increased to $h/D = 0.5$, the interface is closer to the roof, and the form of the tank head acts as a bend, leading the liquid back with a slope down towards the liquid's surface. Resolving this jet of liquid would require a tremendously fine grid, but may not be necessary as long as the jet is identified from the simulation results.

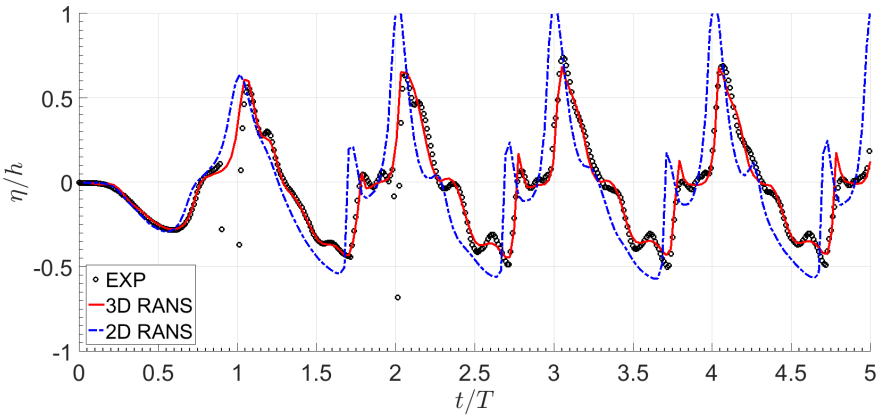

Figure 3.5: Sloshing in a LNG fuel tank. Free-surface elevation compared between experiments, and 2D and 3D simulations. $h/L = 0.255$ and $f/f_{1,0} = 0.92$.

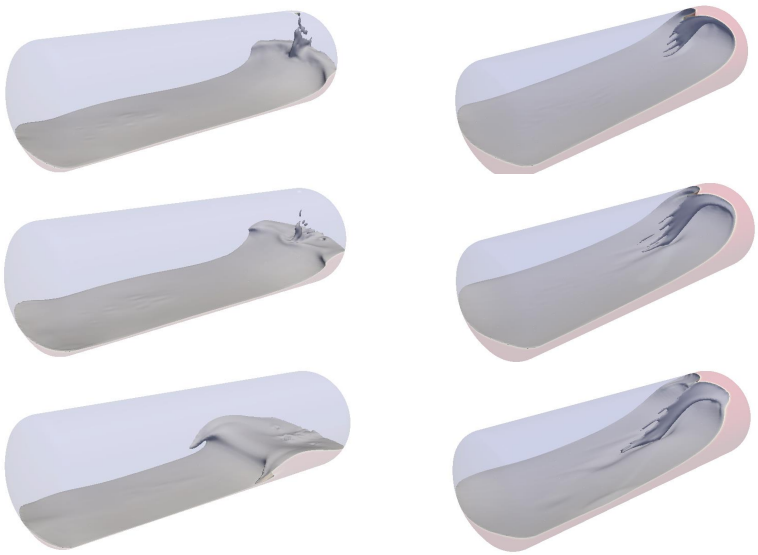

Figure 3.6: CFD simulations of resonant sloshing in LNG fuel tanks. Fillings $h/D = 0.255$ and $h/D = 0.500$ are shown to the left and right, respectively. The 3D effects are pronounced and the sloshing depends significantly on the filling.

By varying the frequency of all fillings in Table 3.2, it is possible to find the lower and upper limits of a *resonance zone*. The upper limit is the *bifurcation* point [11], while the lower limit is defined when a single travelling wave is observed that

violently breaks or turns into a jet. The lower limit depends on the proximity of the liquid to the roof, with a larger range of frequencies with resonant sloshing is found at fillings above $h/D = 0.5$. The resulting resonance zone found from the experiments is presented in Fig. 3.7.

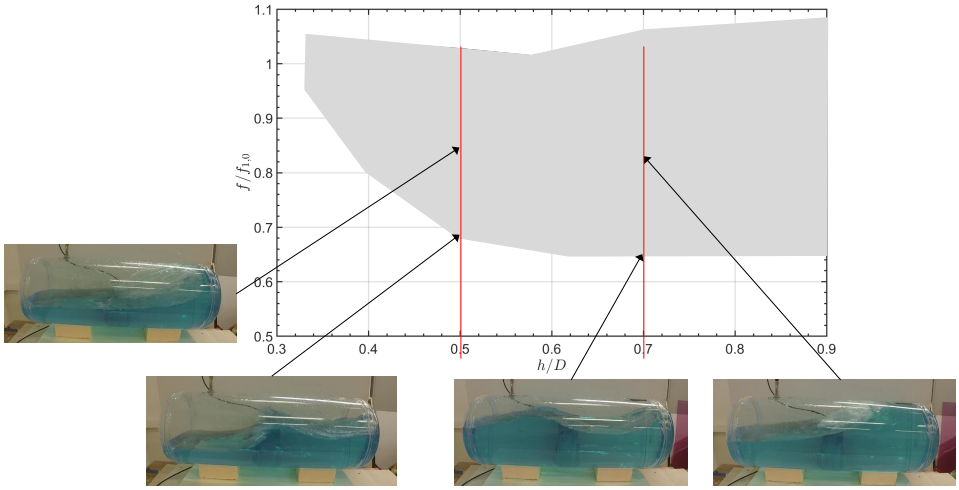

Figure 3.7: Estimated resonance zone for a clean LNG fuel tank with a motion amplitude of 3 degrees and $L/D = 2.68$.

This diagram is not universal and the resonance zone will change with the amplitude and other variables like the L/D ratio. It has been demonstrated in this section that it is possible to use CFD to construct these diagrams for any amplitude, filling, or tank shape and even including inner structure. Fig. 3.7 serves as an example of how to use the experimental results, but it can be done easily with CFD as well. It must be emphasized that $f_{1,0}$ has been calculated for a 2D rectangular tank. The tank with spherical heads has an equivalent length somewhat longer than that of the rectangular tank. This will move the resonance zone upwards in the diagram, which makes the estimated lower limit more conservative here.

3.2 Thermodynamic Response Enhanced by Sloshing (RO3, RO4, RO5)

3.2.1 Sloshing tests with liquid nitrogen

These results are based on paper 3 ([20]). The number of experiments conducted with liquefied nitrogen were limited due to the challenging conditions. Several

more tests were later conducted with water.

These experiments confirm that sloshing enhances the pressure drop. The tank was pressurized with nitrogen gas to create the correct initial conditions at the beginning of sloshing. The pressure and temperature were measured during the entire test. A typical pressure- and temperature plot is shown in Fig. 3.8. The pressure-time history is plotted together with the angle of the motion platform. The motion frequency is $f = 0.17$ [Hz] between 510 and 560 seconds, and suddenly increased to a larger frequency. The gas temperature is not influenced much, but the liquid temperature eventually increases to the saturated temperature.

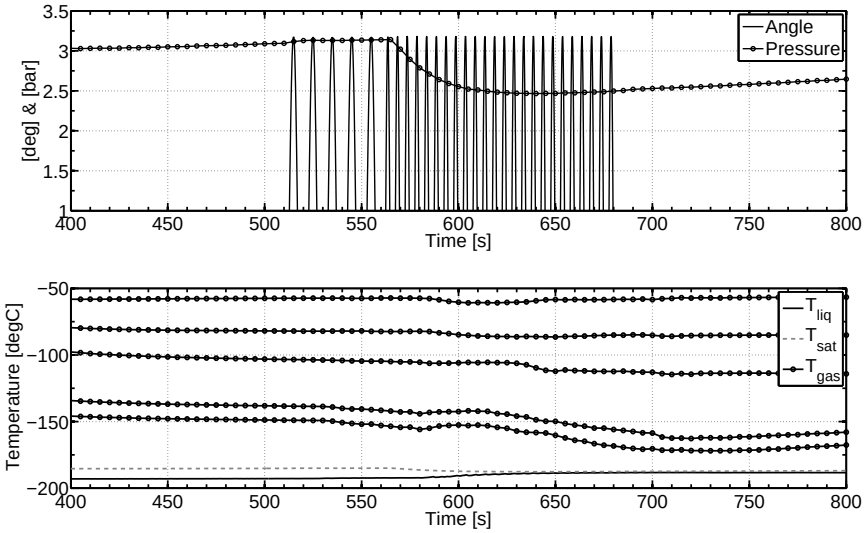

Figure 3.8: Pressure- and temperature-time history in a sloshing tank with LIN.

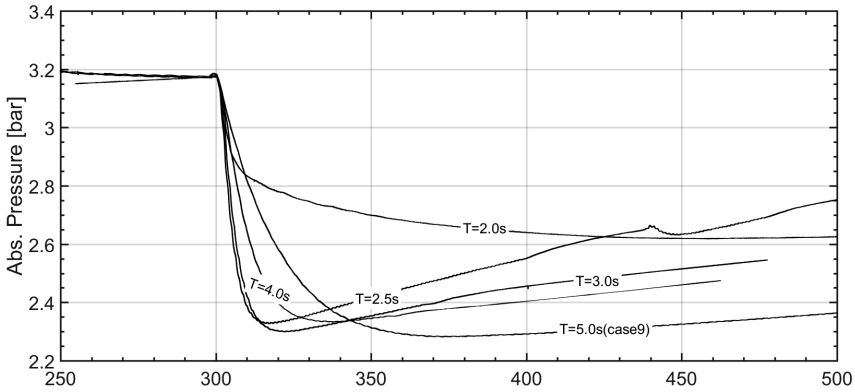

Figure 3.9: Pressure variations due to sloshing with liquid nitrogen and different motion frequencies. Figure from paper 3 ([20]).

The pressure is plotted for different motion frequencies and with a liquid depth equal to $h/D = 25\%$ in Fig. 3.9. Liquid depth, amplitude, and starting pressure are all kept constant in the experiment. Each line contains information about the motion period, T $[s]$. The steepest curve represents the excitation frequency closest to primary resonance ($T = 2.5$ $[s]$). Due to the extreme temperature differences between LIN and the ambient, the pressure starts to increase immediately after reaching a minimum value. The heat ingress works against the condensation process. It was concluded from the analysis presented in paper 2 ([20]) that the sloshing intensity (proximity to $f/f_{1,0}$) has direct influence on the time needed to reach thermal equilibrium (mixing time). The total pressure drop depends on the initial conditions, like the initial liquid temperature and the starting pressure.

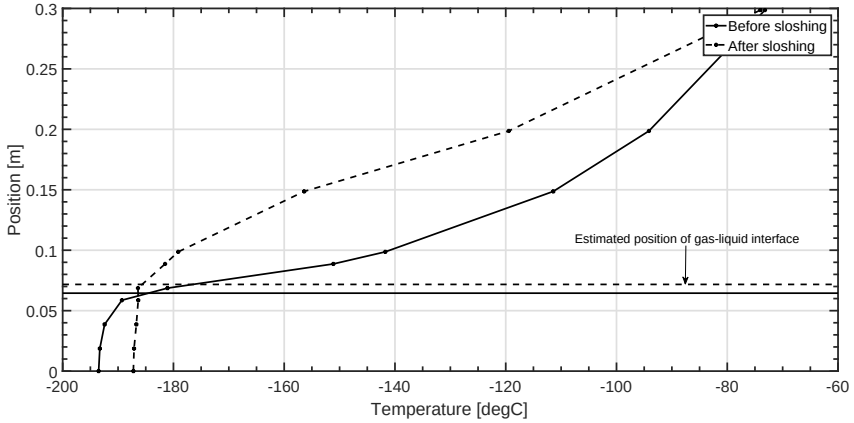

Figure 3.10: Vertical temperature distribution before sloshing and 100 seconds after resonant sloshing. Figure from paper 3 ([20]).

The temperature profile in the resonant case before and after sloshing is shown in Fig. 3.10 ($T = 2.5$ $[s]$ in Fig. 3.9). The temperature gradient is steep on the liquid side before sloshing, but is smeared out after. Only evaporation is possible after sloshing because the liquid temperature is close to saturated, while the gas temperature is superheated. This explains why the pressure increases immediately after the minimum value is reached.

3.2.2 Sloshing tests with water liquid and vapour

Nitrogen was replaced by water in later experiments (P6). The large temperature difference between liquid nitrogen ($T_{sat} \approx -196$ $^{\circ}C$) and the ambient results in heat ingress, while the opposite happens with water. This changes the premise slightly, but is still relevant to the problem. In the first case with N_2, the gas remains superheated, while with water the gas temperature is slightly lower than

T_{sat}.

Pressure measurements with water are presented in Fig. 3.11. Tests were conducted with a liquid depth of 50%. At this filling, there is a liquid jet characteristic for such tanks. Snapshots of the sloshing regime with a transparent tank have been added to the figure. These four cases have been chosen for illustration and comparison. The reason is the very different sloshing regimes and the resulting pressure drop. The minimum pressure and thermal equilibrium are reached only in cases 2 and 3. Case 3 represents the condition closest to resonance (sloshing jet). The pressure decreases by 25% in just 10 seconds. It is obvious from the results that a breaking wave has more influence on the thermodynamic response than a surface with a fixed contact line, as in case 2.

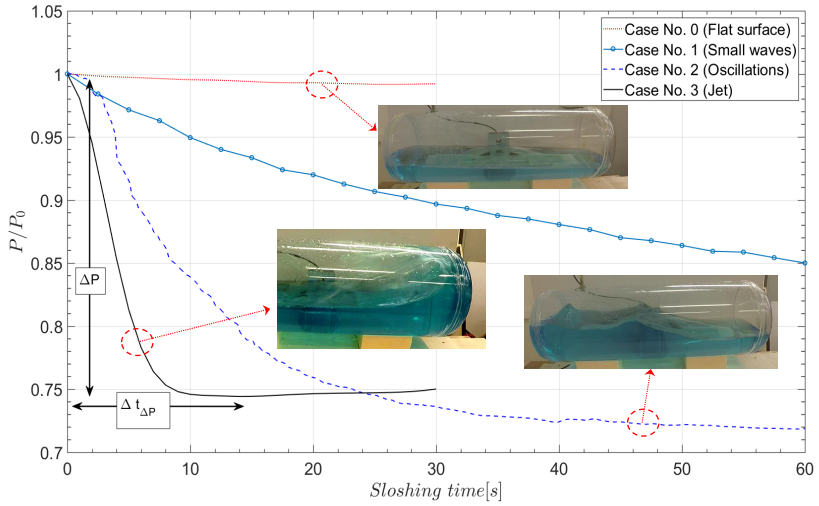

Figure 3.11: Variations of pressure for different sloshing conditions with water. Figure from paper 6.

The corresponding temperature plot is shown in Fig. 3.12. The top and bottom temperatures in the tank are given. Only the first 80 seconds are included. As long as the external heat transfer is small, all cases should eventually reach thermal equilibrium. However, after sufficient time, the final temperature will be equal to the room temperature. As heat is added in between the sloshing, it causes underpressure inside the tank. In case 3 the sloshing intensity is severe, such that a temporary equilibrium is reached after only 10 seconds.

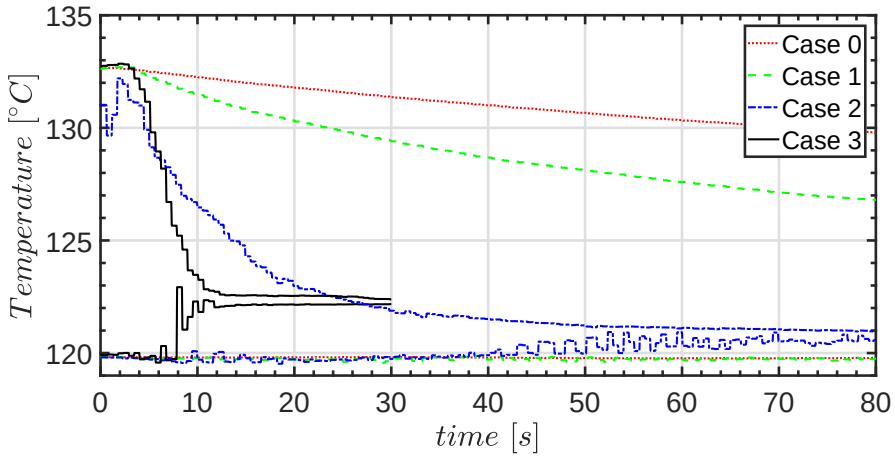

Figure 3.12: Top and bottom temperatures in tank during sloshing. Corresponds to Fig. 3.11.

As with the nitrogen tests, it may be concluded from these results that the sloshing intensity influences the time rate of change of the pressure (dP/dt), or the *mixing time*. This is the most difficult variable to estimate. The final state depends on the initial state and can be estimated as shown in the next section.

3.2.3 Tuning of the lumped capacity model

These results are based on the theory outlined in section 2.1.1 and paper 6.

The condensation mass flow has been modelled as a constant times the difference between the mean liquid temperature and the saturation temperature, $(T_L - T_{sat})$ (see section 2.1.1). This constant was proposed to consist of the product of a heat transfer coefficient and the interface area, $h_L \cdot A_i$. It is difficult to know how each of them weight and vary in time. By implementing the theory into Matlab, it is possible to tune $h_L \cdot A_i$ to make a best fit with the experimental data. The same model was implemented with the use of bond graphs ([22], [29], [37]) in paper 6 (P6) using 20sim ([8]). The results are shown in Fig. 3.13. Pressure is shown in the column to the left. At the right, the mean temperature in the gas (top) and liquid (bottom) is shown. The agreement is quite good. The gas temperature is reduced exponentially and flattens out at the equilibrium temperature. Thermal equilibrium is reached only in cases 2 and 3 (Fig. 3.13(e) - Fig. 3.13(h)).

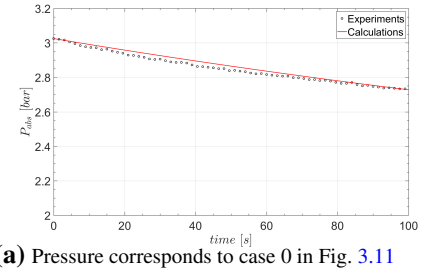

(a) Pressure corresponds to case 0 in Fig. 3.11 (flat surface).

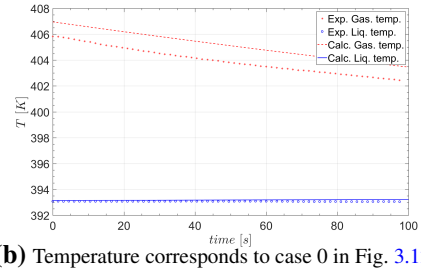

(b) Temperature corresponds to case 0 in Fig. 3.12 (flat surface).

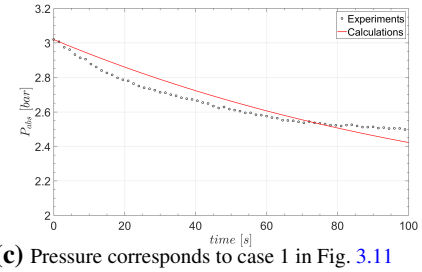

(c) Pressure corresponds to case 1 in Fig. 3.11 (small waves).

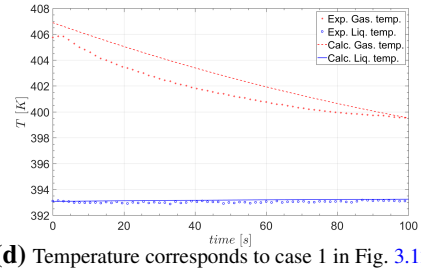

(d) Temperature corresponds to case 1 in Fig. 3.12 (small waves).

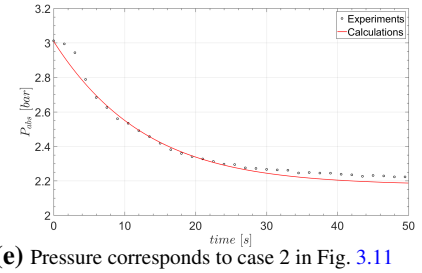

(e) Pressure corresponds to case 2 in Fig. 3.11 (oscillations).

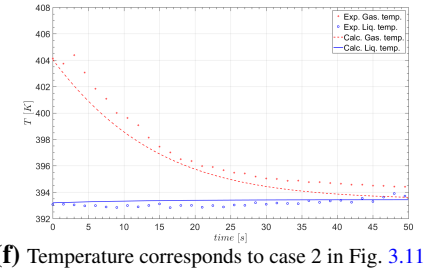

(f) Temperature corresponds to case 2 in Fig. 3.11 (oscillations).

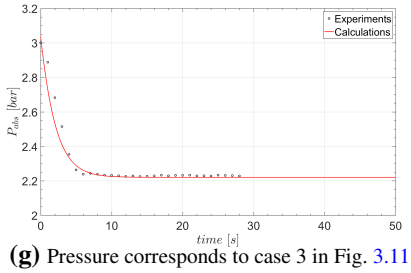

(g) Pressure corresponds to case 3 in Fig. 3.11 (jet).

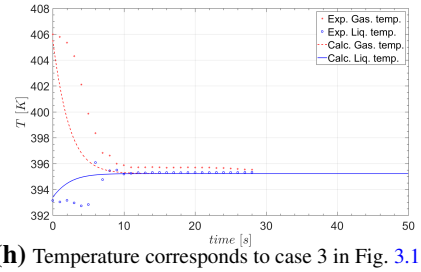

(h) Temperature corresponds to case 3 in Fig. 3.11 (jet).

Figure 3.13: Comparison between experiments and theory. Pressure in the left column and temperature in the right column.

Performing simple simulations like this has several benefits. It provides the same answers as steady-state calculations, but the equations are easily solved numerically without any significant error compared to analytical solutions. The physical mechanisms of the constant $h_L \cdot A_i$ are not known, but it seem to correlate with the sloshing intensity. In cases where the mixing takes a long time, heat ingress may influence the results. This has not been accounted for in the analysis. The model is very efficient, and may easily be combined with other system models.

Some estimates from the analysis are presented in Table 3.3. $m_{0,air}/m_{0,tot}$ is the initial mass fraction of air in the gas, $-\Delta P$ [bar] is the total pressure drop, P_{max} [bar] is the maximum absolute pressure before sloshing, $\Delta t_{\Delta P} \cdot f$ is the number of motion cycles to reach the minimum pressure, $h_L \cdot A_i$ is the heat transfer coefficient times the interface area, and $\Delta m_{cond}/\Delta m_{0,vap}$ is the total condensed mass fraction of the initial vapour mass during $\Delta t_{\Delta P}$. The air content can be accurately determined by comparing the final temperature and pressure. The final temperature must correspond to the saturation pressure. If they do not match, this is due to air still being present. By improving the routines of experiments performance, the air content eventually became insignificant. The constant, $h_L \cdot A_i$ is considered to be the inverse of a thermal resistance, which controls the time needed to reach thermal equilibrium. The second to last column represents the estimated amount of condensed vapour mass divided by the initial mass of vapour.

Table 3.3: Some results found by tuning the simulation to fit the experimental data.

Case No.	$\frac{m_{0,air}}{m_{0,vap}}$	$-\Delta P\ [bar]$	$P_{max}\ [bar]$	$\Delta t_{\Delta P} \cdot f$	$h_L \cdot A_i$	$\frac{\Delta m_{cond}}{m_{0,vap}}$	$f/f_{1,0}$
0	0.470	0.037	4.0254	N/A	9	0.02	0.200
1	0.030	0.453	3.0213	N/A	35	0.15	0.427
2	0.075	0.642	3.0086	40	330	0.23	0.495
3	0.240	0.569	3.1221	7	2500	0.21	0.840

The estimated constant parameter of Eq. 2.13 is plotted for different $f/f_{1,0}$ in Fig. 3.14. The trend is not surprising, since the parameter $h_L \cdot A_i$ is tuned with the experimental pressure. As mentioned before, the pressure drop rate, which determines the time to reach the minimum pressure, correlates with the *sloshing intensity*. The parameter $f/f_{1,0}$ may represent sloshing intensity, or severity. The *total pressure drop*, ΔP, depends on the initial conditions in the tank, like the pressure, and the liquid subcooling. Unfortunately, no experiments were conducted beyond the bifurcation point. This could have made the plot in Fig. 3.14 more complete.

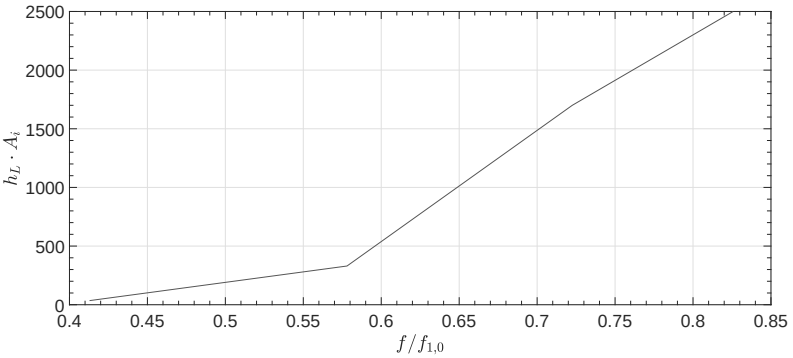

Figure 3.14: $h_L \cdot A_i$ from Table 3.3 plotted for different $f/f_{1,0}$.

3.2.4 The thermodynamic response at resonance

These results are based on paper 7 (P7) [17].

Results presented in paper 7 (P7) show some interesting correspondence between the sloshing hydrodynamics and the pressure measurements. This is an important discovery on the way to understanding the mechanisms that enhance the thermodynamic response. The measured pressure at resonance (case 3) is plotted with a sampling rate of 20 [Hz] in Fig. 3.15. There is a periodic variation of the pressure while it is dropping. The pressure drop rate can be calculated numerically from this pressure. The condensation mass flow is then estimated by the use of Eq. 2.11. The interface area has been predicted by performing a grid independence study with CFD. By normalizing the values, the interface area and mass flow can be compared directly. The result is plotted in Fig. 3.16. The maximum values of the interface area are in phase with the estimated peaks of the condensation mass flow rate (or pressure drop rate; see Eq. 2.11). Synchronized contour plots from the numerical simulations are added to the figure to visualize the sloshing. As the temperature difference is reduced, the peaks also become smaller and eventually cease. This result strengthens the belief that there are local effects that enhance the pressure drop, and that may occur in less than a second. Unfortunately, it is difficult to point out exactly which variable or mechanism is causing this periodic change of state. The maximum area naturally occurs when the sloshing is most severe, like when a wave breaks. But there are a number of mechanisms occurring at the same time, like wall-liquid contact, gas-liquid mixing, transfer of cold bulk, and others. The jet introduces several important effects. Cold bulk is transported efficiently to the surface and brought in contact with the gas.

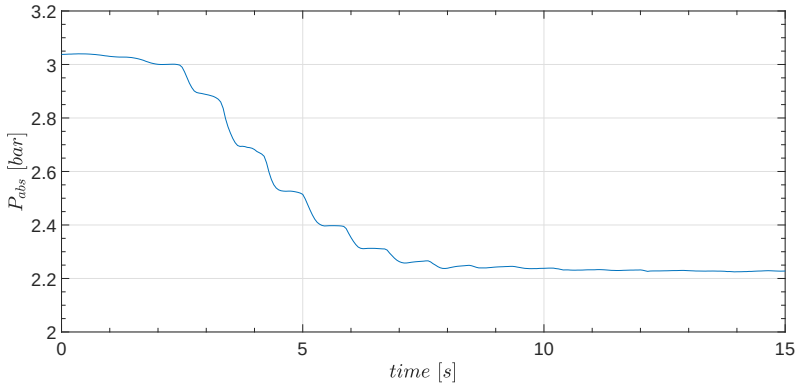

Figure 3.15: Measured absolute pressure in case 3 (jet).

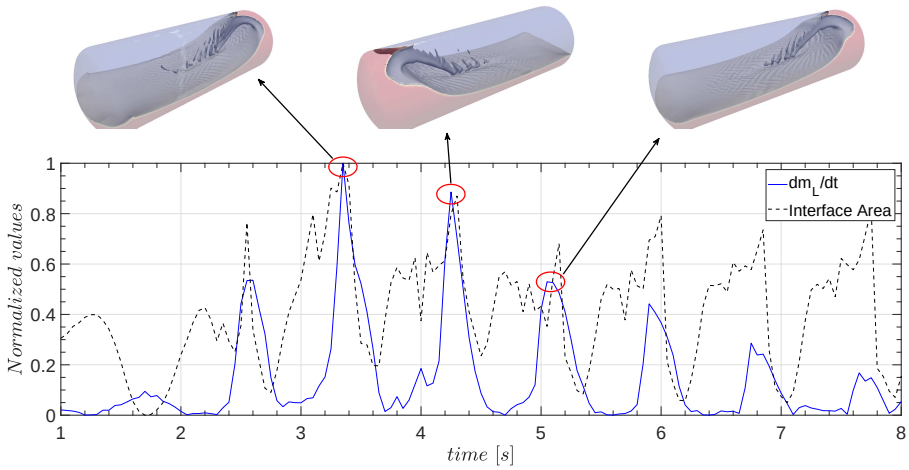

Figure 3.16: Correspondence of the interface area and condensation mass flux estimated from the measured pressure.

3.2.5 Estimate of PBU heat compensation

This work was presented in paper 6 (P6). The purpose of the PBU was initially to maintain pressure in the tank when it was emptied. The pressure drop enhanced by sloshing introduces additional challenges to controlling pressure, and the PBU might have problems compensating for this. The PBU must deliver the same amount of gas that is condensed at all times.

A theoretical prediction of the PBU power, $\dot{Q}_{PBU}$, can be estimated by relating the measured pressure to the mass of condensed vapour, $\dot{m}_L$. Eq. 2.10 can be

rearranged, excluding the temperature contribution to the pressure change, such that

$$\dot{m}_L \cdot h_{fg} \approx \frac{-m_G}{P} \cdot \frac{dP}{dt} \cdot h_{fg}. \tag{3.1}$$

The measured pressure is used to calculate dP/dt numerically as was done in section 3.2.4. The result is shown in Fig. 3.17, including all the cases from Fig. 3.11.

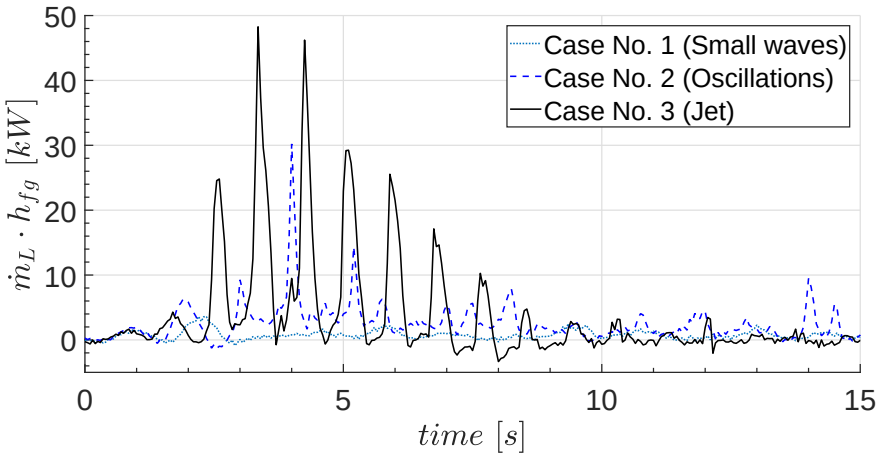

Figure 3.17: Instantaneous condensation heat to compensate for the pressure drop.

Case 3 with the sloshing jet results in a peak reaching almost 50 [kW]. The maximum heat estimate is also significant in case 2. The power in Fig. 3.17 represents time-instant values. Time-averaged values of the aforementioned results may be more realistic. This can be done by filtering the pressure measurement data. The original sampling rate was 20 [Hz]. By employing a reshape function in Matlab the vector is changed such that the sampling rate is reduced to 1 [Hz]. The result is shown in Fig. 3.18. Performing the same exercise as before, the averaged condensation heat is shown in Fig. 3.19.

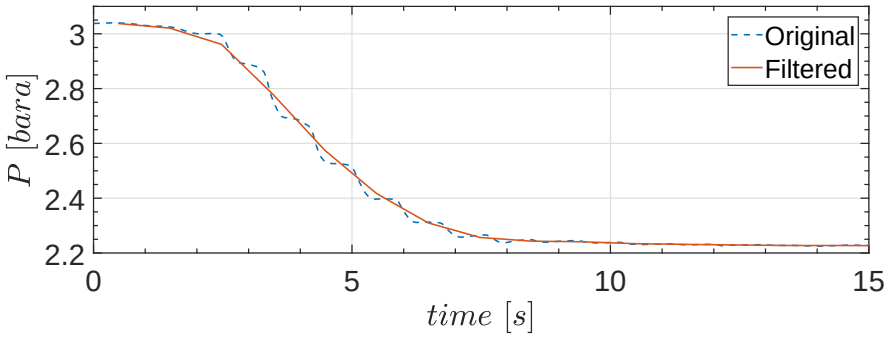

Figure 3.18: Filtered pressure data with 1 [Hz] samples.

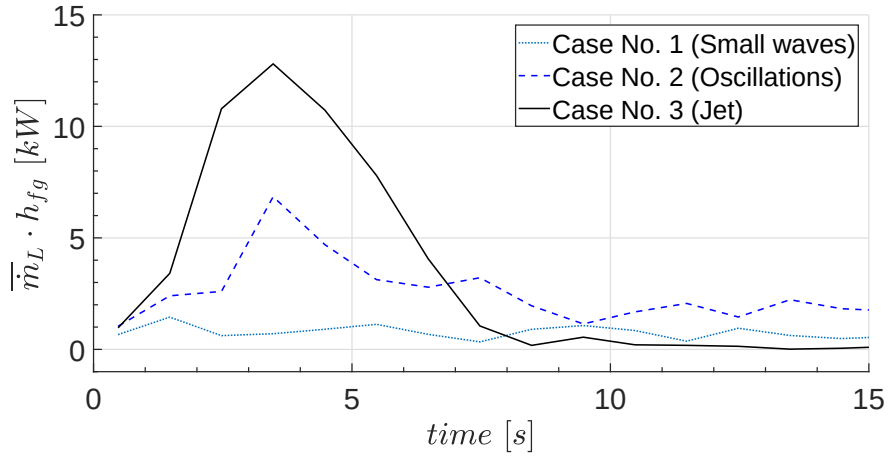

Figure 3.19: Averaged PBU power estimate.

The maximum value of case 3 is now significantly reduced. This is summarized in Table 3.4. It is interesting to note that the value in case 1 is similar to the voltage supply used in our experiments, 1460 [W]. This was the only case where the PBU could compensate for the pressure loss.

Table 3.4: Averaged PBU power estimate to compensate for the pressure drop.

	Case 1	Case 2	Case 3
$\overline{\dot{m}}_L \cdot h_{fg}\ [kW]$	1.45	6.85	12.80

3.3 Prediction of the Pressure Drop with CFD (RO6)

A model to predict the pressure drop rate using CFD was outlined in section 2.3 and paper 7 [17]. The model relies on the correct starting conditions in pressure and temperature, and it is assumed that the pressure drop is related to the internal mixing of liquid and gas. The vertical temperature profile in Fig. 3.20 is used as a starting condition in the analysis. The individual fluid properties of liquid and gas are kept constant and only varied with the liquid volume fraction. The specific enthalpy of formation is kept constant and equal to $2.257 \cdot 10^6$ $[J/kg]$. The other properties are given in Table 3.5.

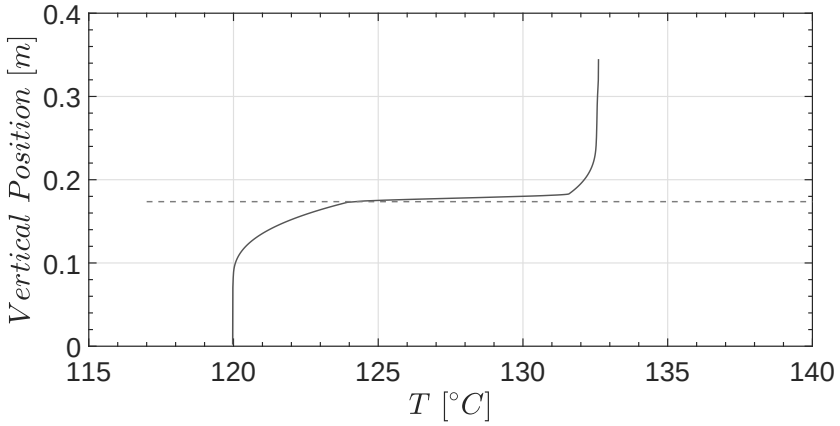

Figure 3.20: Vertical temperature profile inside the tank at the start of sloshing.

Table 3.5: Fluid properties.

Phase	$\rho\ [kg/m^3]$	$\nu\ [m^2/s]$	$c_p\ [J/kg \cdot K]$	$k\ [W/m \cdot K]$
Liquid	997.56	$8.91 \cdot 10^{-7}$	4180	0.62
Gas	1.18	$1.57 \cdot 10^{-5}$	1500	0.03

The pressure from simulations are compared to the experiments in Fig. 3.21. The agreement is is good for the most severe sloshing case, but with large deviations in case 1. The experimental values and numerical results are close to parallel in cases 2 and 3. The start pressure is slightly higher in all cases. The reason is that the pressure has been estimated from the mean gas temperature, taken as saturated. The actual gas temperature is slightly lower in the experiments.

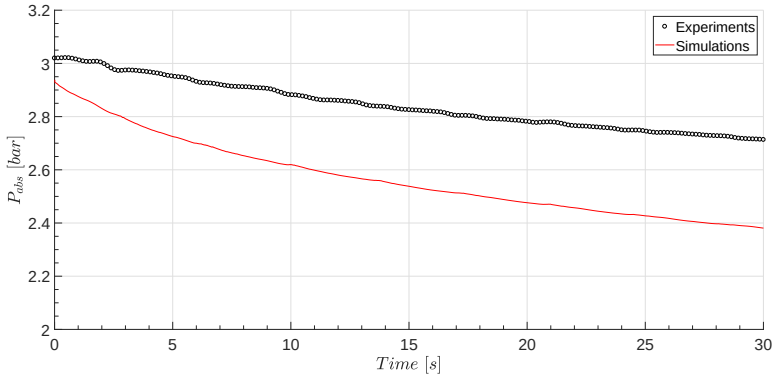

(a) Case 1 (small deformations).

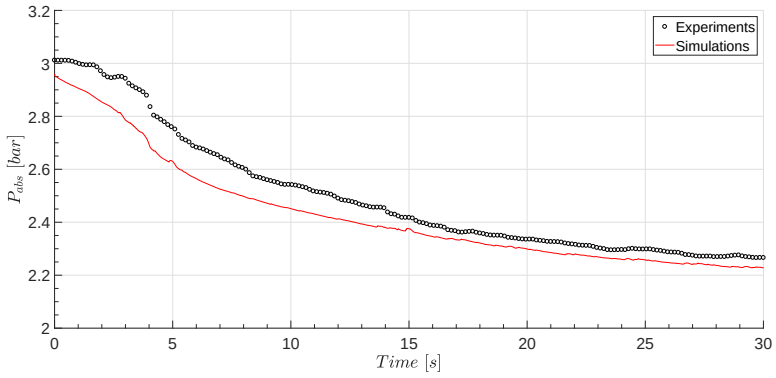

(b) Case 2 (oscillating waves).

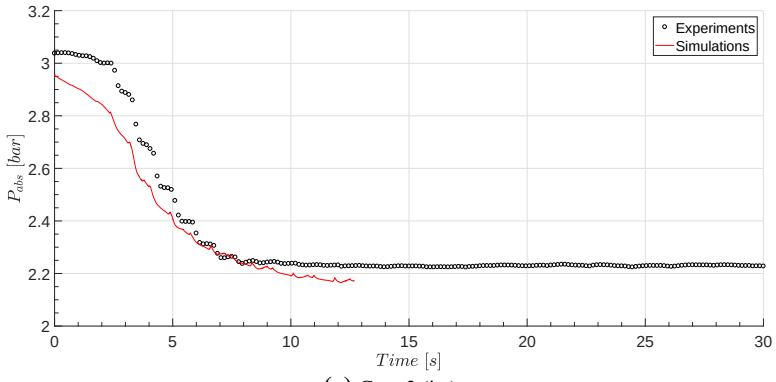

(c) Case 3 (jet).

Figure 3.21: Simulations of the pressure drop due to the enhanced thermal mixing in a sloshing tank.

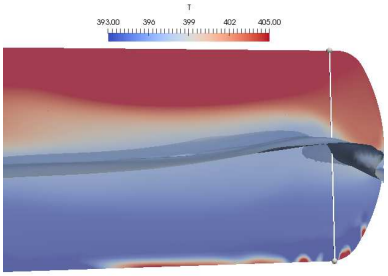

(a) Temperature contour at time 3.1 [s].

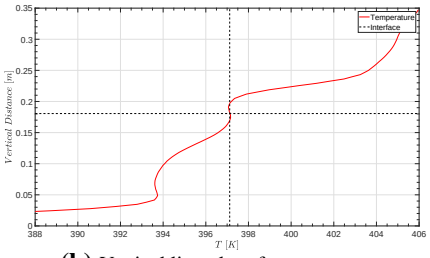

(b) Vertical line plot of temperature.

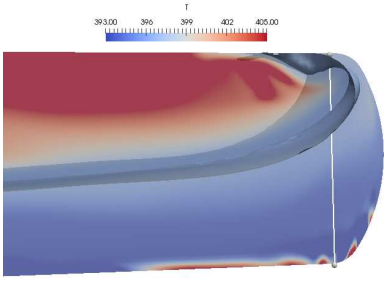

(c) Temperature contour at time 3.2 [s].

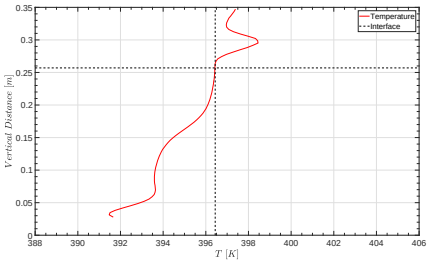

(d) Vertical line plot of temperature.

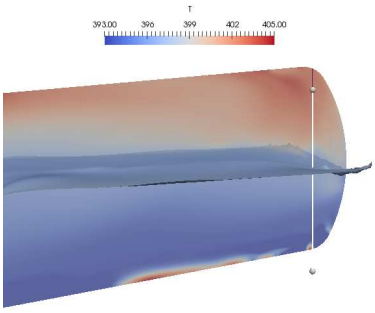

(e) Temperature contour at time 3.8 [s].

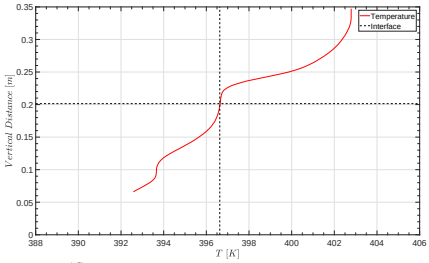

(f) Vertical line plot of temperature.

Figure 3.22: Simulated temperature profile in case 3. The left column shows temperature contours at different time instants. To the right is the temperature profile along the white marked line inside the tank.

Some plots of the temperature development in the tank are presented in Fig. 3.22. In the column to the left, contour plots of temperature for different time instances are given. The white line shows where the vertical profile at the right is plotted inside the tank. The first two figures (3.22(a), 3.22(b)) show the wave at a time instant before the jet is formed along the wall. This is early in the sloshing event, and the temperature gradient is steep on both sides. In the next two pair of figures, the water hits the roof and the temperature profile is much more uniform. It can

be seen that the temperature above the interface is close to the initial interface temperature. The jet thus transports cold liquid efficiently towards the interface. In the last figure, the wave is heading towards the opposite end, and the cooling of the gas is clearly visible comparing Fig. 3.22(b) with Fig. 3.22(f). The gas bulk temperature dropped by 4 [K] during these few seconds. The results may explain why the pressure dropped so efficiently close to resonance. The surface area might not be the dominating factor, but rather the transport of liquid bulk towards the surface. The jet is efficiently mixing together liquid and gas.

3.3.1 Influence of baffles

Additional simulations were performed with case 3 (jet) as a reference case. A ring type of baffle was added inside tank and compared with the data from Fig. 3.21(c). The baffle design and location inside the tank are shown in Fig. 3.23, while the dimensions of the baffles are shown in Fig. 3.24.

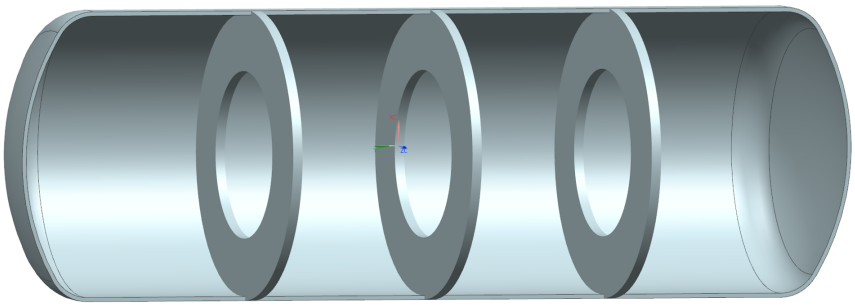

Figure 3.23: Tank with baffles.

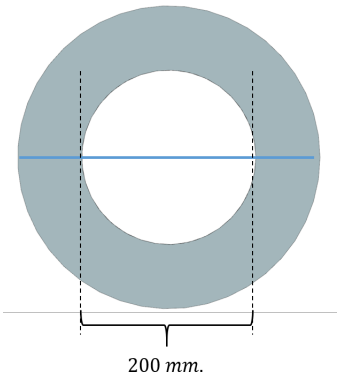

Figure 3.24: Dimensions of the ring baffles.

One baffle is placed in the middle of the tank, while the other two are placed on each side of the middle with a distance of 230 [mm] between them. All three baffles have the same diameter. The same motion frequency and filling depth as in case 3 were used. The resulting pressure is compared in Fig. 3.25 for different ring baffle diameters. Assuming that the thermal CFD model is valid, the presence of baffles reduces the significance of the pressure drop. By studying the sloshing regime, it is found that there are no breaking waves present with the baffles. This is the reason for the large pressure drop seen with the clean tank at approximately 2.5 seconds, when quasi-steady sloshing is established.

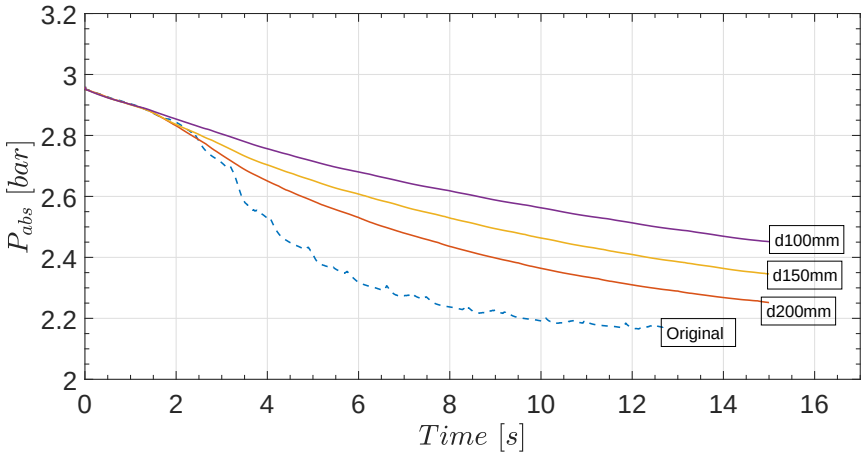

Figure 3.25: Simulations of the pressure drop with ring baffles of different diameters.

The model is based on thermal mixing, and the internal transport may be visualized by contour plots of temperature. This is done in Fig. 3.26 for several time instances with the largest baffle diameter (200 [mm]). The contours of the free surface are also included. The transport of energy can be spotted easily in the beginning with the large temperature differences. The baffles create some vortex shedding, which efficiently transports the liquid. The distance to the free surface seems to be large enough to prevent enhanced transport to the interface. But the baffles are close enough to dampen the breaking wave regime. Removing the breaking wave regime will prevent the large pressure drop. At the same time, it is not known how baffles may affect the mixing of cold bulk close to the interface. Many baffle configurations are possible, and future studies should be conducted to study the effect of baffles in more detail by comparing simulations with experiments.

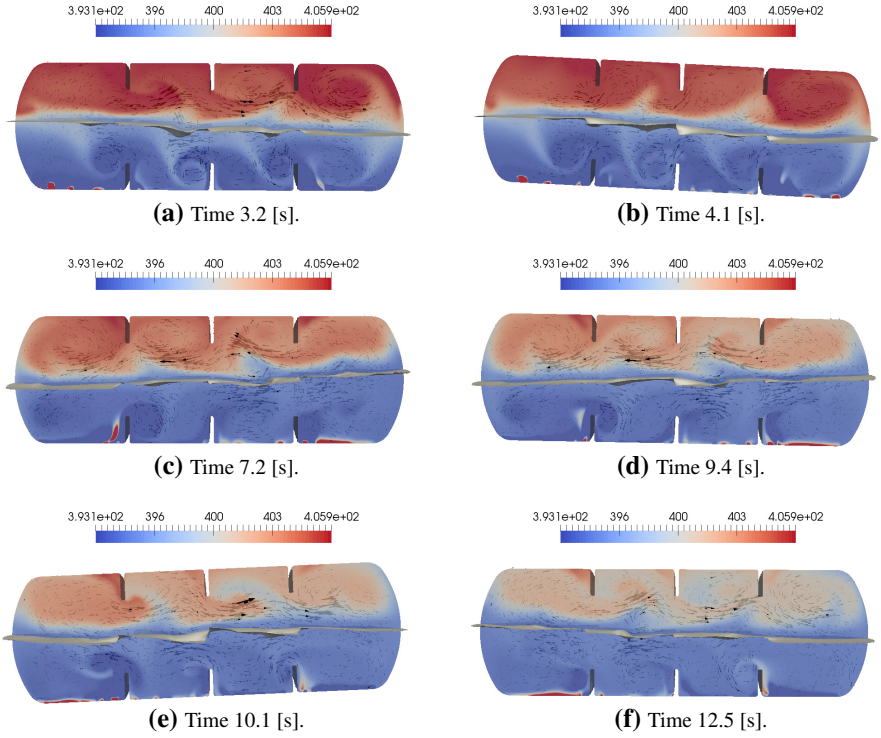

(a) Time 3.2 [s].

(b) Time 4.1 [s].

(c) Time 7.2 [s].

(d) Time 9.4 [s].

(e) Time 10.1 [s].

(f) Time 12.5 [s].

Figure 3.26: Temperature contour plots at different time instances. Ring baffles with a diameter of 200 [mm].

3.4 A Case Study of a Full-Scale Ship

To illustrate how the thesis work may contribute to a real-life problem, a suggested procedure is presented in this section that evaluates sloshing in a full-scale tank on a ship by combining the developed methods. No relevant full-scale data has been analysed so far, but an alternative approach is suggested in the following.

Performing analysis and possibly remedy the enhanced pressure drop depends on whether a ship is already in operation or in the design phase. In the aforementioned case, it would be difficult and costly to change the position of the tank onboard the ship or modify the fuel system. A possible solution could be to avoid the severe sloshing conditions by taking the motion of the ship into consideration when the tank filling is above a certain limit. Modification of the inner tank structure should also be considered. The benefit of considering a ship already in operation is that experience and data can be collected. In the case of a ship not yet built, no data or experience exists, and the motion must be anticipated. However, a more extensive

modification of the design and location of the tank is possible with a ship still in the design phase.

The following approaches are proposed:

1. **A ship *in operation* suffers from rapid pressure loss under severe motion:**

   ➔ Create an overview of the sloshing characteristics for different motion periods and prevent the ship from entering the region that results in resonant sloshing. The CFD analysis provides the necessary information to determine if the sloshing is resonant. It can be used to create a diagram similar to Fig. 3.7 which is unique for this fuel tank. The ship operator may combine the information for filling and expected motion and plan the operations to route of the ship according to these restrictions.

   ➔ Modify the inner structure of the tank to shift the natural frequencies and stay out of the resonant sloshing region. This requires the same analysis as in the previous point.

2. **A LNG-fuelled ship is being designed and prevention of rapid loss of pressure is desired** (this would require a close dialogue with the designers):

   ➔ Estimate typical motions of the ship by combining the anticipated route, weather data, and ship response amplitude operator (RAO).

   ➔ Investigate the sloshing characteristics as in the previous analysis, but now with the possibility of changing the tank location and geometry. The resulting location and design of the tank are a compromise between the optimal sloshing conditions and other design constraints.

   ➔ Use CFD analysis to design an inner structure that ensures a lower resonant limit such that the anticipated frequency of the tank motion is below it.

3.4.1 Investigation of the sloshing characteristics

It has been demonstrated that the hydrodynamic analysis may be conducted with both experiments and simulations, in which the last method has fewer restrictions. Thermodynamic response and sloshing hydrodynamics were investigated separately, but combined with CFD in the last part of the results. A qualitative approach to predict the thermodynamic response is to find the resonance zone for different

conditions and geometries. It was found that the thermodynamic response was related to the parameter $f/f_{1,0}$, with the worst condition being close to the primary resonance ($f/f_{1,0} = 1$). By constructing a plot that contains the lower and upper limits of the resonance zone (see Fig. 3.7), it is possible to identify the sloshing regime of a tank with a certain length, diameter, and filling. A complete map will of course require more simulations or experiments, and baffles will change the diagram by shifting the natural frequencies. A study of baffles and their influence on the natural frequencies in rectangular tanks was performed by Wu *et al.* [38] using numerical methods. The results were compared to a theoretical formula by Faltinsen and Timokha [11]. The numerical results also acceptably predicted the natural frequencies for the surface piercing baffle designs, while the theory became inaccurate.

The CFD tools used in this thesis have proven useful to predict sloshing characteristics. As mentioned, a diagram like the one shown in Fig. 3.7 can be constructed by using CFD for any tank shape and motion. Only a single geometry and amplitude were tested in this thesis, so it is not known whether the data can be transferred to other conditions and tank geometries. But, it can still be used as an example of how to apply it in the analysis. The tank motion must be in the longitudinal direction, such that it may be applied to a tank placed longitudinally on a ship under head sea waves, and transversely if the ship experiences beam seas.

Consider three different tanks with the same volume, all equal to $150\ [m^3]$. The geometries are presented in Fig. 3.27 and scaled correctly according to each other. Using the lower limit from the diagram in Fig. 3.7, and assuming that the diagram is valid for different L/D ratios, the minimum motion periods of each specific tank can be obtained. The result is shown in Fig. 3.28. The period of the tank motion should then be higher than the values in the figure. From this analysis it is obvious that the shorter tank is preferable. It is difficult to give an exact answer to this, and space restrictions and stability measures will in most cases determine the placement and design of the tank.

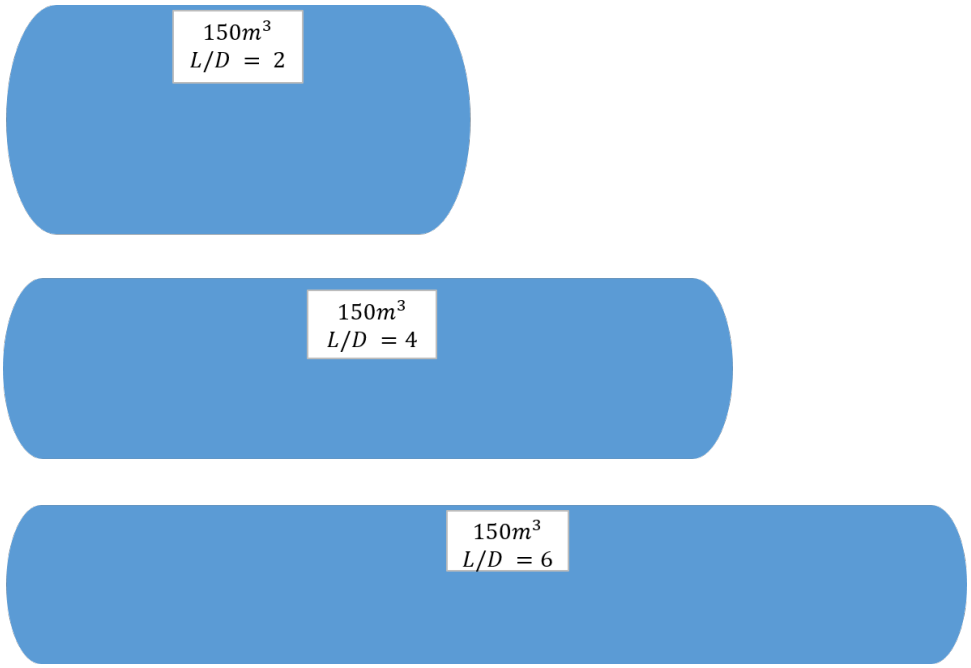

Figure 3.27: Full-scale tanks with typical L/D ratios.

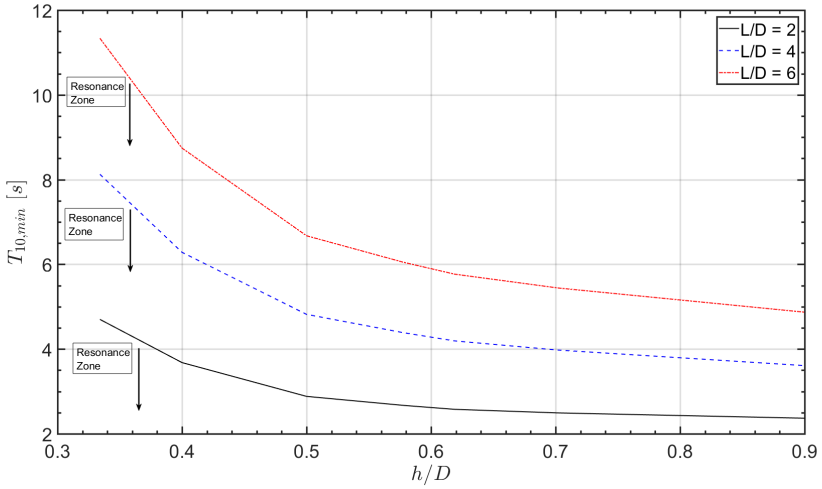

Figure 3.28: The lower limit of the resonance zone for the three tank geometries in Fig. 3.27.

3.4.2 Analysis of a specific ship

Several gas-fuelled ships are in operation along the Norwegian coast. There is no detailed overview of the number of ships that suffer from loss of pressure due to motion and cold LNG. We have been provided some information about a Norwegian gas-fuelled ship. It has a tank similar to the one in Fig. 3.27 with $L/D = 6$ installed longitudinally, as illustrated in Fig. 3.29.

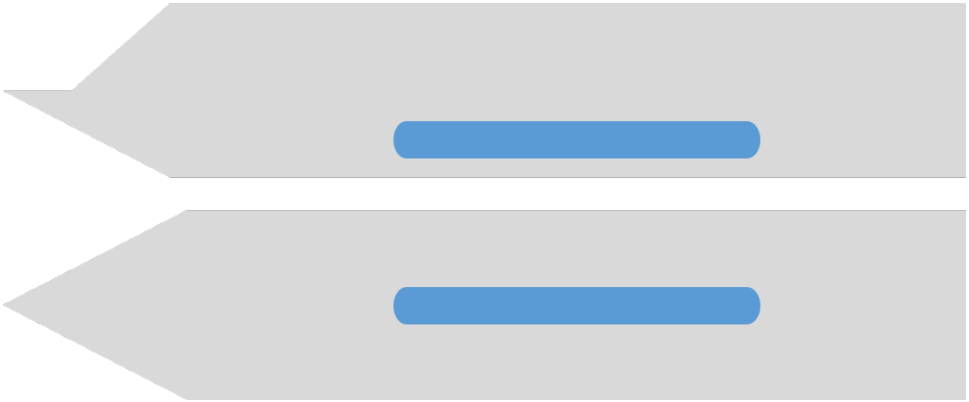

Figure 3.29: Location of the tank onboard the ship.

The information was provided by crew members and is clear in some parts, but more vague in others. It is rather difficult to employ such descriptions in scientific work, but the trends coincide with the results found in the experiments. There are certainly problems in head sea waves, while in beam seas the pressure is more stable. Pressure is influenced even by long head sea waves with small amplitude, but the pressure drop is worsened when the sea state becomes severe. It also depends on the LNG bunkering temperature, which varies between -157 and -150 $[^{\circ}C]$. The pressure drop is a major problem for this ship and derating of the engine is common.

Looking at the ship and the tank location it seems obvious that head sea waves result in the most pronounced pressure loss, and relating this to the large L/D ratio becomes inevitable. No motion or pressure data was obtained for this ship, and analysis must rely on predictions of the vessel's response and the weather data. If the ship motion was known, it could be transferred to the frequency domain and compared with Fig. 3.28, provided that the diagram was valid. This is the most efficient method, but less certain at present. An alternative is to simulate sloshing inside the tank with the prescribed motion using CFD.

With the lack of data, motions must be predicted. This is done by analysing the ship's geometry and calculating the hydrodynamic forces. The vessel's RAO can be estimated for a given heading. This was done by using the software package ShipX ([36]). The RAO gives the transfer function η_a/A, where η_a is the amplitude of the ship's motion and A is the wave amplitude. The motions are surge (η_1), sway (η_2), heave (η_3), roll (η_4), pitch (η_5), and yaw (η_6). η_a is defined according to Fig. 3.30. The ship's motion can be transformed into tank motion by knowing the location of the tank relative to the ship's center of gravity (COG). The RAO for the tank in this specific vessel is shown in Fig. 3.31, and is valid for head sea waves (0 °) and 0 knots ship speed. The values η_a/A can be multiplied with the wave amplitude to find the tank displacement.

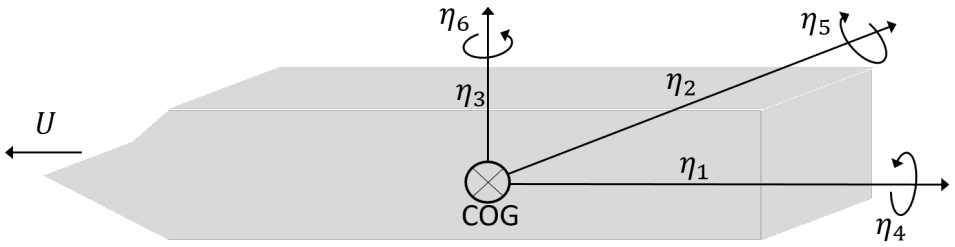

Figure 3.30: Definition of coordinate system and rigid-body motion modes.

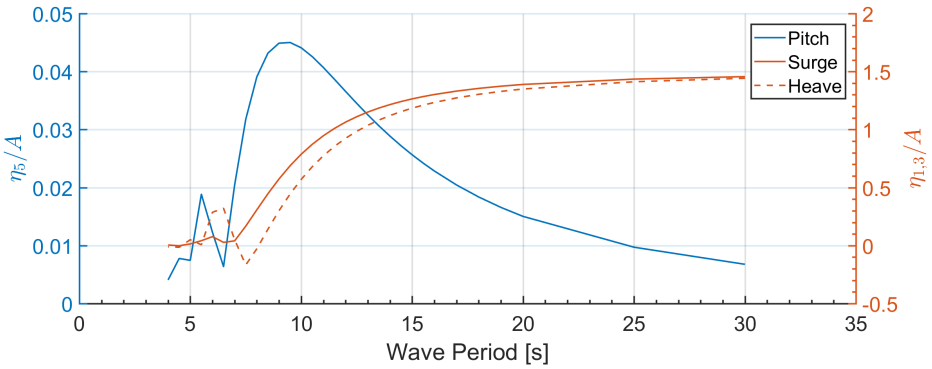

Figure 3.31: Tank RAO for pitch, surge, and heave at 0 knots ship speed and heading 0 °.

The RAO will change depending on the ship's speed. The diagram may be presented as a function of the encounter period by shifting it according to the ship's speed, as a simplification. The encounter frequency is defined as

$$\sigma_e = \sigma_0 \cdot \left(1 + \sigma_0 \cdot \frac{U_s}{g}\right), \tag{3.2}$$

where σ is the circular frequency and $\sigma = 2\pi/T$ with subscripts e and 0 being the encounter frequency and the wave frequency, respectively. U_s is the forward ship speed and g the gravity acceleration. The relation is only valid in head seas with a $0\ ^\circ$ heading angle. At 12 knots, the response will be shifted to a lower period relative to Fig. 3.31. It is noted that the resonance period for pitch is close to a period of 10 [s] (at 0 knots), which is above the lower limit in Fig. 3.28. However, the diagram will in reality change more than just a shift in frequency, so this example is considered simplified.

The wave amplitude and period are still unknown and depend on the wave spectrum, which is a statistical description of waves. The wave spectrum contains a certain wave energy (or amplitude) for different periods and represents the probability of occurrence. The wave spectrum may change the curves in Fig. 3.31 by amplifying the response, if the spectrum coincide with the RAO, or it may deamplify it and broaden the response. The JONSWAP spectrum is representative of the North Sea, and is shown in Fig. 3.32 ([11]).

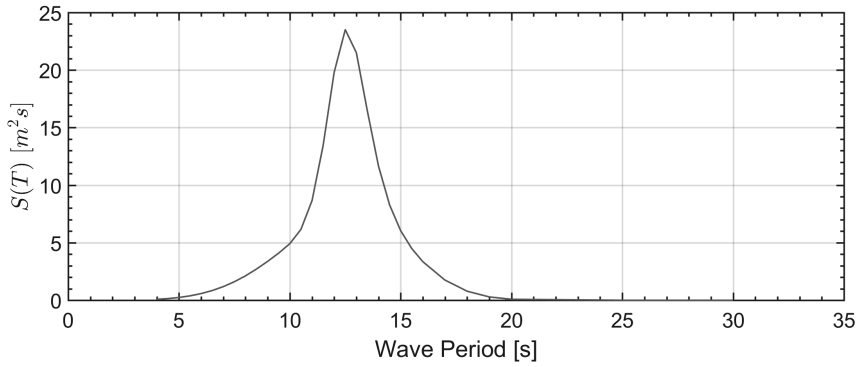

Figure 3.32: JONSWAP wave spectrum [11].

The wave elevation of an irregular sea state can be be written as the sum of a large number of wave components with amplitude A_j. The amplitude is related to the wave energy by

$$\frac{1}{2}A_j^2 = S(\sigma_j)\Delta\sigma, \tag{3.3}$$

where A_j is the wave amplitude of wave component j and $\Delta\sigma_j$ is a constant difference between frequencies in a range.

To keep the example simple, only regular waves are considered. From the information received from the crew, the pressure drop becomes significant in long waves with heights of 1.5-2 metres. By choosing a specific wave height of 2 metres (1 [m] amplitude) and a period of 10 [s], the tank response may be found from the RAO and transferred to the time domain. With a wave period of 10 [s], the encounter frequency at ship speeds 8 and 14 knots is 7.9 [s] and 6.8 [s] respectively. By looking at Fig. 3.28, it can be seen that the longest tank has a lower limit of approximately 6.8 [s] at $h/D = 0.5$. The shortest tank has a lower limit of 2.9 [s] at the same filling.

Considering only pitch motion as relevant, the displacement is given as

$$\eta_5 = A_5 \cdot \left(\frac{\eta_a}{A}\right)_{RAO} \cdot sin\left(\sigma_e t\right), \tag{3.4}$$

with σ_e being the encounter frequency, t as time, A as the wave amplitude (which is chosen to be fixed in this time series), and η_a as the motion amplitude for pitch mode. The resulting motion is given in Fig. 3.33.

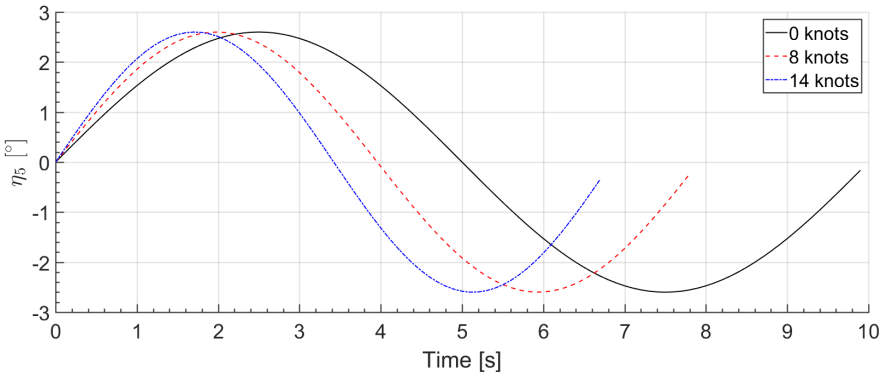

Figure 3.33: Tank pitch at 0, 8, and 14 knots in regular head sea waves. Wave amplitude 1 [m] and a period of 10 [s].

It is seen that the pitch motion has an amplitude of nearly 2.6 degrees at 0 knots. This is slightly less than in the experiments. Simulations for the original full-scale tank with a prescribed pitch motion have been performed. The L/D relationship is approximately 6. It has been compared to a tank with the same volume, but with $L/D = 2.3$. The tank volume is approximately 150 $[m^3]$. To perform these

full-scale simulations, a grid with an average spacing of $\Delta/L = 0.012$ has been used. This gives approximately 340,000 cells, and the mesh is shown in Fig. 3.34. It is coarse considering that more cells were employed to represent the model scale tanks. Still, it is considered fine enough to capture the sloshing wave characteristics. The preliminary implementation of the thermal model would probably require more cells, as there is no special numerical treatment in the model. This should be kept in mind when reviewing the results.

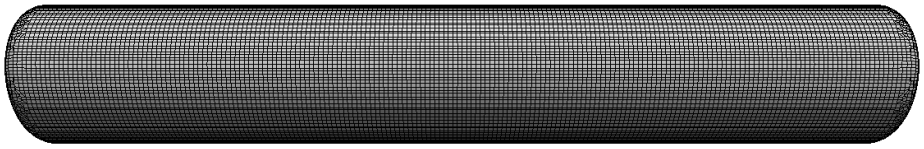

(a) Original tank ($L/D = 6$).

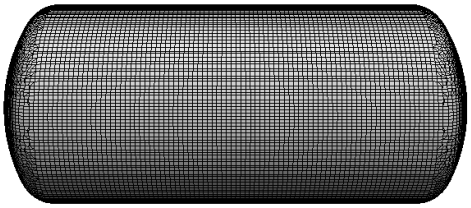

(b) Small tank ($L/D = 2.3$).

Figure 3.34: Mesh used to simulate the full-scale tank.

The tank sloshing has been simulated for the first 30 seconds in both cases. Studying the results, it is considered long enough to know that the sloshing has reached a quasi-steady condition. Screenshots showing the contours of the free surface are used to compare sloshing inside the two tanks. A range of time instances are presented in Fig. 3.35 and Fig. 3.36. Time instances 23.25 to 25.00 [s] show the build up of a wave far to the right inside the long tank. It looks as if a jet is formed, similar to the previous results. However, it is not strong and collapses as seen in Figs. 3.35(c) and 3.35(d). The surface in the short tank is nearly undisturbed. In the next sequence, a wave builds up, as seen at low fillings in the previous results. As before, it rolls up along the tank's side walls. The wave continues towards the lefthand wall and builds up again, as in Fig. 3.35(a). The results are remarkable considering the significant difference between the short and long tanks with equal volume.

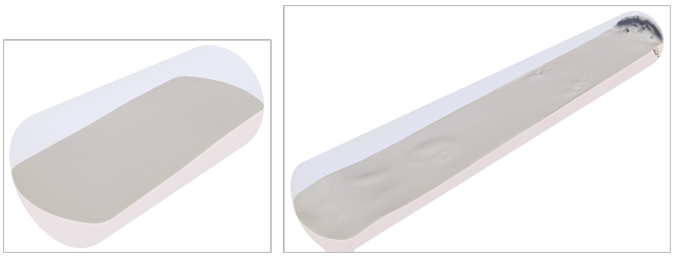

(a) $t = 23.25\ [s]$.

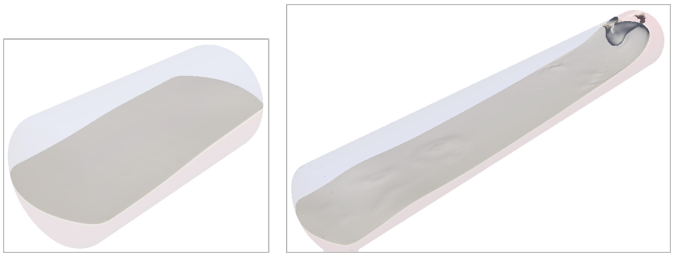

(b) $t = 23.75\ [s]$.

(c) $t = 24.50\ [s]$.

(d) $t = 25.00\ [s]$.

Figure 3.35: Comparison of long and short full-scale LNG tank.

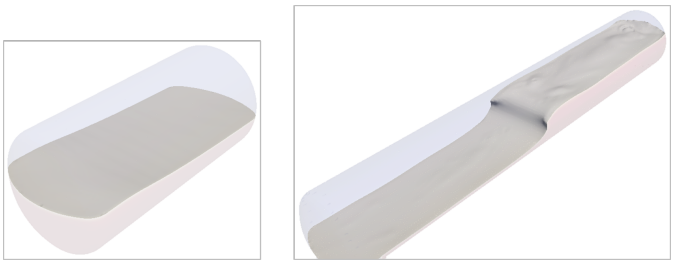

(a) $t = 26.25\ [s]$.

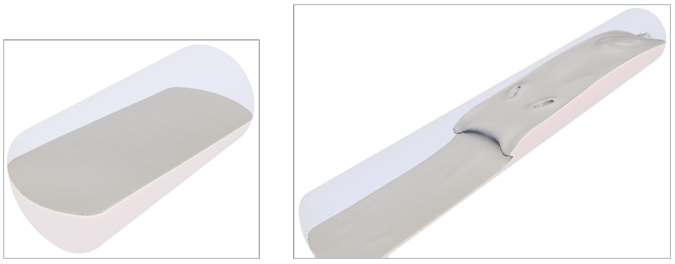

(b) $t = 26.75\ [s]$.

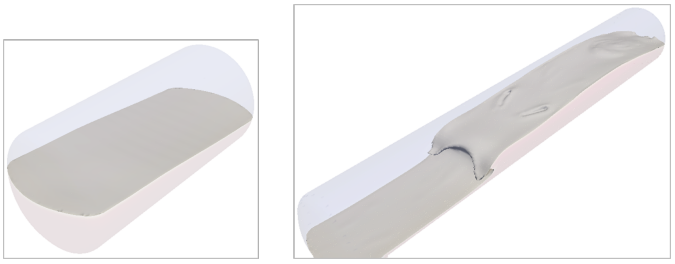

(c) $t = 27.00\ [s]$.

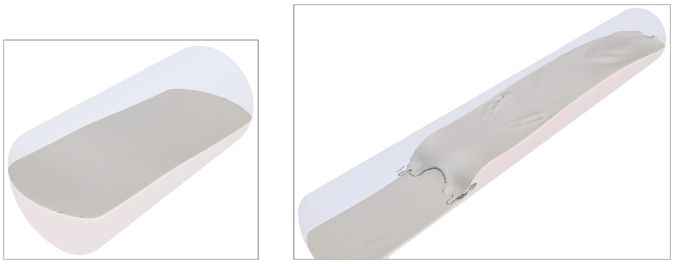

(d) $t = 27.25\ [s]$.

Figure 3.36: Comparison of long and short full-scale LNG tanks.

The first conclusion to the above results is that the L/D ratio has a marked influence on the sloshing regime. A short tank, like $L/D = 2$, would probably reduce the sloshing-enhanced pressure drop onboard this specific ship. The second conclusion is that the diagram in Fig. 3.28 cannot be used to predict the lower resonance limit for tanks of different L/D. A long tank will have a higher period as its minimum, while a shorter tank will have a lower limit. In order to make a complete chart of the resonance zone for LNG fuel tanks, several more tank geometries must be tested. This can be done confidently by using CFD. Unfortunately, it needs to be left for future work.

The resulting pressure estimated by using CFD is shown in Fig. 3.37. The difference is significant. With the long tank, the pressure has dropped by 23 $\%$ in 30 seconds and continued dropping. In the short tank, the pressure was reduced by only 4%.

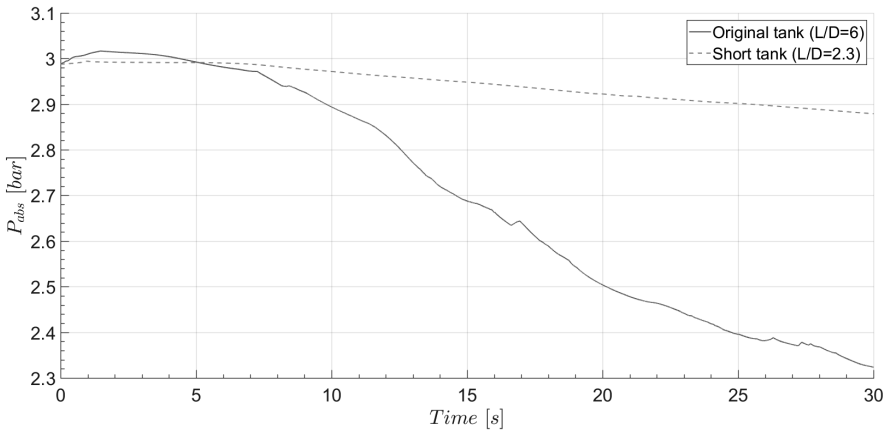

Figure 3.37: Sloshing-enhanced pressure drop compared between long and short full-scale tanks with the same volume. Pitch motion at 0 knots and head sea waves with a period of 10 [s].

Chapter 4

Summary of the Research

This thesis work has been carried out at NTNU in Ålesund (former Ålesund University College). The topic is the thermodynamic response in marine LNG fuel tanks enhanced by sloshing. The problem is the rapid loss of pressure experienced inside LNG fuel tanks on board a ship under severe motion in a seaway. Background information and a problem description were given in the introduction, as well as a list of research questions and objectives. The research was conducted with the use of experimental work, analysis, and numerical simulations. An experimental facility was designed and constructed to perform sloshing tests with both a transparent tank to study hydrodynamics and a pressure vessel made of steel. The pressure tank is insulated and special instruments for measuring pressure and temperature were used.

Fig. 4.1 provides an illustrative summary of the research. Numerical and experimental work were performed with a rectangular tank geometry to validate CFD tools and to investigate its applicability. A significant amount of studies exist that concern sloshing in rectangular tanks, while studies of the LNG fuel tank geometry are few. Studies with the rectangular tank have provided general knowledge about sloshing hydrodynamics and preparation for tests with the LNG tank geometry. Sloshing experiments have been performed with a transparent cylindrical tank. This was done to investigate the sloshing characteristics and to prepare for the thermal tests with the non-transparent steel tank. Numerical simulations are also compared to experiments. This gives the opportunity to vary more parameters, like amplitude, inner structure and tank form.

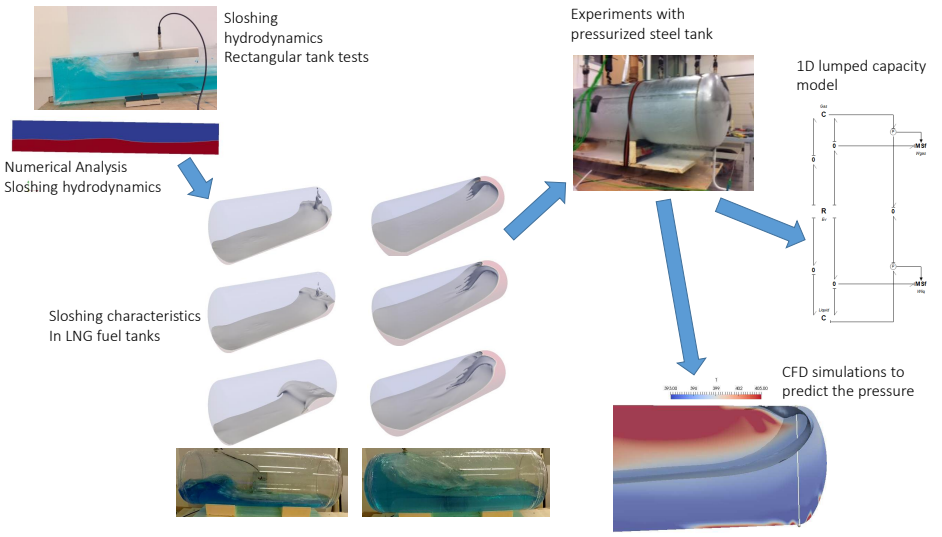

Figure 4.1: Summary of the research.

Thermal tests were performed with specific frequencies representing different sloshing regimes. These experiments provided us knowledge about the mechanisms responsible for the pressure drop by comparing the pressure and temperature measurements with the observed sloshing regimes. Analysis of experiments resulted in the development of theories and models that may be used to predict the thermodynamic response.

4.1 Overview of Papers

The following papers were prepared during the work with this thesis:

Paper 1: Grotle, Erlend Liavåg; Æsøy, Vilmar; Pedersen, Eilif. (2014) Modelling of LNG fuel systems for simulations of transient operations. *Maritime-Port Technology and Development*.

Paper 2: Grotle, Erlend Liavåg; Bihs, Hans; Pedersen, Eilif; Æsøy, Vilmar. (2016) CFD Simulations of Non-Linear Sloshing in a Rotating Rectangular Tank Using the Level Set Method. *ASME 2016 35th International Conference on Ocean, Offshore and Arctic Engineering, Volume 2: CFD and VIV,* doi:10.1115/OMAE2016-54533.

Paper 3: Grotle, Erlend Liavåg; Æsøy, Vilmar; Halse, Karl Henning; Pedersen,

Eilif; Li, Yue. (2016) Non-Isothermal Sloshing in Marine Liquefied Natural Gas Fuel Tanks. *Proceedings of the Twenty-sixth International Ocean and Polar Engineering Conference - ISOPE 2016, Rhodes Greece.*

Paper 4: Grotle, Erlend Liavåg; Bihs, Hans; Æsøy, Vilmar. (2017) Experimental and numerical investigation of sloshing under roll excitation at shallow liquid depths. *Ocean Engineering.* vol. 138(1), p.73-85. (https://doi.org/10.1016/j.oceaneng.2017.04.021).

Paper 5: Grotle, Erlend Liavåg; Æsøy, Vilmar. (2017) Experimental and Numerical Investigation of Sloshing in Marine LNG Fuel Tanks. *ASME 2017 36th International Conference on Ocean, Offshore and Arctic Engineering, Volume 1: Offshore Technology,* doi:10.1115/OMAE2017-61554.

Paper 6: Grotle, Erlend Liavåg; Æsøy, Vilmar. (2017) Dynamic modelling of the thermal response enhanced by sloshing in marine LNG fuel tanks. [*Revised manuscript submitted to Applied Thermal Engineering.*]

Paper 7: Grotle, Erlend Liavåg; Æsøy, Vilmar. (2017) Numerical Simulations of Sloshing and the Thermodynamic Response due to Mixing. *Energies*. vol. 10(9), 1338 (http://dx.doi.org/10.3390/en10091338).

A graphical overview of the papers with some keywords is given in Fig. 4.2. Papers in blue boxes are related to the experiments or the simulations of sloshing hydrodynamics, while papers in the orange boxes are related to experiments or simulations involving thermodynamics. This is in line with the scope of work (Fig. 1.4), which is divided into three fields of study: *sloshing hydrodynamics*, *heat- and mass transfer* and *LNG fuel systems*. The month and year of the paper's publication, or the duration of the writing process is given to the left of each box. All the papers can be found in Appendix A.

Figure 4.2: Papers overview. The color and location of the text boxes corresponds to the scope domain in Fig. 1.4.

4.2 Main Research Contributions

As stated in section 1.4, the overall objective is to improve operational reliability of LNG-fuelled vessels. Considering the research objectives, the results, the papers, and the existing literature, the following specific contributions can be listed:

C1: *An experimental facility has been designed and constructed to investigate both sloshing hydrodynamics and the thermodynamic response due to sloshing. CFD simulations were performed and good agreement with experimental results was found. A theoretical framework to predict the final state was developed and implemented into a lumped capacity model.*

C2: *New sloshing characteristics in LNG fuel tanks are pointed out. The spherical tank head has a significant influence on the sloshing with pronounced 3D effects.*

C3: *It was found that the time rate of change in pressure depends on the sloshing intensity, or more specifically the parameter $f/f_{1,0}$, while the difference between the initial and final states depends on the initial tank pressure and liquid bulk temperature. The pressure is influenced mainly by the mass transport between liquid and gas, and less by the gas superheating. Breaking waves seem to have greater impact on the pressure than sloshing with a fixed contact line.*

C4: *A global heat transfer coefficient was defined which correlates with $f/f_{1,0}$.*

C5: *The PBU power was estimated from the pressure measurements, and it corresponds to the power supply used in the experiments.*

C6: *A method to estimate the thermodynamic response was developed using CFD. Acceptable agreement with the experimental data was found under some conditions.*

Table 4.1: Relationships between research objectives, papers, and contributions.

Contribution	*Paper*	*Research objective*
C1	P2,P3,P4,P6	RO1
C2	P5	RO2
C3	P3,P6	RO3
C4	P6	RO4
C5	P6	RO5
C6	P7	RO6

4.3 Concluding Remarks

Development of the research methods, like the experimental facility and the numerical simulation tools, has provided excellent opportunities to study the problem considering the limited time and budget. The simulations of sloshing hydrodynamics using CFD are considered successful, and may replace the experiments involving hydrodynamics.

Knowledge about sloshing hydrodynamics was improved, and new characteristics were pointed out. Less time should have been spent on investigating rectangular tanks, although the studies were useful as a preparation.

The lumped capacity model is a good starting point for further analysis and model development. The framework is simple, but robust. The model may be used to develop correlations between a heat transfer coefficient and the frequency parameter $f/f_{1,0}$.

The use of CFD to simulate the pressure drop involves complex mechanisms, which may easily extend the scope beyond what is feasible. The local condensation phenomenon may prove even more important to the pressure drop than what can be modelled with CFD. As an example, it is still unknown how much the wetting of the walls matters. The presented model does not take this into account.

Considering the complexity of condensation processes, it seems the most feasible to conduct experiments. The challenge is to perform realistic experiments and to provide sufficient information about the condensation mechanisms. Prediction of the hydrodynamics is less challenging. If more details of the heat- and mass transfer mechanisms were known, only studies of the sloshing hydrodynamics would be necessary to provide the necessary engineering tools.

4.4 Suggestions for Future Work

The experimental facility has great potential, and several more tests should be performed with varying filling, frequency, and amplitude. However, detailed studies of the mechanisms may require better insulation and the ability to look inside the test tank. Constructing a vacuum-insulated transparent tank would be preferable.

To make a complete chart of the sloshing characteristics in LNG fuel tanks, the L/D ratio must be varied. The amplitude must also be changed to get a complete picture of the sloshing characteristics in LNG fuel tanks. All these investigations may be done with the use of CFD.

Of the fields of study mentioned in section 1.5 (Fig. 1.4), more independent studies of heat- and mass transfer must be performed. The thermal sloshing experiment may be broken down into a number of experiments to investigate these mechanisms in more detail. Examples are energy transfer via tank walls and the influence of the interface area and local mixing. Sloshing may be excluded to study only the mechanisms related to condensation.

The influence of baffles should be studied in more detail. It must be kept in mind that the baffles are not only changing the sloshing, but they may also contribute to the transport of heat. Both hydrodynamics and heat transfer mechanisms with baffles should be investigated in future work.

Bibliography

[1] ÆSØY, V., EINANG, P. M., STENERSEN, D., HENNIE, E., AND VALBERG, I. LNG-fuelled engines and fuel systems for medium-speed engines in maritime applications. Tech. rep., SAE Technical Paper, 2011.

[2] ÆSØY, V., AND STENERSEN, D. Low emission LNG fuelled ships for environmental friendly operations in arctic areas. In *ASME 2013 32nd International Conference on Ocean, Offshore and Arctic Engineering* (2013), American Society of Mechanical Engineers, pp. V006T07A028–V006T07A028.

[3] ARNDT, T. *Sloshing of Cryogenic Liquids in a Cylindrical Tank under normal Gravity Conditions*. Universtität Bremen, 2011.

[4] BERTHELSEN, P. A., AND FALTINSEN, O. M. A local directional ghost cell approach for incompressible viscous flow problems with irregular boundaries. *Journal of computational physics 227*, 9 (2008), 4354–4397.

[5] BIHS, H. *REEF3D, User Guide*, 2016.

[6] BIHS, H., KAMATH, A., CHELLA, M. A., AGGARWAL, A., AND ARNTSEN, Ø. A. A new level set numerical wave tank with improved density interpolation for complex wave hydrodynamics. *Computers & Fluids 140* (2016), 191–208.

[7] BOTIA VERA, E., SOUTO IGLESIAS, A., BULIAN, G., AND LOBOVSKỲ, L. Three sph novel benchmark test cases for free surface flows.

[8] CONTROLLAB PRODUCTS. 20-sim. `http://www.20sim.com`, 2017. [Online; accessed 15-October-2017].

[9] DURBIN, P. Limiters and wall treatments in applied turbulence modeling. *Fluid dynamics research 41*, 1 (2009), 012203.

[10] EINANG, P. M. Gas-fuelled ships. *CIMAC paper 261* (2007).

[11] FALTINSEN, O. M., AND TIMOKHA, A. N. *Sloshing*. Cambridge University Press, 2009.

[12] FERZIGER, J. H., AND PERIC, M. *Computational methods for fluid dynamics*. Springer Science & Business Media, 2012.

[13] GHIAASIAAN, S. M. *Two-phase flow, boiling, and condensation: in conventional and miniature systems*. Cambridge University Press, 2007.

[14] GREENSHIELDS, C. Openfoam user guide. version 4.0. *OpenFOAM Foundation Ltd* (2016).

[15] GROTLE, E., ÆSØY, V., AND PEDERSEN, E. Modelling of LNG fuel systems for simulations of transient operations. CRC Press, pp. 205–215.

[16] GROTLE, E. L., AND ÆSØY, V. Experimental and numerical investigation of sloshing in marine LNG fuel tanks. In *ASME 2017 36th International Conference on Ocean, Offshore and Arctic Engineering* (2017), American Society of Mechanical Engineers, pp. V001T01A046–V001T01A046.

[17] GROTLE, E. L., AND ÆSØY, V. Numerical simulations of sloshing and the thermodynamic response due to mixing. *Energies 10*, 9 (2017), 1338.

[18] GROTLE, E. L., BIHS, H., AND ÆSØY, V. Experimental and numerical investigation of sloshing under roll excitation at shallow liquid depths. *Ocean Engineering 138* (2017), 73–85.

[19] GROTLE, E. L., BIHS, H., PEDERSEN, E., AND ÆSØY, V. CFD simulations of non-linear sloshing in a rotating rectangular tank using the level set method. In *ASME 2016 35th International Conference on Ocean, Offshore and Arctic Engineering* (2016), American Society of Mechanical Engineers, pp. V002T08A019–V002T08A019.

[20] GROTLE, E. L., HALSE, K. H., PEDERSEN, E., AND LI, Y. Non-isothermal sloshing in marine liquefied natural gas fuel tanks. In *The 26th International Ocean and Polar Engineering Conference* (2016), International Society of Offshore and Polar Engineers.

[21] IBRAHIM, R. A. *Liquid sloshing dynamics: theory and applications*. Cambridge University Press, 2005.

[22] KARNOPP, D. C. State variables and pseudo bond graphs for compressible thermofluid systems. *Journal of Dynamic Systems, Measurement, and Control 101*, 3 (1979), 201–204.

[23] KREITH, F., AND BOEHM, R. F. *Direct-contact heat transfer*. Springer Science & Business Media, 2013.

[24] LA ROCCA, M., SCIORTINO, G., AND BONIFORTI, M. A. A fully nonlinear model for sloshing in a rotating container. *Fluid Dynamics Research 27*, 1 (2000), 23–52.

[25] LEMMON, E. W., HUBER, M. L., AND MCLINDEN, M. O. NIST Standard Reference Database 23: Reference Fluid Thermodynamic and Transport Properties-REFPROP, Version 9.1, National Institute of Standards and Technology, 2013.

[26] LIN, C. S., VAN DRESAR, N. T., AND HASAN, M. M. Pressure control analysis of cryogenic storage systems. *Journal of propulsion and power 20*, 3 (2004), 480–485.

[27] LUDWIG, C., DREYER, M., AND HOPFINGER, E. Pressure variations in a cryogenic liquid storage tank subjected to periodic excitations. *International Journal of Heat and Mass Transfer 66* (2013), 223–234.

[28] MOKHATAB, S., MAK, J. Y., VALAPPIL, J. V., AND WOOD, D. A. *Handbook of liquefied natural gas*. Gulf Professional Publishing, 2013.

[29] MOKSNES, P. O. Modeling two-phase thermo-fluid systems using bond graph. *Dr. ing thesis, University of Sciences and Technology, Department of Marine Engineering, Norway* (1997).

[30] MORAN, M. E., MCNELIS, N. B., KUDLAC, M. T., HABERBUSCH, M. S., AND SATORNINO, G. A. Experimental results of hydrogen slosh in a 62 cubic foot (1750 liter) tank, 1994.

[31] MORAN, M. J., SHAPIRO, H. N., BOETTNER, D. D., AND BAILEY, M. B. *Fundamentals of engineering thermodynamics*, 5th. ed. John Wiley & Sons, 2003.

[32] MOUKALLED, F., MANGANI, L., AND DARWISH, M. *The Finite Volume Method in Computational Fluid Dynamics: An Advanced Introduction with OpenFOAM® and Matlab*, vol. 113. Springer, 2015.

[33] MURRAY, F. W. On the computation of saturation vapor pressure. Tech. rep., RAND CORP SANTA MONICA CALIF, 1966.

[34] RUSCHE, H. *Computational fluid dynamics of dispersed two-phase flows at high phase fractions*. PhD thesis, Imperial College London (University of London), 2003.

[35] SIDEMAN, S., AND MOALEM-MARON, D. Direct contact condensation. *Advances in Heat Transfer 15* (1982), 227–281.

[36] SINTEF. ShipX. `https://www.sintef.no/en/software/shipx/`, 2017. [Online; accessed 15-October-2017].

[37] THOMA, J., AND BOUAMAMA, B. O. *Modelling and simulation in thermal and chemical engineering: A bond graph approach*. Springer Science & Business Media, 2013.

[38] WU, C.-H., FALTINSEN, O. M., AND CHEN, B.-F. Numerical study of sloshing liquid in tanks with baffles by time-independent finite difference and fictitious cell method. *Computers & Fluids 63* (2012), 9–26.

Appendix A

Main Papers

Paper I

Paper 1 - Modelling of LNG fuel systems for simulations of transient operations.

Grotle, Erlend Liavåg; Æsøy, Vilmar; Pedersen, Eilif. (2014)
Maritime-Port Technology and Development.

Is not included due to copyright

Paper II

Paper 2 - CFD Simulations of Non-Linear Sloshing in a Rotating Rectangular Tank Using the Level Set Method.

Grotle, Erlend Liavåg; Bihs, Hans; Pedersen, Eilif; Æsøy, Vilmar. (2016)
ASME 2016 35th International Conference on Ocean, Offshore and Arctic Engineering, Volume 2: CFD and VIV.
doi:10.1115/OMAE2016-54533.

Is not included due to copyright

Paper III

Paper 3 - Non-Isothermal Sloshing in Marine Liquefied Natural Gas Fuel Tanks.

Grotle, Erlend Liavåg; Æsøy, Vilmar; Halse, Karl Henning; Pedersen, Eilif; Li, Yue. (2016)

Proceedings of the Twenty-sixth International Ocean and Polar Engineering Conference - ISOPE 2016, Rhodes Greece.

Is not included due to copyright

Paper IV

Paper 4 - Experimental and numerical investigation of sloshing under roll excitation at shallow liquid depths.

Grotle, Erlend Liavåg; Bihs, Hans; Æsøy, Vilmar. (2017)
Ocean Engineering. vol. 138(1), p.73-85.
(https://doi.org/10.1016/j.oceaneng.2017.04.021).

Ocean Engineering 138 (2017) 73–85

Contents lists available at ScienceDirect

Ocean Engineering

journal homepage: www.elsevier.com/locate/oceaneng

Experimental and numerical investigation of sloshing under roll excitation at shallow liquid depths

Erlend Liavåg Grotle[a,*], Hans Bihs[b], Vilmar Æsøy[a]

[a] Department of Maritime Technology and Operations, Norwegian University of Science and Technology (NTNU), NO-6009 Ålesund, Norway
[b] Department of Civil and Transport Engineering, Norwegian University of Science and Technology (NTNU), NO-7491 Trondheim, Norway

ARTICLE INFO

Keywords:
Sloshing
Experiments
RANS
Shallow depths
Resonance zone

ABSTRACT

This paper investigates sloshing at shallow-liquid depths in a rectangular container by using experimental and numerical methods. A motion platform is used to perform a prescribed periodic rotational motion to excite the liquid sloshing at a range of frequencies and filling levels. Simulated free-surface elevation is compared with the experimental results for a selection of cases. The wave mechanisms at the chosen fillings are studied by combining numerical methods and the experimental results. We find that the simulated free-surface elevation is in close agreement with experimental results inside the resonance zone. But at frequencies above the bifurcation point, with several overlapping waves, the deviation is increasing. The bifurcation point is determined for a range of filling levels through observation. The numerical results provide important information about sloshing mechanisms at these depths. Complex interaction between the bottom, the lower layer and the wave influences the amount of dissipation before the wave hits the wall. The existing theory seems to be too conservative in predicting the occurrence of hydraulic jumps in the upper limit.

1. Introduction

Sloshing can be characterized as the motion of liquids in containers or vessels. Sloshing can occur with more than one immiscible liquid, as studied in Rocca et al. (2002) and La Rocca et al. (2005). There are several applications in which sloshing may occur. The basic problem sloshing presents is estimating the hydrodynamic pressure distribution, forces, moments, and natural frequencies. Extensive work on how to approach it analytically can be found in Ibrahim (2005) and Faltinsen and Timokha (2009). The former focuses on space applications, while the latter focuses on sloshing within the maritime field. Naturally, a moving ship in waves is subject to sloshing. Within the maritime field there are tanks of different applications, but in general all marine vehicles have some kind of tank installed on-board. Examples are roll-stabilizer tanks or cargo tanks carrying different type of liquids. Impact at shallow depths can cause great damage to the tank. The resonance zone extends to frequencies higher than the calculated first natural frequency. Depending on the depth, frequencies below the first natural frequency result in a bore (Olsen and Johnsen, 1975; Peregrine and Svendsen, 1978). By increasing the frequency, it is possible to cause the bore to travel all the way from one wall to the other. Further increase of the frequency results in a narrow region where a steep solitary wave travels the entire tank length without breaking, and this results in severe impact on the side walls. This paper aims to characterize wave patterns in a sloshing tank under roll and to identify frequencies that cause severe impacts at low fillings.

There are many methods to analyse sloshing and several studies use experimental or analytical approaches to examine the subject. Olsen and Johnsen (1975) characterized sloshing at these depths and performed a limited number of tests with forced roll. Armenio and Rocca (1996) investigated sloshing with forced and free oscillations at shallow depths under rolling motion. The roll amplitude varies between 1.0° and 4.5° with two different depths. They compare results using the shallow water equations (SWE) form of the Navier-Stokes equations and RANS equations, and they found higher accuracy with RANS than with SWE. La Rocca et al. (2000) and Mele and Armenio (1997) also performed theoretical and experimental analysis of sloshing in a rotating container at intermediate depths. A fully nonlinear model is defined by applying the variational method. A technique to select the most energetic modes from experimental tests is presented. The comparison between experiments and theory shows good agreement.

To investigate the detailed flow conditions in sloshing, both with and without internal structures, computational fluid dynamics (CFD) provide promising capabilities. Viscous dissipation is accounted for and wave breaking regimes can be modelled with good accuracy. The literature offers several studies. Gómez-Goñi et al. (2013) compared

* Corresponding author.
E-mail address: erlend.l.grotle@ntnu.no (E.L. Grotle).

http://dx.doi.org/10.1016/j.oceaneng.2017.04.021
Received 11 September 2016; Received in revised form 12 March 2017; Accepted 16 April 2017

two CFD tools using the volume of fluid method (VOF) and a multi-modal sloshing model by Ansari et al. (2011). They found good agreement between the two CFD codes, but the multi-modal method over-predicted the wave amplitude in some conditions. Bai et al. (2015) used a finite difference CFD model to simulate a full scale LNG tank undergoing realistic ship motions. To capture the free surface, a level-set method is employed. To validate the simulations, both longitudinal and rotational motions are considered. Few cases that compared free-surface elevation are considered. The comparison of pressure data showed acceptable agreement. Zhao and Chen (2015) implemented a finite-analytical NavierStokes (FANS) flow solver in conjunction with a new coupled level-set and VOF method (CLSVOF). Impact pressure from simulations are compared with experimental data and shows good agreement. They also compared the method to a level-set method with global mass conservation and found that the CLSVOF method showed an significant reduction in the relative mass change.

An increasing trend is to use large-eddy simulations (LES), but this comes at a computational cost, which increases with higher Reynolds number. Liu and Lin (2008) simulated sloshing in a three-dimensional tank using LES with the Smagorinsky subgrid scale model. However, their comparisons only concern non-linear sloshing conditions, excluding the resonant case. The cases with violent sloshing were not validated against experimental data.

Another method that has proven promising in predicting wave motions in sloshing is smooth particle hydrodynamics (SPH). Iglesias et al. (2004) performed SPH simulations of passive anti-roll tanks. The phase-lag for the roll moment is compared to experimental results for different fillings and roll amplitudes. Bouscasse et al. (2013) investigated shallow depth sloshing for sway. They compared experimental results with a δ-SPH scheme and found that the method proved to be robust and reliable in studying violent free-surface flows. An extensive experimental program is presented, with several amplitudes and fillings. An additional classification of the wave patterns by Olsen and Johnsen (1975) are presented. Delorme et al. (2009) and Bulian et al. (2010) also compare SPH simulations and experiments.

The numerical model, REEF3D (Bihs et al., 2016; Bihs and REEF3D, 2016) which we use in this work is based on discretization and solving the Reynolds-averaged Navier-Stokes equations (RANS). The novelties of the RANS simulations are the use of level-set method and the improved turbulence boundary condition at the free surface. The model has been extensively used for wave hydrodynamics problems (Chella et al., 2015), ocean wave energy (Kamath et al., 2015) and sediment transport problems (Afzal et al., 2015). Forced sloshing within the proximity of the first mode natural frequency as well as free sloshing is simulated and compared to experiments performed at the lab facility at the Norwegian University of Science and Technology (NTNU) in Ålesund. Together with the high-order numerical treatment of the governing equations, this leads to high-quality simulation results, as shown through the comparison with the measured data in the first part of the paper. In the second part, investigation of the resonance zone at shallow depth sloshing is performed. The mean wave amplitude and bifurcation point is determined for a range of fillings. The combination of RANS simulations and experimental observations has led to an improved representation of the sloshing hydrodynamics.

2. Numerical model

2.1. RANS equations

The governing equations are the incompressible RANS equations given in tensor notations valid for two and three dimensions:

$$\frac{\partial \overline{u}_i}{\partial t} + \overline{u}_j\frac{\partial \overline{u}_i}{\partial x_j} = -\frac{1}{\rho}\frac{\partial \overline{p}}{\partial x_i} + \frac{\partial}{\partial x_j}\left[(\nu + \nu_t)\left(\frac{\partial \overline{u}_i}{\partial x_j} + \frac{\partial \overline{u}_j}{\partial x_i}\right)\right] + S_i \tag{1}$$

Where u is the velocity, p the pressure, ρ the density and ν and ν_t are the viscosity and turbulent eddy-viscosity respectively. The last term are the body forces. Since we are using a tank-fixed coordinate system, source terms in addition to gravity must be accounted for to represent the equations in a non-inertial global system. The motion is harmonic, and the x- and z-terms are given by:

$$\begin{aligned} S_x &= \ddot{\theta}(z - z_m) + \dot{\theta}^2(x - x_m) - g\sin\theta, \\ S_z &= -\ddot{\theta}(x - x_m) + \dot{\theta}^2(z - z_m) - 2\dot{\theta}\overline{u} - g\cos\theta. \end{aligned} \tag{2}$$

where the z-component is the vertical direction and x is in the longitudinal direction of the tank. As the motion is planar, no source term is added for the y-component. θ is the rotational angle. $\dot{\theta}$, $\ddot{\theta}$ is angular velocity and acceleration respectively. The coordinates x_m and z_m are center of the rotational point, and therefore $x - x_m$ is the distance from the rotational point to the center of the tank fixed coordinate system. The second last term of the z-component is the *Coriolis* acceleration.

2.2. Turbulence

Modelling turbulence in sloshing, or general free surface flow with large density ratios, is complex. To calculate the velocities and pressure of Eq. (1), an expression for the eddy-viscosity is needed. The two-equation, k-ω turbulence model is used to close the set of equations (Wilcox, 1994). These are the kinetic turbulent energy and the specific dissipation rate of turbulent energy, ω. The equations can be written (Wilcox, 1988):

$$\frac{\partial k}{\partial t} + \overline{u}_j\frac{\partial k}{\partial x_j} = \frac{\partial}{\partial x_j}\left[\left(\nu + \frac{\nu_t}{\sigma_k}\right)\frac{\partial k}{\partial x_j}\right] + P_k - \beta_k k\omega \tag{3}$$

$$\frac{\partial \omega}{\partial t} + \overline{u}_j\frac{\partial \omega}{\partial x_j} = \frac{\partial}{\partial x_j}\left[\left(\nu + \frac{\nu_t}{\sigma_\omega}\right)\frac{\partial \omega}{\partial x_j}\right] + \frac{\omega}{k}\alpha P_k - \beta\omega^2 \tag{4}$$

P_k is the turbulent energy production term. σ_k, σ_ω are standard coefficients in the model, both with values of 2 in this case. β_k, β and α are empirical constants, with values 9/100, 3/40 and 5/9 respectively. The RANS model overproduces the turbulent energy in highly strained flows. This gives unrealistically large values for the eddy-viscosity. Menter (1994) noted that the stress intensity ratio scales with the ratio of turbulence production to dissipation. Typical stress intensity ratios can be found from experiments in certain type of flows. In order to avoid overproduction of turbulence in highly strained flow outside the boundary layer, the turbulent eddy-viscosity, ν_t, can be bounded through the limiting formulation (Durbin, 2009):

$$\nu_t = \min\left(\frac{k}{\omega}, \sqrt{\frac{2}{3}}\frac{k}{|\mathbf{S}|}\right) \tag{5}$$

where $|\mathbf{S}|$ is the rate of strain.

The rough wall function by Schlichting (1979) is applied to solid boundaries (Bihs and REEF3D, 2016):

$$u^+ = \frac{1}{\kappa}ln\left(\frac{30y}{k_s}\right). \tag{6}$$

u^+ is the dimensionless wall velocity, κ is a constant equal to 0.4 and k_s is the equivalent sand roughness. Near the wall it is assumed that the turbulent production is equal to the dissipation of turbulent energy. This gives the following expression for the specific turbulent dissipation:

$$\omega_{wall} = -\frac{C_\mu^{3/4}k_w^{1/2}u_w^+}{\Delta y_p} \tag{7}$$

where Δy_p is the distance from the wall to the respective cell.

The initial conditions for the velocity field are calculated from potential flow. The turbulence starting values are based on turbulence intensity and viscosity ratio.

At the free surface it seems plausible that the turbulent length scales are reduced. This is a similar effect as on the wall boundaries, where a shear layer is formed due to forces near the surface. The normal fluctuations are damped out, with an amplification of the other components. A boundary condition is proposed to limit the length scale near the free surface (Naot and Rodi, 1982):

$$\omega_s = \frac{C_\mu^{-1/4}}{\kappa} k^{1/2} . \frac{1}{y'} \tag{8}$$

where $C_\mu = 0.07$ and $\kappa = 0.4$. y' is the virtual origin of the length scale of the turbulence. In Hossain and Rodi (1980) this was determined to be 0.07 times the mean water depth. To activate this boundary condition at the interface of thickness ϵ, the expression is multiplied by the Dirac delta function:

$$\delta(\phi) = \begin{cases} \frac{1}{2\epsilon}[1 + \cos(\frac{\pi\phi}{\epsilon})], & \text{if} |\phi| < \epsilon; \\ 0, & \text{otherwise} \end{cases} \tag{9}$$

where ϕ is the level set function. It should be noted that Eq. (5), limits the eddy-viscosity in the whole flow domain. The free surface boundary condition of ω in Eq. (8) increases the dissipation and therefore reduces the eddy-viscosity, but only at the free surface.

2.3. Interface capturing

The interface between liquid and gas represent a discontinuity in the fluid properties. To capture the interface, the level set technique is used, first presented by Osher and Sethian (1988). The location of the surface is represented by the zero level of a signed distance function. The following properties are defined:

$$\phi(\mathbf{x}, t) \begin{cases} >0, & \text{if } \mathbf{x} \in \text{phase 1}; \\ =0, & \text{if } \mathbf{x} \in \Gamma; \\ <0, & \text{if } \mathbf{x} \in \text{phase 2} \end{cases} \tag{10}$$

Where Γ represents the free surface. In order to move the interface inside a velocity field, a transport equation for the level set function, ϕ, is solved. The equation is given as:

$$\frac{\partial \phi}{\partial t} + \bar{u}_j \frac{\partial \phi}{\partial x_j} = 0 \tag{11}$$

The convective term in Eq. (11) is discretized with the Hamilton-Jacobi version of the weighted essentially non-oscillatory scheme (WENO HJ). The temporal term is solved with the third-order TVD Runge-Kutta scheme (Osher and Sethian, 1988). When the level set function is convected, it will not remain a signed distance function. To maintain this property, it must satisfy the Eikonal equation, $|\nabla\phi| = 1$. Reinitialization at each time step is done using a PDE based equation (Sussman et al., 1994), (Peng et al., 1999). Preserving mass conservation poses a challenge when there are significant deformations of the free surface. Some recent advances are found in Nourgaliev et al. (2005) and Sussman et al. (1998).

The mixture density in each cell center is evaluated using the smoothed Heaviside function as:

$$\begin{aligned} \rho(\phi) &= \rho_1 H(\phi) + \rho_2[1 - H(\phi)] \\ \mu(\phi) &= \mu_1 H(\phi) + \mu_2[1 - H(\phi)] \end{aligned} \tag{12}$$

where ρ_1 and ρ_2 are the densities in phase 1 and 2 respectively. The Heaviside function is defined as

$$H(\phi_i) = \begin{cases} 0, & \text{if } \phi_i < -\epsilon; \\ \frac{1}{2}\left[1 + \frac{\phi_i}{\epsilon} + \frac{1}{\pi}\sin\left(\frac{\pi\phi_1}{\epsilon}\right)\right], & \text{if} |\phi_i| < \epsilon; \\ 1, & \text{if } \phi_i > \epsilon \end{cases} \tag{13}$$

Treatment of the abrupt change of fluid properties is needed, and to avoid numerical instabilities, the values are smoothed across the free surface. This can be done by assigning a finite thickness to the interface. Typically the thickness is equal to $\epsilon = 1.6\Delta x$, where Δx is the grid spacing.

Using a staggered grid, the density must also be evaluated at the cell faces to find the fluxes. Performing this in two steps, by interpolation of the densities at the cell center, leads to small scale oscillations. Instead, the cell face densities are calculated in a single step with the smoothed Heaviside function:

$$\rho_{i+1/2} = \rho_1 H(\phi_{i+1/2}) + \rho_2[1 - H(\phi_{i+1/2})] \tag{14}$$

where the level set function at the cell faces is evaluated through averaging:

$$\phi_{i+1/2} = \frac{1}{2}(\phi_i + \phi_{i+1}) \tag{15}$$

2.4. Solution procedure

Chorin's projection method (Chorin, 1968) is used to handle the pressure-velocity coupling. This procedure starts with computing an intermediate velocity field by ignoring the pressure terms in the RANS equations. This is the predictor step. In the next projection step the pressure gradient is added to give the final velocity at the next time step. The continuity condition is used to eliminate $\bar{u}^{n+1}$, to get the Poisson equation:

$$\frac{\partial}{\partial x_i}\left(\frac{1}{\rho}\frac{\partial p}{\partial x_i}\right) = \frac{1}{\Delta t}\frac{\partial \bar{u}_i^*}{\partial x_i} \tag{16}$$

The equation is iteratively solved to find the pressure at the new time step. Integration of Parallel High Performance Preconditioners (HYPRE) with REEF3D makes it possible to combine a conjugate gradient solver with geometric multigrid preconditioning (Center for Applied Scientific Computing, 2015).

The convective terms in the RANS equation are discretized using the conservative fifth-order WENO scheme (Jiang and Shu, 1996). A non-conservative WENO scheme (WENO HJ) is used to discretize the convective terms in the level set equation, the k and ω equations. Essentially non-oscillatory schemes (ENO) bring higher order to the first order upwind schemes by polynomial interpolation of the flux functions. There are three possible HJ ENO approximations to the fluxes. WENO uses a weight parameter and combines the three stencils.

The grid is uniform and orthogonal. Construction of this is done quite easily in the rectangular domain. The ghost cell method (Berthelsen and Faltinsen, 2008) is implemented to account for solid boundaries.

3. Experimental set-up and results

The experiments were carried out at the Department of Maritime Technology and Operations at NTNU Ålesund. A solid rotational

Table 1
Tank configurations.

Tank config.	$L[m]$	$B[m]$	$H[m]$	s/L	Test type
1	1.00	0.25	0.40	0.408	Main test
2	0.59	0.18	0.3	0.408	Comparison and $h/L = 0.125$

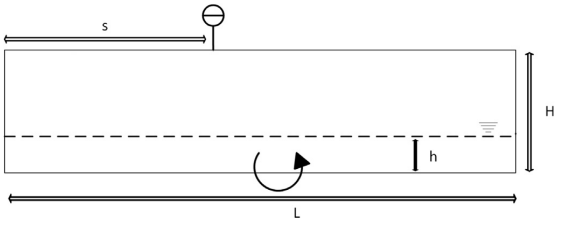

Fig. 1. Tank configuration.

platform is used to excite sloshing. A crank mechanism driven by an electro motor creates the rotational motion of a plane table. Two different tanks have been used, the smallest one to test $h/L = 0.125$, because it required depths that would result in tank-roof impacts with the longest tank. The main dimensions are given in Table 1. An explanation of the dimensions is given in Fig. 1. Validation results are performed by placing the sensor slightly to the left in Fig. 1, while the free-surface amplitude from experiments is measured also at the middle of the tank, $x/L = 0.500$. Several fillings are also tested with the small tank to compare the results with the long tank. This can be done by scaling the frequencies based on the tank lengths, so that $f_2 = f_1 \cdot \sqrt{L_1/L_2}$, where L_1 and f_1 is the length and frequency of the long tank respectively.

The roll axis is at the intersection of the bottom and the centerplane of the tank, creating liquid motions in the longitudinal direction (Fig. 1). Videos of all the sloshing tests are recorded, using a GoPro Hero4 camera. The distance from the tank top to the free surface is measured using an ultrasonic sensor, type Sick UM12. The resolution of the sensor is 0.069 mm. The accuracy is ±1% with a repeatability of ±0.15% based on the current measurement value. If it is assumed that the percentage accuracy is valid also for a measured distance of 100 mm, the potential error would be 1 mm. The operating range of the sensor is 20–150 mm. The location of the sensor is close to the middle of the tank, with a distance of $s/L = 408$ from the left side.

The varied test parameters are the frequency of motion and the filling level. The roll amplitude is kept equal to 3 degrees in all tests. The tank breadth is small relative to the length, so that 3D effects are negligible. This is also seen from the 3D simulation results. The test parameters are given in Table 2. The test runs for each filling are performed continuously by adjusting frequency at small steps after several cycles with each frequency.

3.1. Wave amplitude and the bifurcation point

The free-surface elevation for a range of frequencies and fillings is found from measurements in the tank test. The sensor location is close to the middle, and as already shown, the amplitude is slightly different when passing each way. As the wave starts to travel all the way without breaking from wall to wall, the amplitude is almost similar, and the dominating frequency is $2{\cdot}f$. To identify the amplitude-frequency curve of each filling, it would make sense to calculate the average of the two amplitudes of each pass (right to left and left to right). The free-surface elevation is therefore calculated as the mean value of the positive peaks, being the wave passing from left to right and opposite:

$$\bar{\eta} = \frac{1}{N}\sum_{i=1}^{N}\eta_i \tag{17}$$

where N is the total number of positive peaks within the time series and η_i is wave peak number i of each passing. The resulting wave amplitude for a selection of fillings is shown in Fig. 2.

To find the repeatability of the measured peaks within each test of constant motion frequency, the standard deviation is found for each of the wave peaks, defined as

$$S = \sqrt{\frac{1}{N-1}\sum_{i=1}^{N}|\eta_i - \bar{\eta}|}\,. \tag{18}$$

It is found that the standard deviation could be as high as 15% of the respective wave elevation, but on average it is 10%. The number of sloshing cycles is 30 for each frequency. This means that the repeatability of the amplitude within a test of several sloshing cycles is relatively low. The absolute values should therefore be considered with care, but the curves in Fig. 2 show interesting trends. There seems to be a marked difference between the depth $h/L = 0.07$ and $h/L = 0.08$, as the wave amplitudes at $h/L = 0.08$ are more significant for a broader range of frequencies. The sections below show how the filling affects the speed of the wave, breaking or non-breaking, as it approaches the side wall. The dissipation is quite different between the different fillings. The rapid increase seen for $h/L = 0.08$ close to $f/f_{1,0} = 1$ is because the wave breaks close to the middle or slightly across it.

At a certain frequency parameter, $f/f_{1,0}$, the wave amplitude drops significantly. The frequency when this occurs is higher for smaller fillings. The zone where impacts are more severe is also narrower for smaller depths. Through observation it is found which frequencies result in the characteristic solitary wave followed by the *bifurcation* point. In a practical sense, the definition is such that a small change in

Table 2
Test parameters, minimum and maximum frequencies of each filling.

Test no.	h/L	f[Hz]	$f/f_{1,0}$	Tank config.
1	0.030	0.233–0.483	0.861–1.785	1
2	0.040	0.300–0.500	0.960–1.601	1
3	0.050	0.300–0.533	0.860–1.529	1/2
4	0.060	0.300–0.600	0.787–1.573	1
5	0.070	0.333–0.633	0.811–1.541	1/2
6	0.080	0.300–0.633	0.684–1.445	1
7	0.090	0.333–0.617	0.719–1.330	1
8	0.100	0.367–0.627	0.752–1.287	1/2
9	0.125	0.500–0.633	0.926–1.173	2

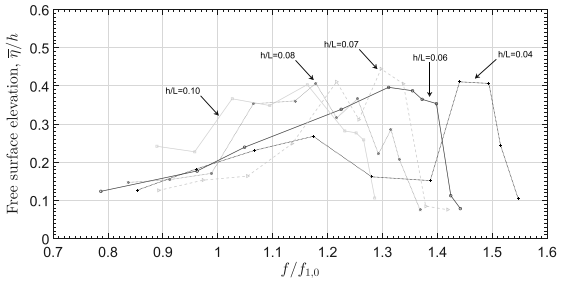

Fig. 2. Wave amplitude.

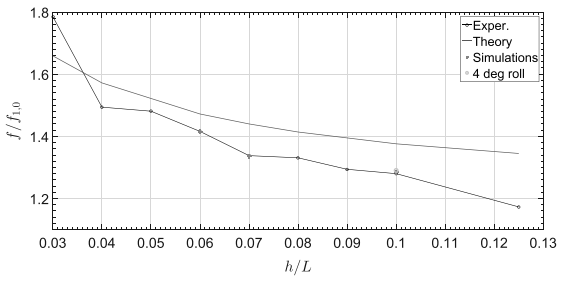

Fig. 3. The bifurcation frequency (experiments and simulations) and the theoretical prediction of the upper range of hydraulic jumps to occur.

$f/f_{1,0}$ causes a sudden topological change in the long-term dynamic behaviour of the system (Faltinsen and Timokha, 2009). This point is accurately determined by gradually varying the frequencies, and observing at which frequency it occurs.

The bifurcation frequency for all the tested fillings is presented in Fig. 3. It has been determined for a few fillings at 3 degree roll using simulations. 4 degree roll amplitude has also been determined with REEF3D only at filling $h/L = 0.10$. The bifurcation parameter $f/f_{1,0}$ is slightly higher with 4 degree roll. Several more amplitude and filling combinations should be investigated for the future. This may be done with our numerical tool.

The curve is steeper for low fillings, and flattens out as the filling level passes $h/L = 0.06$. The flat curve at high fillings indicates that the sloshing enters the intermediate depth region. Comparison with the smaller tank (number 2) resulted in the same parameter $f/f_{1,0}$ with the tested fillings and scaled frequencies. In the same figure, the upper range of hydraulic jumps to occur according to the theory by Verhagen and Wijngaarden (1965) is shown. The formula is given in Eq. (19). It should be noted that the theoretical prediction is not a prediction of the bifurcation point. But as it predicts a higher frequency parameter for $h/L > 0.04$, the guidance is poor. Using the theoretical prediction in the upper range will therefore result in a too wide range for resonant conditions to be present.

$$|1 - f/f_{1,0}| \leq \pi^{-2}\sqrt{24}\sqrt{L\eta_{4a}/h + \pi^2 Z_r \eta_{4a}/L} \tag{19}$$

4. Numerical investigation of shallow-depth sloshing

4.1. Grid sensitivity study

In this section, the simulation and experiment results are compared and discussed. A grid sensitivity study is presented at first, followed by the comparison between experiments and simulations for some selected cases. The numerical set-up is meant to closely represent the experimental test. A rectangular domain with orthogonal and uniform cells is constructed. The rotation point similar to Fig. 1 is chosen, and motion is generated through the momentum source terms, as described in Eq. (2). Three different cell sizes are compared for test number 4 with $h/L = 0.06$ and the frequency corresponding to the bifurcation point ($f/f_{1,0} = 1.40$). Only two-dimensional simulations are compared. The resulting free-surface elevation is shown in Fig. 4. It is found that the highest peak is slightly lower with finer grid where the amplitude is slightly over-predicted by the RANS simulations. As the simulation with grid $\Delta x/L = \Delta y/L = 0.003$ is significantly more efficient than the finest grid, it is therefore chosen for further studies. The number of grid cells is equal to 33,300 in the two-dimensional case.

4.2. Comparison of free-surface elevation

The comparison between experiments and simulations is based on the measured free-surface elevation. The results from tests with water elevation $h/L = 0.06$ are plotted in Fig. 5a–d respectively. The simulated amplitude of the wave travelling back and forth is in close agreement with the experiments. Any discrepancy is due to ripples at the back of the wave and a free-surface profile at the wave front. It was observed during experiments that the wave front is chaotic as it breaks. The sensor is placed somewhat to the left of the middle. In Fig. 5c, it can be seen that the two peaks have almost the same amplitude. This is because the amplitude of the travelling wave only differs slightly when passing each direction. This indicates that this is almost a single solitary wave just prior to the bifurcation point.

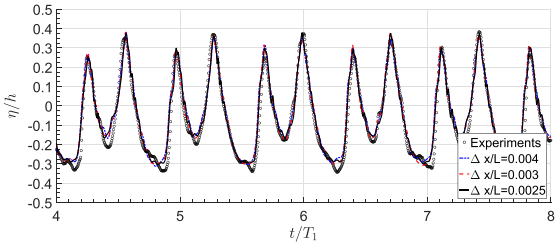

Fig. 4. Grid sensitivity for case $h/L = 0.06$ and $f/f_{1,0} = 1.40$.

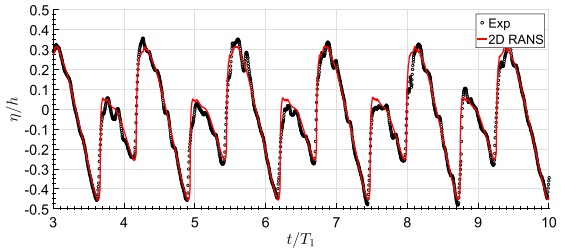

(a) $h/L = 0.06$ and $f/f_{1,0} = 0.79$.

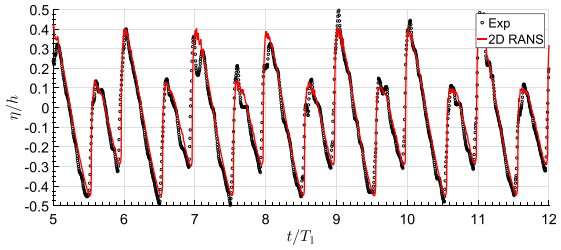

(b) $h/L = 0.06$ and $f/f_{1,0} = 1.00$.

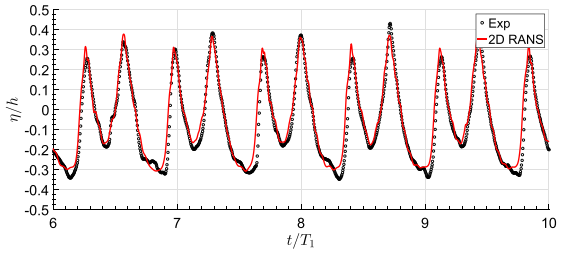

(c) $h/L = 0.06$ and $f/f_{1,0} = 1.40$.

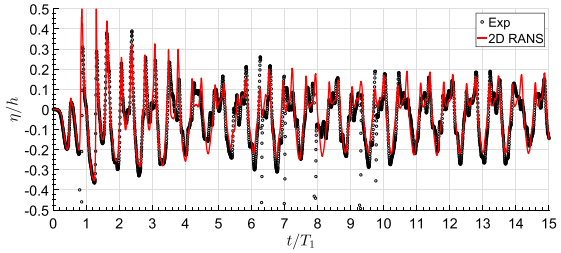

(d) $h/L = 0.06$ and $f/f_{1,0} = 1.44$.

Fig. 5. Free-surface elevation at forced sloshing.

4.3. Simulations of free sloshing

Free sloshing is investigated by turning off the motion after half a

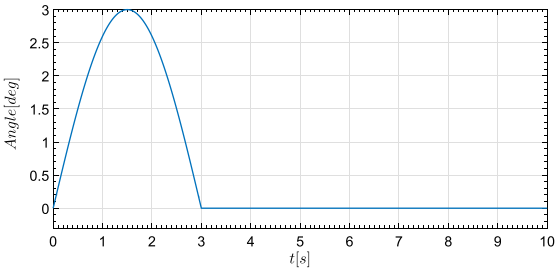

Fig. 6. Motion transient of half a period in the free sloshing case.

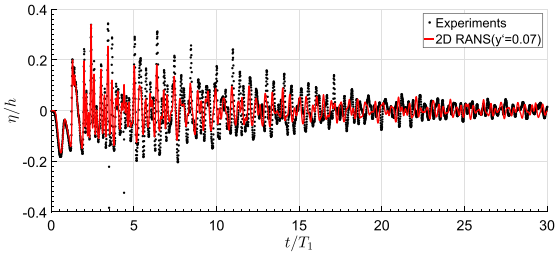

Fig. 7. Free sloshing results. Half a period of $f/f_{1,0} = 0.437$ at $h/L = 0.06$.

cycle with a frequency of $f/f_{1,0} = 0.437$. Time history of the motion amplitude is shown in Fig. 6. The long tank is used to perform these tests (configuration 1). Repeatability of such tests are not so good due to the low damping. No steady state exists and the sloshing is highly transient. The more damping the better should the repeatability be, as the damping act as a constraint to the motion. However, this is only true if details in the flow are excluded, like the chaotic wave front.

The reason for running free sloshing tests, as mentioned in Armenio and Rocca (1996), is to evaluate the ability of the model to predict the wave speed and shape. Sloshing with zero tank excitation results in natural sloshing modes. Our aim is to compare the frequencies from simulations with those that are calculated, as well as performing a sensitivity analysis on the turbulence settings. This is relevant because it is found that two-equation RANS turbulence models over-predicts the eddy viscosity at the free surface. The resulting free-surface elevation is given in Fig. 7. Some slight discrepancy in the free-surface amplitude is found before $t/T_1 = 20$. In the beginning, after $t/T_1 = 4$, the decay predicted by RANS is greater. Some signal noise is present at around $t/T_1 = 4$.

The wave profile at different time instants is shown in Fig. 8. Fig. 8b shows the wave when the motion stops. The travelling wave is small, but has some steepness in the beginning of the travel towards the right wall. The returning wave system is shown in Fig. 8d. At this time instant, the first of the three waves is registered by the ultrasonic sensor, while the following waves are seen towards the right. The wave with the maximum amplitude, in Fig. 8f, results from interaction

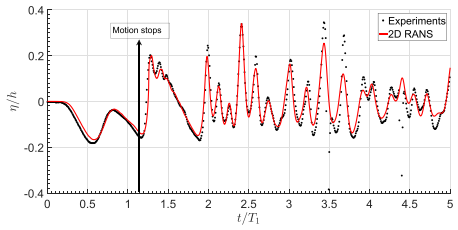

(a) Wave amplitude at motion stop.

(b) Simulated wave profile at motion stop.

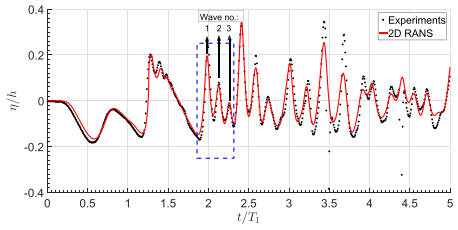

(c) Wave amplitude of 3 travelling waves.

(d) Wave profiles from simulations.

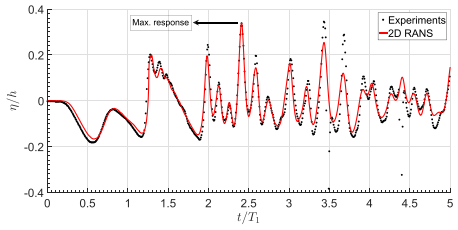

(e) Maximum wave amplitude.

(f) Wave profile at maximum response.

Fig. 8. Simulated wave profile at selected times. Sensor position is marked between the dark and light contours on the figure.

between the three waves (Fig. 8d) and occurs when the first of the three waves return to meet the two last waves.

Most of the simulations in this study are performed in two dimensions. To investigate the influence of wall shear on the damping, simulations in three dimensions are compared to the two-dimensional case. Fig. 9 shows a time series of 3D simulations performed at the Notur supercomputers. The grid cell number is equal to 1.6 million with the same Δx as in the 2D case. The difference between 2D and 3D is minor, which indicates that the damping due to wall shear is insignificant.

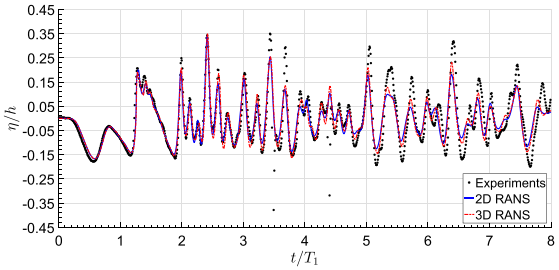

Fig. 9. Comparison of 2D and 3D running half a period before stop ($h/L = 0.06$ and $f/f_{1,0} = 0.437$).

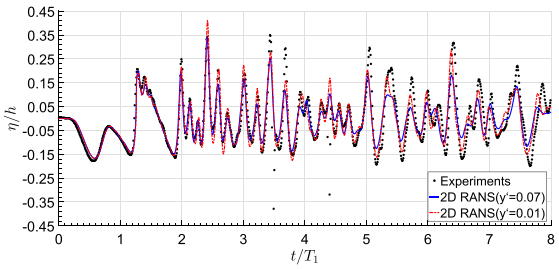

Fig. 10. Comparison of turbulence settings (Eq. (8)).

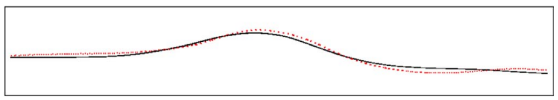

Fig. 11. Comparison of the wave profile for different turbulence settings. The red dotted line represent the lower value of y'. (The border does not represent the tank walls, and the free surface is blown up to see the differences).

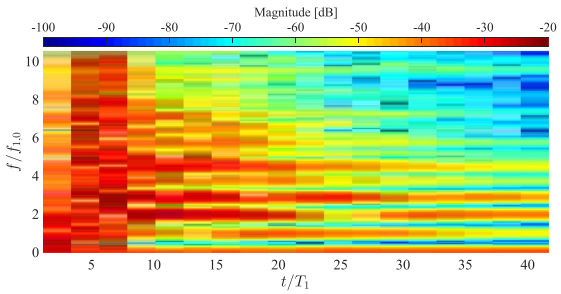

Fig. 14. Spectrogram representing experimental data. Running half a period before stop ($h/L = 0.06$ and $f/f_{1,0} = 0.437$).

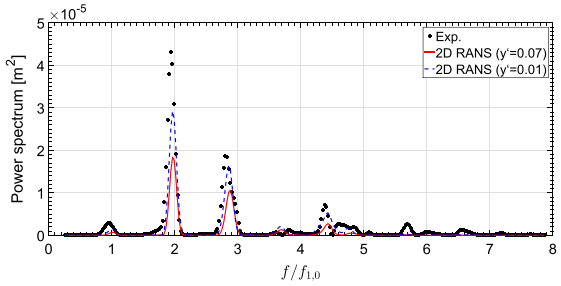

Fig. 15. FFT of the time window between $t/T_1 = 10$ and $t/T_1 = 20$. The largest peaks correspond to the natural frequencies, $f_{2,0}$ and $f_{3,0}$.

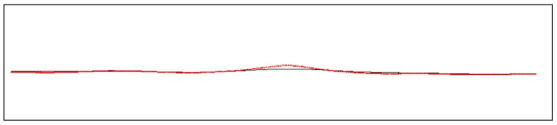

Fig. 16. Comparison of the wave profile for different turbulence settings. 2nd mode standing wave at $t/T_1 = 8.33$. The red dotted line represent the lower value of y'.

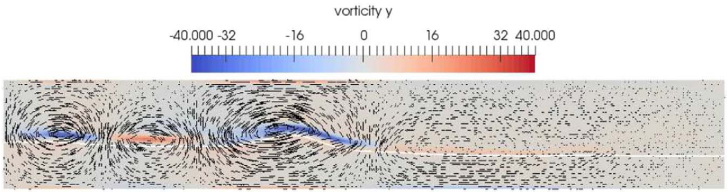

Fig. 12. Vorticity at the time of maximum response during the free sloshing test.

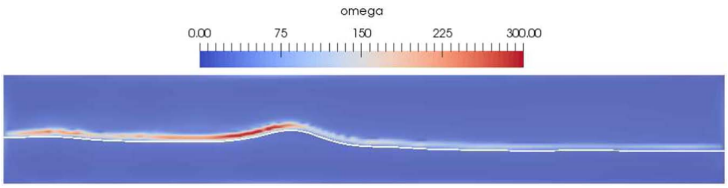

Fig. 13. Specific dissipation of turbulence energy (ω) at the time of maximum response during the free sloshing test.

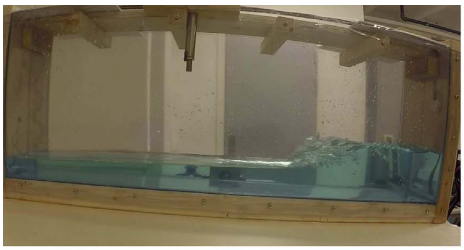

(a) Wave advancing upstream.

($h/L = 0.07$ and $f/f_{1,0} = 0.892$).

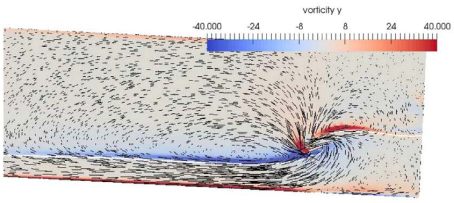

(b) Simulation of Fig. 17a.

($h/L = 0.07$ and $f/f_{1,0} = 0.892$).

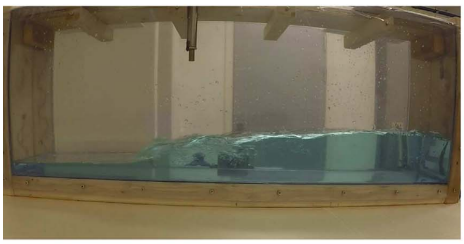

(c) Wave dissipating upstream.

($h/L = 0.07$ and $f/f_{1,0} = 0.892$).

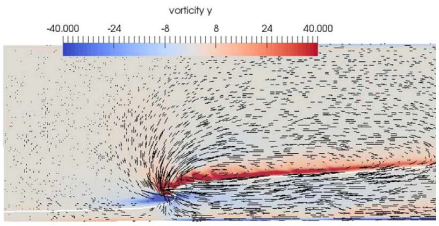

(d) Simulation of Fig. 17c.

($h/L = 0.07$ and $f/f_{1,0} = 0.892$).

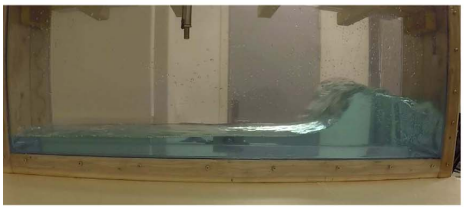

(e) Wave advancing downstream.

($h/L = 0.07$ and $f/f_{1,0} = 1.135$).

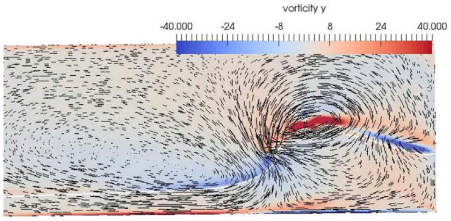

(f) Simulation of Fig. 17e.

($h/L = 0.07$ and $f/f_{1,0} = 1.135$).

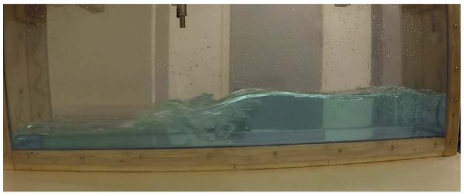

(g) Wave dissipating downstream.

($h/L = 0.07$ and $f/f_{1,0} = 1.135$).

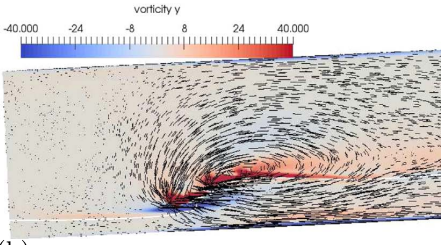

(h) Simulation of Fig. 17g.

($h/L = 0.07$ and $f/f_{1,0} = 1.135$).

Fig. 17. Upstream and downstream positive surge.

Fig. 18. Bounce back after impacting the surface. $h/L = 0.08$ and $f/f_{1,0} = 1.065$.

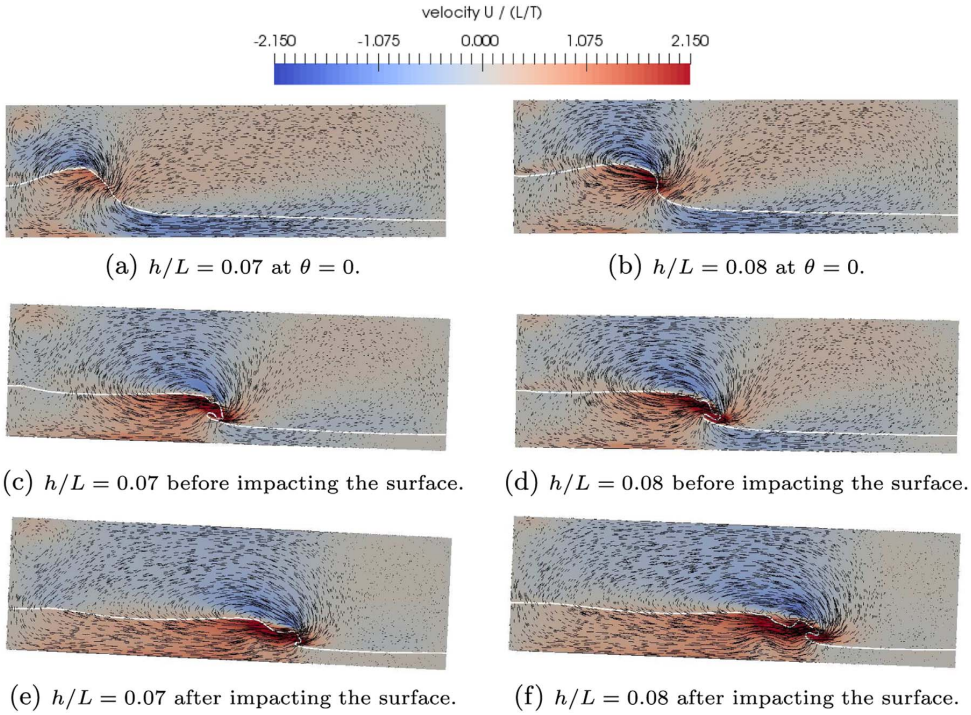

Fig. 19. Wave breaking with different mean depths. $h/L = 0.07$ / $f/f_{1,0} = 1.135$ and $h/L = 0.08$ / $f/f_{1,0} = 1.065$.

The free-surface boundary condition of ω can be investigated by adjusting the y' value in Eq. (8). The default value in REEF3D is 0.07. A reduction of this value increases the specific turbulent dissipation resulting in a decrease of the eddy viscosity. This is only activated at the free surface. From Fig. 10 the results clearly show that the lower value of y' results in increased amplitude. The wave amplitude is sensitive to the turbulence settings at the free surface. This is questionable because the fluid motion is expected to be laminar due to the low initial motion.

The free-surface profile at the time the maximum wave is measured is shown comparing the two turbulence settings in Fig. 11. The reduced eddy viscosity increases the crest and reduces the trough. The difference in the wave amplitude measured at this time instant is found to be approximately 0.3 [mm], so the difference is minor.

The vorticity at the same instant of time is plotted in Fig. 12. It indicates that viscous effects are important, and fluid properties are set into rotation by an unbalanced shear stress (Panton, 2004). Providing the vorticity offers a method to separate the flow into viscous and inviscid effects. Specific dissipation of turbulent energy is shown in Fig. 13. The dissipation dominates closest to the interface. The results are kind of paradoxical. When the dissipation is expected to be minor, the turbulence settings at the free surface will matter. But when the dissipation is large, like in forced sloshing close to resonance, these settings is of minor importance. It is a result from the abrupt change in fluid properties across the interface. The results does not have any particular consequence. The difference is seen only in the laminar case when the damping is small in general. That is why the results show some sensitivity.

The spectrogram plot in Fig. 14 shows short-time Fourier transformation (SFFT) of the experimental data. Fast Fourier transformation is performed in specified sections, or time windows. The signal is divided into 18 equal sections. This corresponds to a time interval of 6 [s] which equals the initial motion period. It can be seen that no distinct frequency dominates before approximately $t/T_1 = 8$. Here, the first symmetric mode is seen, $f/f_{1,0} \approx 2$ as well as the second asymmetric mode, $f/f_{1,0} \approx 3$. An FFT-analysis is performed between $t/T_1 = 10$ and $t/T_1 = 20$ including experiments and simulation results with the two

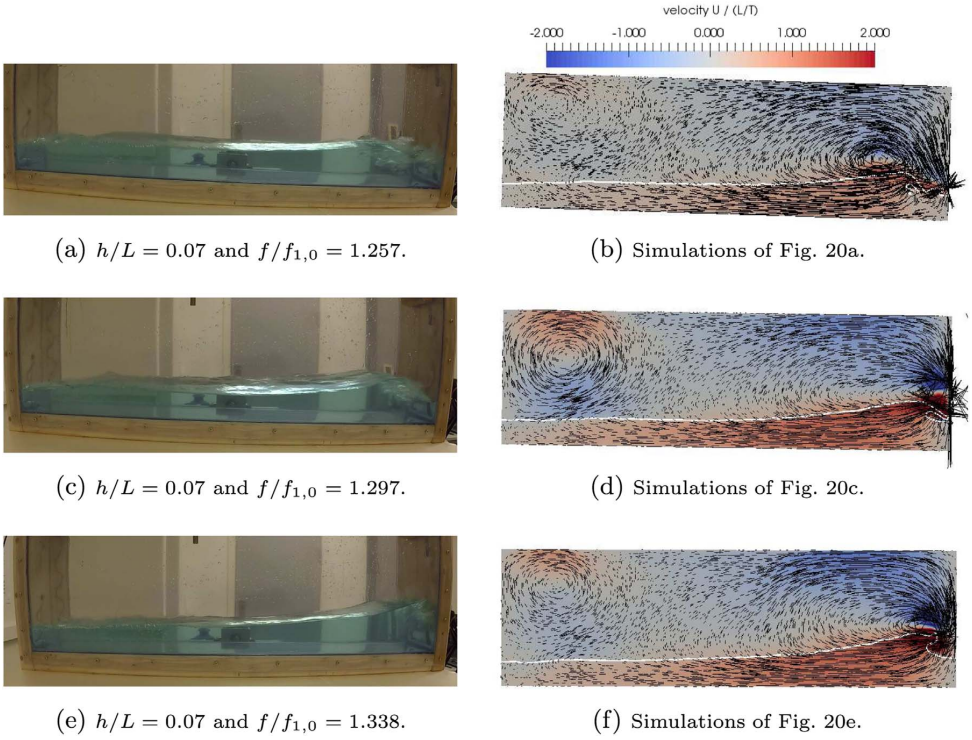

(a) $h/L = 0.07$ and $f/f_{1,0} = 1.257$. (b) Simulations of Fig. 20a.

(c) $h/L = 0.07$ and $f/f_{1,0} = 1.297$. (d) Simulations of Fig. 20c.

(e) $h/L = 0.07$ and $f/f_{1,0} = 1.338$. (f) Simulations of Fig. 20e.

Fig. 20. Frequencies slightly below and at the bifurcation point.

different values of y' (Fig. 15). The lower spectral value shows the underestimated wave amplitude from simulations. It is also seen that the lower value of y' is closer to the experiments. It is interesting to observe that although the natural frequencies are predicted quite well by the simulations, there is an increasing shift. This is not visible at $f/f_{1,0} = 2$, but more pronounced at $f/f_{1,0} = 3$ (Fig. 16).

Not only the amplitude is affected by the damping, but the wave speed as well.

4.4. Up- and downstream advancing waves

The chosen excitation frequencies are in proximity to the first fundamental frequency or higher. The results suggest that the characteristic patterns described by Olsen and Johnsen (1975) require further investigation. The difference seems to depend on the platform angle, which is particularly important for roll motion, as well as the tank filling. Observation reveals that the wave behaves quite differently depending on whether it is advancing up- or downstream. This is illustrated below in Fig. 17a–b. In the case of an upstream advancing wave, the breaking of the wave occurs almost immediately after returning from the side wall. While in the downstream case, the resulting wave has larger amplitudes before it eventually breaks as seen from Fig. 17e and g. If the angle of the tank is closer to zero when the wave returns, the wave gains more momentum due to gravitational forces travelling downstream after leaving the wall. As can be seen in Fig. 17b, the velocity of the lower liquid layer travels in an opposite direction to the wave. The wave may be characterized as a bore (Peregrine and Svendsen, 1978), and dissipates by travelling on top of the lower layer of liquid. Observation indicates that the largest difference between the two regimes depends on whether the wave breaks at a positive or negative tank motion angle. In this case, positive is defined for when the wave is advancing downstream. The wave in Fig. 17e–h is more of a spilling breaker type, and no plunging breakers are observed in the experiments. The impact force from the bore depends on how much the wave is dissipated before it reaches the wall.

4.5. Breaking characteristics of waves advancing downstream

In the previous section, different wave characteristics have been observed. The most significant impact occurs when a solitary wave travels along the whole tank length without breaking. All of the dissipation takes place in a very short time interval when it hits the wall. It is reasonable to assume that the impact force depends on the location of the breaking. If the wave breaks further away from the wall, more kinetic energy has been dissipated before it hits the wall. During the experiments, it is observed that even waves that break close to the middle can have significant kinetic energy when reaching the wall, and the energy increases with increasing liquid depth.

Fig. 19a and b show the waves when the tank is horizontal. Two different fillings are investigated. The same excitation frequency is used, which is $f = 0.4667[Hz]$. It can be seen that for $h/L = 0.08$, the wave is already overturning. The resulting difference is that the wave front drops with larger vertical velocity towards the liquid surface compared to $h/L = 0.07$. With $h/L = 0.07$ the gravitational component is larger in the longitudinal tank direction. The impact on the surface creates a bounce back and the motion is violent as shown in Fig. 18. Fig. 19f and g show the simulations at the time instants just after the impact.

4.6. Wave impacts close to the bifurcation point

A slight variation of the frequency below the observed bifurcation point shows different characteristics of the wave front just before impacting the wall. Fig. 20a–f shows video captures and corresponding simulations of the wave just before it hits the wall. The frequencies are at the bifurcation point in Fig. 20e and slightly below in Fig. 20a and c. In the case with the lowest frequency the wave breaks before the wall, but does not have time to dissipate before it impacts the wall. In Fig. 20c, the wave also starts to break, but even closer to the wall. This causes a more severe impact. At the bifurcation point, the wave does not break before it hits the wall.

From the figures, it can be observed that the platform angle is close to zero just before the wave hits the wall in Fig. 20e. The speed of the wave and momentum of the lower layer of liquid is balanced correctly with the platform angle to make the wave travel all of the tank length.

5. Conclusion

Sloshing at shallow depths results in steep waves that may potentially cause damages to structures due to severe impact at the walls. Understanding the wave patterns for a range of fillings and frequencies is important to remedy this.

Studies of sloshing in a rectangular tank with shallow depths were conducted at the lab facility at NTNU in Ålesund. A range of fillings between $h/L = 0.03$ to $h/L = 0.125$ were tested with several frequencies in proximity to the first mode natural frequency and ranging past the bifurcation point. RANS simulations of sloshing have been performed using the open-source finite difference CFD solver REEF3D. Comparisons are made between experiments and RANS for a selection of fillings and frequencies. Through the coherent approach of combining experiments and validated numerical simulations, the study extends the state-of-the art research through the description of additional wave pattern characteristics. The following conclusions can be made:

- The mean wave amplitude is measured for a range of fillings and frequencies. The wave breaks closer to the middle of the tank for the larger fillings. The resonance zone moves to higher frequencies for the lower depths.
- The bifurcation point is determined for a range of fillings between $h/L = 0.03$ and $h/L = 0.125$. It occurs at $f/f_{1,0}$ larger than unity for the lower fillings, while it approaches unity for fillings above $h/L = 0.1$.
- The theory from Verhagen and Van Wijngaarden (Verhagen and Wijngaarden, 1965) predicts a too high upper limit for hydraulic jumps to occur. Thus, it provides poor guidance for when the harmful wave impact occurs in the upper frequency range.
- The open-source CFD tool REEF3D predicts the sloshing waves with good accuracy. The largest deviation occurs when there are many waves present in the tank with severe oscillations, like above the bifurcation point and with free sloshing.
- Comparison of the free-surface elevation with free sloshing indicates that the damping of the wave is sensitive to the turbulence model settings at the free surface and less sensitive to the wall shear.
- The wave characteristics and dissipation mechanisms depend on whether the waves advance up- or downstream in the tank. This is relevant for sloshing under a roll motion.

Acknowledgement

The authors would like to thank the staff at the Department of Maritime Technology and Operations for providing lab facilities and materials necessary for performing the experiments. Thanks also to the other members of the REEF3D team for their support. This study is a part of a PhD project funded by NTNU in Ålesund.

Appendix A. Appendix

An example of input files for REEF3D is given below. The first text file, 'control.txt' sets the meshing and boundary conditions. The second file, 'ctrl.txt' is to set the simulation parameters. Explanation to the relevant settings is given behind each line starting with '//'. The reader is also referred to the REEF3D manual (Bihs and REEF3D, 2016).

'control.txt':

```
C 11 21 //Wall boundary
C 12 3 //Symmetry boundary
C 13 3
C 14 21
C 15 21
C 16 21
B 1 0.003 //Grid cell size [m]
B 10 0.0 1.0 0.0 0.003 0.0 0.3 //B 10 Provide the size of domain in x-, y and
z-dir. [m]
M 10 4 //No. of processors for parallel computations
```

'ctrl.txt':

B 5 1

B 10 1

B 11 1

B 50 0.0001 //Surface roughness

B 192 -3.0 0.16667 0.5 0.0 //B192 provide angle amplitude [deg], frequency [Hz]
and point of rotation (x,y) [m]

B 194 0.0 3.0 //Time to start and stop motion [s]

D 10 4

D 20 2

D 30 1

F 30 3

F 40 3

F 46 2

F 50 4

F 60 0.06 //Free surface position

I 12 1

N 40 3

N 41 100.0 //Total simulation time

N 47 0.1

M 10 4 //No. of processors, here 4

P 10 1

P 30 0.05 //Time of printing VTU-files [s]

P 40 1

P 41 1

P 54 10

P 51 0.408 0.125 //Position of wave sensor

P 51 0.1 0.125 //Position of sensor no. 2

P 51 0.5 0.125 //Position of sensor no. 3

P 75 1

P 101 1

T 10 2

T 36 1 //Free-surface turbulence limitation ON

T 37 0.01 //y'-value of free-surface turbulence BC

W 22 -9.81

References

Afzal, M.S., Bihs, H., Kamath, A., Arntsen, Ø.A., 2015. Three-dimensional numerical modeling of pier scour under current and waves using level-set method. J. Offshore Mech. Arct. Eng. 137 (3), 032001.

Ansari, M., Firouz-Abadi, R., Ghasemi, M., 2011. Two phase modal analysis of nonlinear sloshing in a rectangular container. Ocean Eng. 38 (11), 1277–1282.

Armenio, V., Rocca, M.La, 1996. On the analysis of sloshing of water in rectangular containers: numerical study and experimental validation. Ocean Eng. 23 (8), 705–739.

Bai, W., Liu, X., Koh, C., 2015. Numerical study of violent lng sloshing induced by realistic ship motions using level set method. Ocean Eng. 97, 100–113.

Berthelsen, P.A., Faltinsen, O.M., 2008. A local directional ghost cell approach for incompressible viscous flow problems with irregular boundaries. J. Comput. Phys. 227 (9), 4354–4397.

Bihs, H., Kamath, A., Chella, M.A., Aggarwal, A., Arntsen, Ø.A., 2016. A new level set numerical wave tank with improved density interpolation for complex wave hydrodynamics. Comput. Fluids 140, 191–208.

Bihs, H., 2016. REEF3D, User Guide. ⟨https://reef3d.files.wordpress.com/2012/05/reef3d-userguide_16-11.pdf⟩.

Bouscasse, B., Antuono, M., Colagrossi, A., Lugni, C., 2013. Numerical and experimental investigation of nonlinear shallow water sloshing. Int. J. Nonlinear Sci. Numer. Simul. 14 (2), 123–138.

Bulian, G., Souto Iglesias, A., Delorme, L., Botia Vera, E., 2010. Smoothed particle hydrodynamics (SPH) simulation of a tuned liquid damper (TLD) with angular motion. J. Hydraul. Res. 48 (Spécia), 28–39.

Center for Applied Scientific Computing. Hyper High Performance Preconditioners - Users Manual, 2015.

Chella, M.A., Bihs, H., Myrhaug, D., Muskulus, M., 2015. Breaking characteristics and geometric properties of spilling breakers over slopes. Coast. Eng. 95, 4–19.

Chorin, A.J., 1968. Numerical solution of the Navier-Stokes equations. Math. Comput. 22 (104), 745–762.

Delorme, L., Colagrossi, A., Souto-Iglesias, A., Zamora-Rodriguez, R., Botia-Vera, E., 2009. A set of canonical problems in sloshing, part i: pressure field in forced rollcomparison between experimental results and SPH. Ocean Eng. 36 (2), 168–178.

Durbin, P.A., 2009. Limiters and wall treatments in applied turbulence modeling. Fluid Dyn. Res. 41 (1), 012203, ⟨http://stacks.iop.org/1873-7005/41/i=1/a=012203⟩.

Faltinsen, O.M., Timokha, A.N., 2009. Sloshing. Cambridge University Press.

Gómez-Goñi, J., Garrido-Mendoza, C.A., Cercós, J.L., González, L., 2013. Two phase analysis of sloshing in a rectangular container with volume of fluid (VOF) methods. Ocean Eng. 73, 208–212.

Hossain, M., Rodi, W., 1980. Mathematical modelling of vertical mixing in stratified channel flow. In: Proceedings of the 2nd Symposium on Stratified Flows, pp. 280–290.

Ibrahim, R.A., 2005. Liquid Sloshing Dynamics: Theory and Applications. Cambridge University Press.

Iglesias, A.S., Rojas, L.P., Rodríguez, R.Z., 2004. Simulation of anti-roll tanks and sloshing type problems with smoothed particle hydrodynamics. Ocean Eng. 31 (8), 1169–1192.

Jiang, G., Shu, C., 1996. Efficient implementation of weighted ENO schemes. J. Comput. Phys. 126 (130), 202–228.

Kamath, A., Bihs, H., Arntsen, Ø.A., 2015. Numerical investigations of the hydrodynamics of an oscillating water column device. Ocean Eng. 102, 40–50.

La Rocca, M., Sciortino, G., Boniforti, M.A., 2000. A fully nonlinear model for sloshing in a rotating container. Fluid Dyn. Res. 27 (1), 23.

La Rocca, M., Sciortino, G., Adduce, C., Boniforti, M., 2005. Experimental and theoretical investigation on the sloshing of a two-liquid system with free surface. Phys. Fluids (1994-Present) 17 (6), 062101.

Liu, D., Lin, P., 2008. A numerical study of three-dimensional liquid sloshing in tanks. J. Comput. Phys. 227 (8), 3921–3939.

Mele, P., Armenio, V., 1997. Variational approach to the problem of sloshing in a moving container. J. Theor. Appl. Fluid Mech. 1, 280–310.

Menter, F.R., 1994. Two-equation eddy-viscosity turbulence models for engineering applications. AIAA J. 32 (8), 1598–1605.

Naot, D., Rodi, W., 1982. Calculation of secondary currents in channel flow. J. Hydraul. Div. 108 (8), 948–968.

Nourgaliev, R., Wiri, S., Dinh, N., Theofanous, T., 2005. On improving mass conservation of level set by reducing spatial discretization errors. Int. J. Multiph. Flow 31 (12), 1329–1336.

Olsen, H.A., Johnsen, K., Nonlinear sloshing in rectangular tanks. In: A Pilot Study on the Applicability of Analytical Models.

Osher, S., Sethian, J.A., 1988. Fronts propagating with curvature-dependent speed: algorithms based on hamilton-jacobi formulations. J. Comput. Phys. 79 (1), 12–49.

Panton, R.L., 2004. Incompressible Flow. John Wiley & Sons Inc, New Jersey.

Peng, D., Merriman, B., Osher, S., Zhao, H., Kang, M., PDE-based, A., 1999. fast local level set method. J. Comput. Phys. 155 (2), 410–438.

Peregrine, D., Svendsen, I., Spilling breakers, bores, and hydraulic jumps. Coastal Engineering Proceedings 1, (16).

Rocca, M.L., Sciortino, G., Boniforti, M.A., 2002. Interfacial gravity waves in a two-fluid system. Fluid Dyn. Res. 30 (1), 31, ⟨http://stacks.iop.org/1873-7005/30/i=1/a=A04⟩.

Schlichting, H., 1979. Boundary-Layer Theory. McGraw-Hill Book Company.

Sussman, M., Smereka, P., Osher, S., 1994. A level set approach for computing solutions to incompressible two-phase flow. J. Comput. Phys. 114 (1), 146–159.

Sussman, M., Fatemi, E., Smereka, P., Osher, S., 1998. An improved level set method for incompressible two-phase flows. Comput. Fluids 27 (5), 663–680.

Verhagen, J., Van Wijngaarden, L., 1965. Non-linear oscillations of fluid in a container. J. Fluid Mech. 22 (04), 737–751.

Wilcox, D.C., 1988. Reassessment of the scale-determining equation for advanced turbulence models. AIAA J. 26 (11), 1299–1310.

Wilcox, D., 1994. Turbulence Modeling for CFD, DCW Industries, Incorporated, ⟨https://books.google.com/books?Id=VwlRAAAAMAAJ⟩.

Zhao, Y., Chen, H.-C., 2015. Numerical simulation of 3D sloshing flow in partially filled lng tank using a coupled level-set and volume-of-fluid method. Ocean Eng. 104, 10–30.

Paper V

Paper 5 - Experimental and Numerical Investigation of Sloshing in Marine LNG Fuel Tanks.

Grotle, Erlend Liavåg; Æsøy, Vilmar. (2017)
ASME 2017 36th International Conference on Ocean, Offshore and Arctic Engineering, Volume 1: Offshore Technology.
doi:10.1115/OMAE2017-61554.

Is not included due to copyright

Paper VI

Paper 6 - Dynamic modelling of the thermal response enhanced by sloshing in marine LNG fuel tanks.

Grotle, Erlend Liavåg; Æsøy, Vilmar. (2017)
Revised manuscript submitted to Applied Thermal Engineering.

Dynamic modelling of the thermal response enhanced by sloshing in marine LNG fuel tanks

Erlend Liavåg Grotle[a,*], Vilmar Æsøy[a]

[a] *Department of Ocean Operations and Civil Engineering, Norwegian University of Science and Technology (NTNU), NO-6009 Ålesund, Norway*

Abstract

This paper investigates the thermal response in marine liquefied natural gas (LNG) fuel tanks by experiments and modelling. The aim of this work is to develop phenomenological models that can predict the rapid pressure loss experienced onboard LNG fuelled vessels. Experiments have been conducted using water. A horizontally aligned tank made of steel has the same geometry as a LNG fuel tank, but at model scale. The tests are performed by supplying heat to evaporate water that is led through a closed loop from the bottom to the top passing a heating element. A lumped dynamic model is developed that can be tuned by adjusting few parameters. Uniform conditions are assumed in each phase. The model can provide useful insight and be combined with other submodels to perform system simulations. Good correspondence with the experimental data is found after tuning heat transfer coefficients, air content in the gas and the average temperatures. After validating the model, it is used to predict the necessary heat supplied to the pressure build-up unit (PBU) to maintain the tank pressure. A simple relation between the measured pressure and the PBU heat capacity is presented.

Keywords: Sloshing, dynamic models, experiments, heat transfer, LNG fuel tanks

1. Introduction

Natural gas as a fuel has proven beneficial for the environment [1]. The number of ships fuelled with liquefied natural gas (LNG) has increased the recent years, and operational experience has shown that ensuring reliable operation is still challenging. One of the challenges are related to the thermodynamic response inside the LNG fuel tank, influenced by sloshing. Sloshing can be characterized as the motion of liquids in containers or vessels [2]. Traditionally, concerns with sloshing are damages due to impact forces. Sloshing may also alter the ship stability, but is also used to enhance the ship stability with roll-stabilizer tanks. The rapid pressure drop in the LNG fuel tanks is related to the motion, filling depth and the temperature of the bunkered LNG. The consequence of such a pressure drop is shutdown of the gas engines, as the system pressure may drop below a minimum required for reliable operation [3]. The potential pressure

*Corresponding author
Email address: erlend.l.grotle@ntnu.no (Erlend Liavåg Grotle)

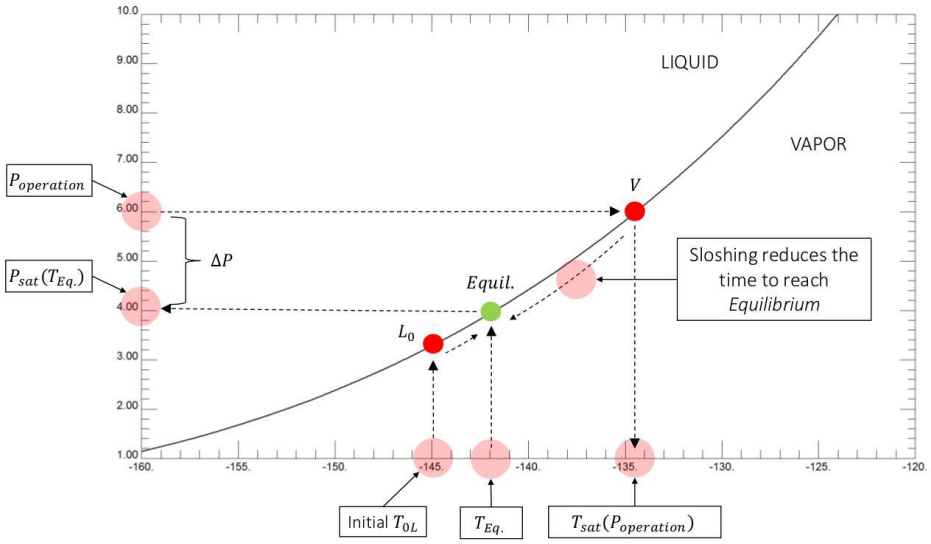

Figure 1: Co-existence curve for methane. The P-T data was generated using REFPROP v9.1 [4].

drop in a tank with a single component fluid can be explained by considering the co-existence curve for methane (Fig. 1).

The potential pressure drop corresponds to the maximum possible temperature difference between the liquid bulk and the saturation temperature of the operational pressure. The operating pressure corresponds to a T_{sat}, which is higher than the bunkered liquid temperature. If it is assumed that the liquid temperature remains the same, the potential final pressure corresponds to this temperature. The liquid temperature is also increasing, depending on its mass. The superheated gas counteracts the subcooled liquid, but the larger liquid mass makes it dominating the process.

Moran *et al.* [5] investigated the thermodynamic response due to sloshing in a liquid hydrogen tank by performing experiments with varying excitation frequency. The pressure collapse magnitude was recorded, as well as the temperature at different locations. Unstable sloshing conditions with an excitation close to the first mode natural frequency was found to have the greatest impact on the pressure drop, while stable sloshing were found to have minor effect.

Lacapere *et al.* [6] compared experimental tests and numerical simulations to investigate the influence of interface heat and mass transfer on the pressure evolution due to sloshing using both liquefied nitrogen (LN_2) and liquefied oxygen (LOx). Comparison between the numerical simulations and experiments shows that the de-stratification in the liquid is responsible for the large pressure drop.

Arndt [7] presented experiments in his PhD thesis, and found that the presence of non-condensible gas reduces the condensation and increases the evaporation. This indicates that condensation is responsible for

the majority of the energy transfer.

Ludwig *et al.* [8] conducted several experiments using liquefied nitrogen (LN_2) in a vacuum-insulated upright cylindrical tank. All of the experiments were conducted with one translational motion amplitude, except in the last case. The excitation frequency was varied in proximity to the first mode natural frequency, representing regimes that cover the range of stable planar wave motion to swirl waves. A Nusselt number were introduced that correlates with a sloshing Reynolds number based on wave amplitude and frequency.

Sloshing in a horizontally aligned pressure vessel were investigated by Grotle et al. [9] using LN_2 as test medium. The influence of frequency and initial pressure is presented in the paper. It was found that the pressure drop rate depends on the frequency, and the most significant occurs close to the first mode natural frequency. The total pressure drop is influenced by the initial pressure, but to reach the potentially minimum, a certain sloshing intensity is required.

From the mentioned studies there are strong evidence that direct energy exchange takes place between the liquid and the gas. This is also the hypothesis in this project. Direct-contact heat transfer can be beneficial with the large contact area between the phases, and the thermal resistance of a solid wall is also excluded [10]. There are several industrial processes where direct-contact heat transfer are applied. One example is fluid mixing by an axial jet which is a method to reduce tank pressure of a two-phase system in which the fluid is thermally stratified. This is done to prevent pressure rise due to external heating in a cryogenic tank [11], [12]. Mahood *et al.* [13] made a theoretical prediction of the transient characteristics of a two-phase, two-component direct-contact condenser. Joseph *et al.* [14] studied the effect of insulation thickness on the pressure evolution in a cryogenic tank. The tank model is divided into an ullage gas volume and a liquid volume. The pressurization is investigated using the ideal gas law with a compressibility factor. The same modelling principle is used in our model, assuming that the latent heat must balance the total sensible heat, and that the sensible heat consist mainly of convection.

Modelling of thermodynamic systems by the bond graph technique is inspired by Karnopp [15], Moksnes [16], Pedersen [17]. and Thoma [18].

2. Objectives

A lumped dynamic model may be useful when several subsystems are joined together to perform system simulations, because the models are computational efficient. In the case of LNG fuelled ships, the fuel system itself consist of several units, including the tank, pressure build-up unit (PBU), main evaporator, gas recovery unit (GRU) and the gas engines with propulsion- and control system. Although our modelling approach is fairly simple, it can provide useful insight by combining it with experimental results.

In this paper, a two-compartment dynamic model is developed to represent the thermal response due to sloshing. The main focus is the mechanisms that cause the rapid pressure loss experienced on-board LNG

fuelled ships. Experiments have been conducted with a model scaled LNG fuel tank. Liquid water and vapour is used as test medium. A discussion about the similarity between methane and water is presented in the last part. To study the sloshing regimes, tests with a transparent tank of similar size are presented as well. The thermodynamic model is developed using the bond graph technique, which is a graphical method to combine several ordinary differential equations to a system of equations that can be solved numerically. The aim is to tune the model according to experiments with only a limited number of parameters. Only a few tests are presented here, but they represent different sloshing regimes. This is done on purpose to better emphasize the effect of sloshing on the pressure drop.

As to our knowledge, there are no similar studies presented with such a modelling technique to represent direct-contact heat- and mass transfer enhanced by sloshing. No similar tests involving the thermal response in a horizontally aligned pressure vessel can be found as far as to the authors knowledge. Few general sloshing studies considering semi-elliptic pressure vessels exist, and so the preliminary investigation of the transparent tank is a contribution as well.

The results show that our dynamic model represent the thermodynamic response quite accurately by tuning few parameters. The greatest uncertainty in the model is the spatial distribution of internal energy. It is found that the assumption of convection in the bulk as the driving mechanisms for condensation is too rough. The relation between the condensation mass flow and the bulk convection is too tightly coupled considering uniform conditions in each phase. This is because we can not separate the area from the heat transfer coefficients, and with lack of a proper formulation of the condensation mass flow rate. A simple way to predict the PBU power need from the measured pressure is presented in the last part of the paper.

3. Model description

3.1. Mass and energy balance

By considering the whole tank as a system, the total energy balance can be written as the sum of internal, kinetic and potential energy.

$$dU + dE_k + dE_p = \delta Q - \delta W, \tag{1}$$

where U is the total internal energy of the tank, E_k and E_p are kinetic and potential energy respectively. Q is heat and W is work transferred to the system. We consider only heat supply to the PBU (Fig. 2). The work term consist of pressure-volume work and external work. We assume that all the work input corresponds to the sum of the change in kinetic and potential energy. These terms then vanish. This is the same as assuming that there is no change in internal energy due to dissipation of kinetic energy.

The tank system is divided into two compartments that exchange internal energy, one for liquid and one for gas, as shown in Fig. 2. Heat is also transferred to the PBU. The energy balance for the total tank system

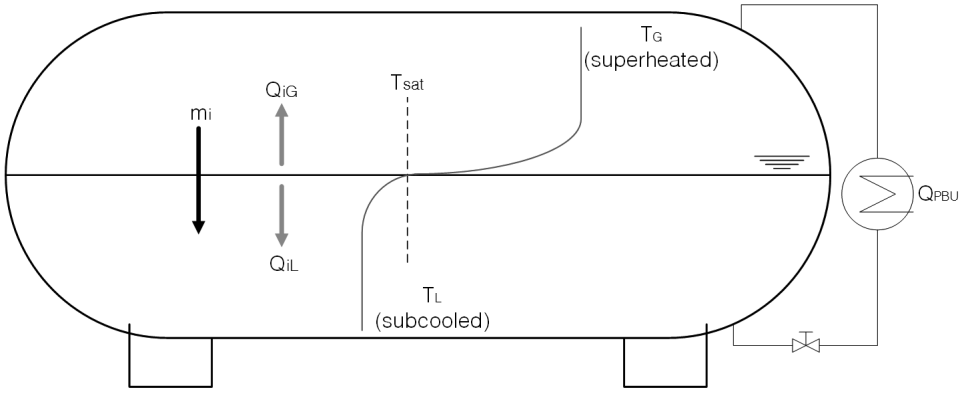

Figure 2: Model description.

then reads

$$dU_L + dU_G = \dot{Q}_{PBU}, \tag{2}$$

where the subscripts, L and G mean liquid and gas respectively. Our assumption of no heat losses is acceptable since the heat transfer between the phases is much greater during the period of sloshing. As explained in the previous sections, the purpose of the PBU in the fuel system is to maintain the tank pressure. The heating element is used in the experiments compensate the for the pressure during sloshing.

For the mass, we have the following condition

$$dm_L + dm_G = 0. \tag{3}$$

As the total tank volume is constant, the volume is also conserved, so that

$$dV_L + dV_G = 0. \tag{4}$$

The liquid density is kept constant in the model. This means that the gas density can be solved for when both the volume and mass in each phase are used as state variables.

In addition to this, we have the energy balance for each of the phases, where the internal energy is given as:

$$\frac{dU_G}{dt} = \dot{m}_G u_g + \dot{Q}_{iG} - p\frac{dV_G}{dt} + \dot{Q}_{PBU}, \tag{5}$$

$$\frac{dU_L}{dt} = \dot{m}_L u_f + \dot{Q}_{iL} - p\frac{dV_L}{dt}. \tag{6}$$

Here $\dot{Q}_{iG}$ and $\dot{Q}_{iL}$ are sensible heat fluxes in the gas- and liquid bulk. $\dot{m}_G$ is the evaporation mass flux equal to dm_G/dt. u_g and u_f are the specific saturation internal energy for gas and liquid respectively.

$\dot{Q}_{PBU}$ is the heat supplied to the heating element, and is defined as

$$\dot{Q}_{PBU} = \dot{m}_{PBU} \cdot \left[h_{fg} + c_{v,L} \left(T_{sat} - T_L \right) \right], \tag{7}$$

where h_{fg} is the specific enthalpy of formation and $c_{v,L}$ is the specific heat capacity of the liquid.

Summing Eq. 5 and Eq. 6 and subtracting the result from Eq. 2 it can be shown that

$$u_{fg}\dot{m}_L = \dot{Q}_{iG} + \dot{Q}_{iL}. \tag{8}$$

This is the interface condition which shows that the sensible heat is balanced by latent heat. If there is no mass exchange, the heat flux must be the same on each side of the interface. Positive heat flux is defined as positive into a control volume. By considering that the heat flux is always directed towards decreasing temperature, the value of the gas side sensible heat would be negative, while the liquid side positive (see Fig. 2). $\dot{m}_L$ is the condensation mass flux. Increasing the superheated gas temperature would then reduce $\dot{m}_L$, while reducing liquid temperature would increase $\dot{m}_L$.

The specific internal energy is $u = U/m$ and a simple relation between the specific internal energy and temperature is used,

$$u_G - u_g = c_{v,G} \left(T_G - T_{sat} \right), \tag{9}$$

$$u_L - u_f = c_{v,L} \left(T_L - T_{sat} \right). \tag{10}$$

$T_{sat} = T(P_v)$ is the saturation temperature which is assumed to be the temperature at the interface, and a function of the vapour pressure, P_v.

The assumption of uniform conditions means that a mass-averaged temperature must be considered to ensure that the energy balance is fulfilled. This may easily result in errors as the spatial distribution is not entirely known from the experiments. As far as possible, the experimental measurements are used to find a mass-averaged value. In some of the cases, the information is still not enough to know how the temperature is distributed spatially. In this work we approximate the values by weighting the energy content by a factor. This is adjusted until the energy balance is fulfilled. This must be done after the other parameters are determined as will be explained in the following. The resulting average temperature are then compared to the measured values. Working with averaged values like this is probably the largest uncertainty of our model.

The sensible heat on each side of the interface, $\dot{Q}_{iG}$ and $\dot{Q}_{iL}$ can be defined according to Newtons law of cooling

$$\dot{Q}_{iG} = -h_{iG} \cdot A_i \left(T_G - T_{sat} \right), \tag{11}$$

$$\dot{Q}_{iL} = -h_{iL} \cdot A_i \left(T_L - T_{sat}\right). \tag{12}$$

h_{iG} and h_{iL} are the heat transfer coefficients for the gas and liquid side of the interface respectively. A_i is the interface area. Each of them can not be known by tuning the model, but the product. $h_i \cdot A_i$ can be found by comparing the simulated temperature and pressure with the experimental results. The tuning of these parameters only changes the speed, not the final state.

The liquid temperature has significant influence on the pressure due to the large mass. The gas side heat transfer coefficient has only a minor impact on the pressure, but influences the proximity of the gas temperature to the saturation temperature. The experimental saturation temperature is found from the pressure. The low influence of the gas side heat transfer coefficient on the pressure makes it possible to assume saturation conditions in the gas without changing the final state much. This is the same as assuming a very large heat transfer coefficient.

The pressure can be related to the gas temperature and density by the ideal gas law,

$$P = \rho_G R T_G, \tag{13}$$

where R is the individual gas constant, equal to R_u/M and R_u is the universal gas constant, ρ_G is the gas density and M the mole weight.

Air is present in the gas pocket during the tests and its contribution to pressure must be accounted for. The mass of dry air is unknown, but can be found by assuming that the saturation temperature must correspond to the equilibrium temperature of liquid and gas. The saturation temperature is a function of the vapour pressure. The change in the fluid properties, like the specific heat capacity is also taken into account.

The concept of specific humidity can be used [19]. Introducing the ideal gas law, we got:

$$\omega = \frac{m_v}{m_a} = \frac{M_v P_v V / R_u T}{M_a P_a V / R_u T} = \frac{M_v P_v}{M_a P_a}, \tag{14}$$

where we have introduced the partial pressure of water vapour ("v") and air ("a"), as well as the respective mole masses, M_v and M_a, with the ratio approximately equal to $M_v/M_a = 0.622$. The total pressure, P consist of the sum of these partial pressures, such that

$$P_v = P \cdot \left(\frac{0.622}{\omega} + 1\right)^{-1}. \tag{15}$$

In this way, the correct saturation temperature can be found from the vapour partial pressure.

3.2. Implementation of the model using bond graphs

The bond graph method provides a simple graphical method to solve a set of ordinary differential equations. A lumped model is only varying in time, and the state variables are integrated numerically using

20-sim [20]. The resulting bond graph is shown in Fig. 3. Each C-element represent accumulation of mass and internal energy in each phase. The resultant flux (right-hand side of Eq. 5 and Eq. 6) is integrated to give the new effort variables. The two MSf-elements at the right are pressure-volume work, which is minor in this case. The R-element ("Ev") represent the sensible heat flux on each side of the interface. The sum is equal to the latent heat, and the mass flux is calculated inside the same R-element. The mass- and energy fluxes are calculated in the beginning of each time step based on the difference of the effort variables which in this case is the temperature. All the saturation properties are found by interpolation in thermodynamic tables. The PBU-power of the heating element is supplied with the Sf-element ("Heat"). The mass and energy flow through the heating element is calculated in side the R-element ("Element").

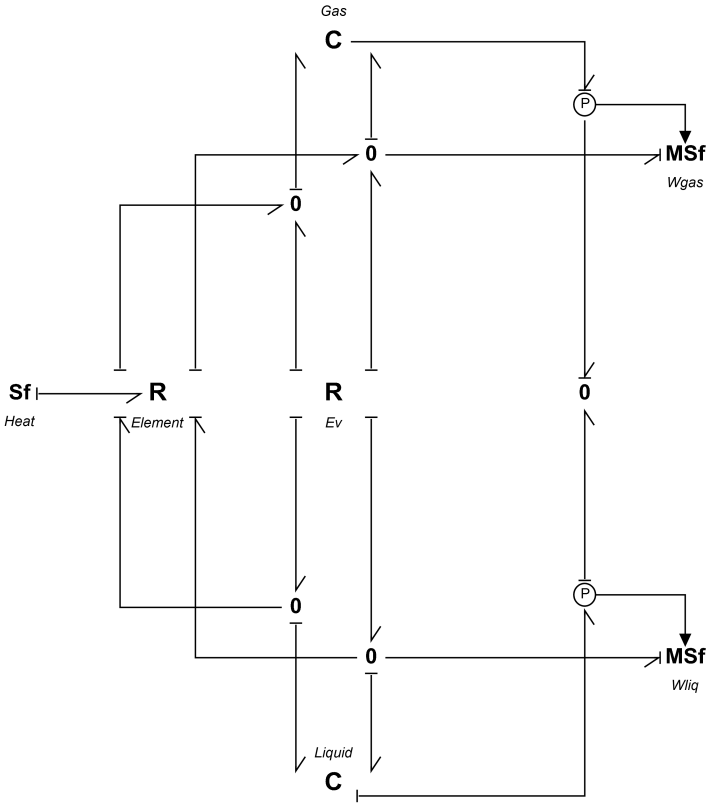

Figure 3: Bond graph model.

4. Experimental set-up

4.1. Thermal tank test

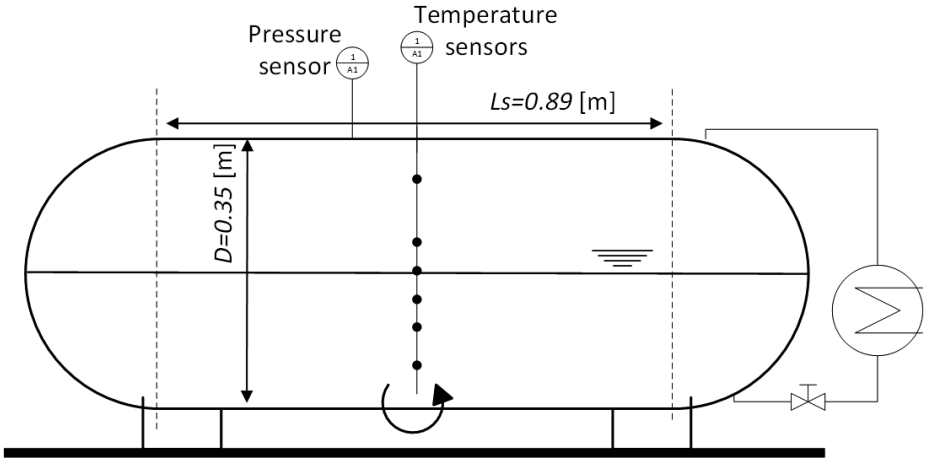

Figure 4: Thermal tank and the instrumentation.

Table 1: Specifications of instrumentation and devices.

Device	Type	Range	Accuracy
Temperature sensor	Thermocouple type T	-270-370 [°C]	±1.0 [°C]
Pressure sensor	P8AP	0-20 [bar]	0.3 %
Heating element	Høiax	0-1460 (max. 3000) [W]	-
Voltage supply	Philips 2422 530 05401	0-260 [V]	-
Electro-motor	MAC800-D2	750 [W] @ 3000 RPM	±0.5 % (speed)

The experimental work presented in this paper consists of tests performed with an insulated cylindrical pressure tank. The set-up is shown in Fig. 4. It consist of instrumentation like pressure sensor and several thermocouples placed vertically in the middle of the tank. The instruments and their specification are given in Table. 1. At the right side on Fig. 4, a variant of a unit PBU has been installed. A heating element is heated by using an external voltage supply. The mean water depth in the tank is 50 % in all tests. The heater is placed lower than the mean depth, and the flow of water and vapour is driven by hydrostatic pressure differences. The relationship between mass flux and power supply is measured in advance to know the amount of vapour.

The test procedure consist of initial heating of the liquid from approximately 15-20 degC to 120 degC. This ensures that the ΔT does not get too large. The heater is adjusted to the maximum power possible. For these tests, the power has been limited to 1460 [W]. In the beginning, the tank is left open to remove air. However, removing air from the system can be challenging, so it is expected that the presence of air must

Table 2: Sloshing test conditions. h/D is the mean height to diameter relationship, L_s $[m]$ is the length of the cylindrical section, f $[Hz]$ is the excitation frequency and $f/f_{1,0}$ is the frequency divided by the first mode natural frequency calculated for a rectangular tank with the same length as L_s. t_s $[s]$ is the length of the sloshing time.

Case No.	h/D	h/L_s	f $[Hz]$	$f/f_{1,0}$	t_s	Description
0	0.50	0.19	0.13	0.200	30	Flat surface
1	0.50	0.19	0.29	0.427	70	Small deformation
2	0.50	0.19	0.40	0.495	51	Oscillating waves
3	0.50	0.19	0.57	0.840	30	Jet formed

be accounted for. To build up the system temperature we switch between pressurisation with the heater and sloshing. The heat is then mixed more efficiently inside the tank.

When the system is ready for the sloshing tests, the pressure is increased to the desired value. The heater is turned off and the electro-motor starts with a specified frequency and number of periods.

4.2. Investigation of sloshing regimes

The thermal tank is not transparent. To study sloshing inside these tanks, a pre-study is also performed where a transparent tank of similar size and form is moved on a platform. Existing studies on horizontally aligned cylindrical tanks are limited, and the natural frequencies with these type of tank heads are unknown. Studies have been performed by the authors, but the results are not yet published.

A characteristic feature of the sloshing in these tanks is the jet that forms due to the spherical tank heads, as seen Fig. 5a. When the wave that builds up at the side wall hits the roof, the circular form lead the liquid in return with high speed. There is less impact against the roof compared to a square corner like in rectangular tanks. The jet goes approximately half way back in return before it hits the liquid surface with an inclined angle. The form and speed depends on filling and frequency. The frequency range is narrower for the lower fillings with a motion frequency closer to primary resonance. With fillings $h/D \geq 0.5$ like studied here, the jet is present in a broader frequency range.

The chosen sloshing parameters used in this preliminary study are given in Table 2. The same motion amplitude, filling and frequency were used to study the thermal response. The motion amplitude is kept constant and equal to 3 degrees in all tests. Several more experiments have been performed by the authors, but the listed conditions are chosen specifically to validate the dynamic model.

In case number 0 the frequency is very low. The free surface remains flat and the wetting of the walls is only due to the inclination angle. There is no break-up of the liquid-gas surface.

In the second case small waves are present, but the surface is not broken.

The third case is performed with a motion closer to the first mode natural frequency. Several waves are oscillating rapidly, like shown in Fig. 5b. The surface does not break, but steep standing waves sometimes result in some splashing.

Case 3 is at resonance so the sloshing is severe. The jet seen in Fig. 5a is present during the whole sloshing event.

(a) The jet formed due to the spherical heads (case number 3).

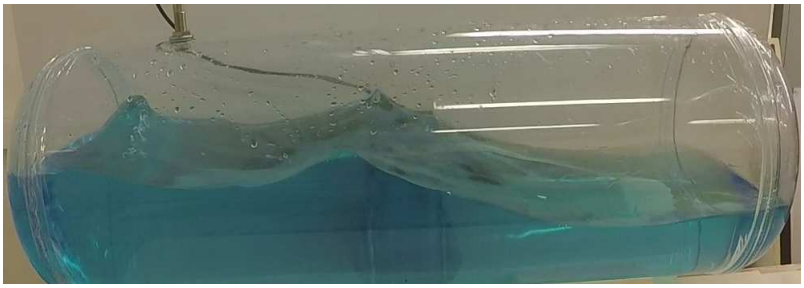

(b) Oscillating surface without breaking (case number 2).

Figure 5: Sloshing cases.

5. Results

5.1. Comparison of the pressure drop

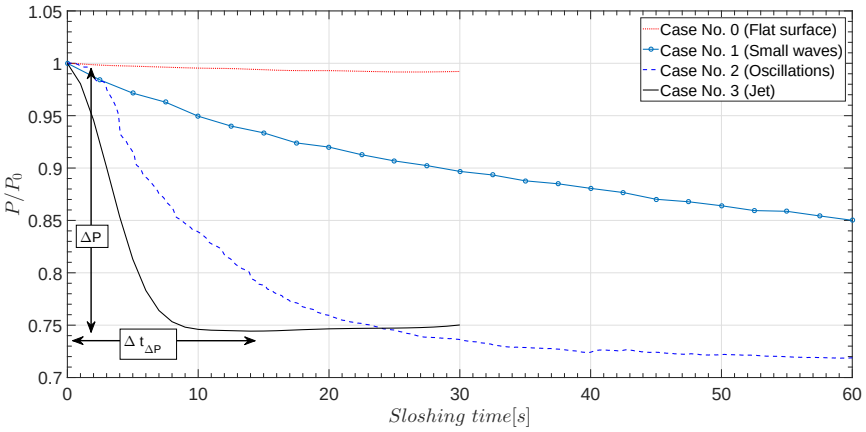

Figure 6: Measured pressure drop and its dependency on the motion frequency. P_0 is the maximum pressure before sloshing starts.

The resulting pressure evolution for the different cases is shown in Fig. 6. The sloshing starts at time 0 seconds in all cases. Although the number of sloshing time vary from case to case, only the first 60 seconds are shown in the figure. The heating element is turned off throughout the sloshing tests presented in this section.

It is clear that the most severe sloshing results in the most significant pressure drop. The pressure decreases 25 % in approximately 10 seconds in case number 3. Case 0 has almost unchanged pressure drop, while the pressure in case number 1 has not reached a minimum value after 60 seconds. The reason for the lower pressure in case number 2 is the lower air content in the gas. The results indicate that the pressure drop rate is large due to the large area of the broken free surface. The results also indicate that pressure is influenced by oscillating waves where the free surface area is significantly less than in case number 3. The local condensation takes place due to the large area and depends on hold up time and the size of the liquid drops and gas bubbles [12]. The condensation close to the interface between the gas and liquid rely on transport of energy between the interface and liquid bulk.

5.2. Validation of the model

Comparison of pressure and temperature is shown in Fig. 7 - Fig. 9. The time $t = 0$ $[s]$ is a few seconds after the actual start of the motion. This is because the product $h_{iL} \cdot A_i$ represent an average value during the sloshing time, and the start is not representative for this average. The agreement is good considering that

only a single parameter is tuned to represent sloshing intensity. The experimental temperatures in the figures are from the lower- and uppermost sensors in the liquid and gas. A mean value is found by interpolating between the saturation temperature and the bottom and top temperature. An equilibrium temperature is reached in case number 2 and 3. The time to reach this condition is much longer in case number 2 than in 3. The pressure in case 1 has not reached its minimum value when the sloshing stops. Case 0 is not included in the figure.

It can be seen from the measurements that the raise of the liquid temperature occur at a later time when the largest decrease in pressure already has taken place. It happens earlier in case 3 compared to case 2. This is due to the time it takes before the energy is mixed out from the interface to the bottom. Still, the pressure has almost reached a minimum value before the bottom temperature is affected. The pressure is sensitive to local condensation rates. For large fillings the liquid temperature is not influenced before a certain time of bulk mixing. As the condensation rate in the model is directly related to the bulk convection, and the spatial variation is unknown, the liquid temperature will increase differently than in the experiments. The condensation rates are not predicted correctly, but the tuned value gives the resulting pressure evolution. It must be noted that significant amount of gas is condensed in case number 2 before the liquid temperature at the bottom increases. Much less break-up of the surface is found in case number 2 than 3, and so a much less condensation rate is expected.

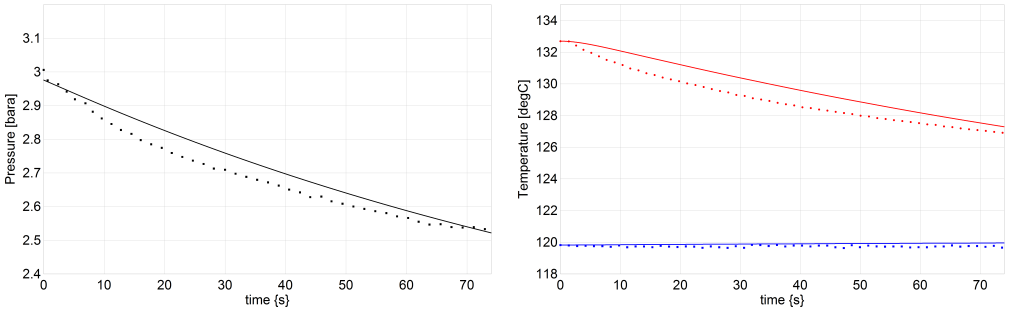

Figure 7: Pressure (left) and temperature (right) from **case 1** (Small waves) comparing experiments and simulations.

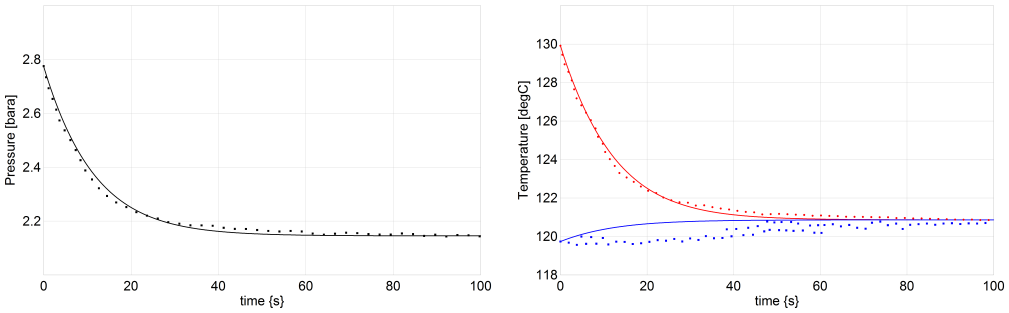

Figure 8: Pressure (left) and temperature (right) from **case 2** (Oscillations) comparing experiments and simulations.

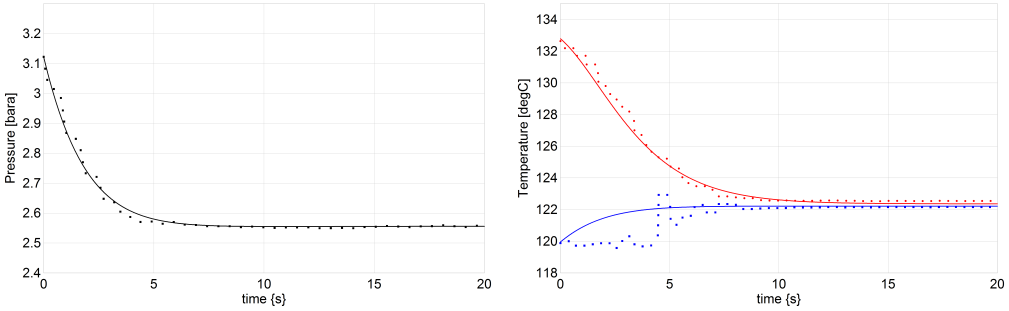

Figure 9: Pressure (left) and temperature (right) from **case 3** (Jet) comparing experiments and simulations.

Table 3: Results found from simulations and experiments. $m_{0,air}/m_{0,tot}$ is the initial mass fraction of air in the gas, $-\Delta P$ [bar] is the total pressure drop, P_{max} [bar] is the maximum absolute pressure before sloshing, $\Delta t_{\Delta P} \cdot f$ is the number of motion cycles to reach the minimum pressure, $h_{iL} \cdot A_i$ and $h_{iG} \cdot A_i$ $[W/m^2 \cdot K] \cdot [m^2]$ are the heat transfer coefficients times the interface area and $\Delta m_{cond}/\Delta m_{0,vap}$ is the total condensed mass fraction of the initial vapour mass during $\Delta t_{\Delta P}$.

Case No.	$\frac{m_{0,air}}{m_{0,gas}}$	$-\Delta P$ $[bar]$	P_{max} $[bar]$	$\Delta t_{\Delta P} \cdot f$	$h_{iL} \cdot A_i$	$h_{iG} \cdot A_i$	$\frac{\Delta m_{cond}}{m_{0,vap}}$
0	0.470	0.037	4.0254	N/A	9	50	0.02
1	0.030	0.453	3.0213	N/A	35	40	0.15
2	0.075	0.642	3.0086	40	330	170	0.23
3	0.240	0.569	3.1221	6	2500	50	0.21

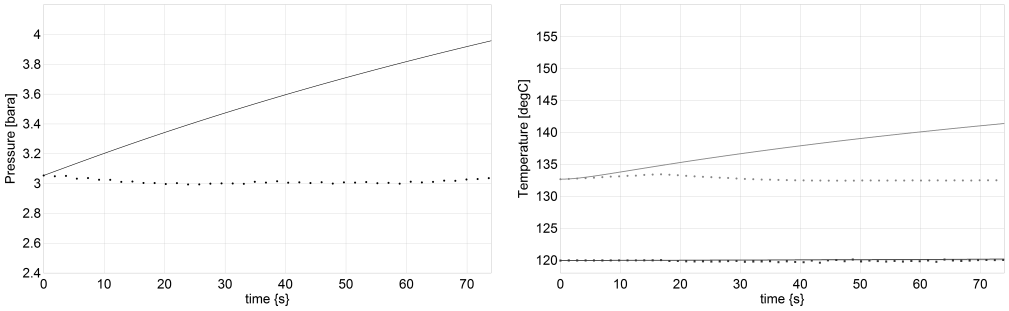

Figure 10: Pressure (left) and temperature (right) from case 1 with heat compensation and same tuning as in Fig. 7.

Tuned parameters and the results for all cases are shown in Table 3. Some differences between the initial values exist, like the pressure and the air content. The lower air content in case number 2 results in even lower pressure. It is also seen that more than 20 % of the initial vapour mass is condensed in case number 2 and 3, which results in a equilibrium condition. It can be seen from the table that the interface area is not separated from the heat transfer coefficient, as the interface area is unknown. An alternative way may be to predict the area using CFD methods, but this would hardly be accurate in case number 3. Its worth mentioning that the undisturbed interface area is 0.3557 m^2.

5.3. Prediction of heat compensation

The purpose of the PBU is to control the pressure when the liquid level is reduced. The same principle is used in land-based facilities. The power needed to compensate for the rapid pressure loss due to sloshing is a relevant matter. The PBU must deliver the same energy that corresponds to the condensation of the gas. The reduction in gas density has the largest influence on the pressure drop, and so the PBU must deliver the same amount of mass that is condensed.

The theoretical prediction of the mass flow for a given input power on the heating element can be calculated by Eq. 7. Experiments have been conducted to relate the power input, assumed to be $\dot{Q}_{PBU}$, to the mass flow of vapour. The results indicate that the mass flow is approximately 90 % of the theoretical value. Some external heat losses are expected. The relation between power and mass flow shows almost a linear trend.

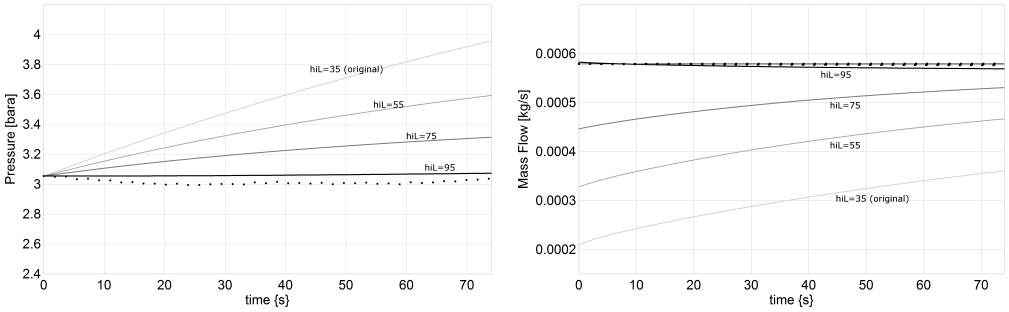

Figure 11: Pressure (left) and temperature (right) from case 1 with compensation and *increased* condensation rate relative to the initial settings in Fig. 10.

Case number 1 was found to have low enough frequency for the heating element to compensate for the pressure loss. The motion parameters are given in Table 2. The result is shown in Fig. 10. It can be seen that the pressure and temperature is over-predicted when the heating element is included in the simulations. The reason is probably the increased condensation rate when the gas is pressurized. In our model, this must accounted for by changing h_{iL}. By increasing this parameter slightly, we see that the mass flow of condensation approach the mass flow of the heating element (Fig. 11). Tuning of the heat transfer coefficient should be unnecessary in the case of pressurization. This is a consequence of the definition of the mass flow rate in our model.

The mass transfer at the interface due to condensation can be related directly to the pressure drop by differentiating Eq. 13 and assuming no change in the gas volume,

$$\frac{dm_L}{dt} = -\frac{m_G}{P} \cdot \frac{dP}{dt} + \frac{m_G}{T_G} \cdot \frac{dT_G}{dt}. \tag{16}$$

The change in temperature has minor effect on the pressure loss, and the rightmost term may be excluded. The power needed by the PBU is then the mass flux found from the pressure drop rate multiplied by the specific enthalpy of formation,

$$\dot{Q}_{PBU} = \frac{dm_L}{dt} \cdot h_{fg} \approx -\frac{m_G}{P} \cdot \frac{dP}{dt} \cdot h_{fg}. \tag{17}$$

We apply this to the measured pressure from case 1-3 by calculating the pressure drop rate numerically. The result is given in Fig. 12.

The calculated PBU power, $\overline{\dot{Q}}_{PBU}$ averaged over a sloshing cycle is given in Table 4. The power in case 1 varies in all of the 5 cycles shown. The sloshing is less intense, so the pressure drop is distributed over a longer period of time. In case 2 and 3, the pressure curve is steeper in the beginning and worst in case 3. The only case where a difference with and without compensation was found, is in case 1, as presented earlier in this section. The power supply to the element is limited to 1461 [W] in all of these tests. The reason is

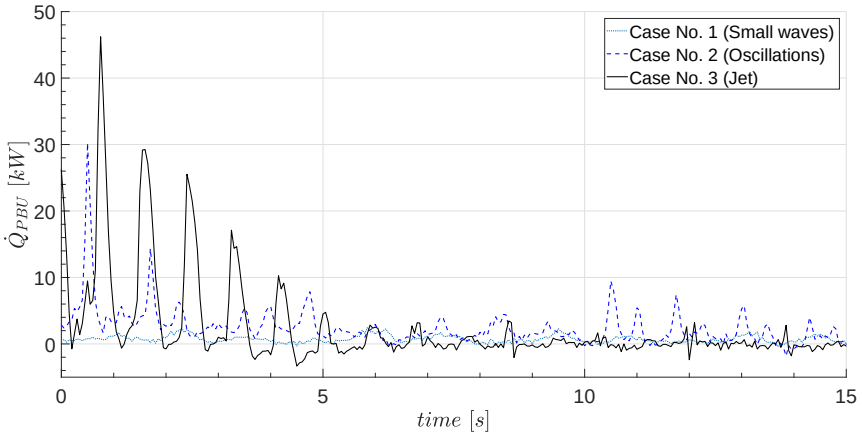

Figure 12: PBU power need estimated from the measured pressure.

Table 4: Predicted PBU power needed to compensate for the pressure drop is averaged the first 5 sloshing cycles.

Sloshing cycle no.:	1	2	3	4	5
		$\overline{\dot{Q}}_{PBU}$ [kW]			
Case 1:	0.976	0.711	0.845	0.638	0.599
Case 2:	3.808	2.676	2.107	2.346	1.506
Case 3:	11.486	7.235	1.731	0.373	0.279

limitations in the equipment. The theory predicts somewhat less power needed for compensation, equal to 980 [W] in case 1. Averaging over an even smaller part of the first cycle result in even larger power need.

6. Scaling and similarity analysis

Water has been used as a substitute for natural gas at model scale. The aim of the paper is not to find a substitute to LNG, but rather to investigate the phenomenon of sloshing enhanced mixing and pressure drop. This is why water is considered a good option. However, if results should be applicable to full scale there would need to be some scaling involved. A full scale tank may be as long as 30 metres, with a diameter of 5 metre. A prerequisite to perform model tests is to ensure geometrical similarity. For this tank type, the length-to-diameter, L/D must be the same. The tank heads and length of cylindrical section must have the same ratios. The non-dimensional filling (filling-to-length), h/L must be the same as well.

Scaling that considers fluid properties as well as compressible flow is not that easy to perform. Criteria for scaling of LNG sloshing was presented in Bass et al. [21]. In general, Froude analysis is sufficient if incompressible scaling is considered. This is true for the hydrodynamics. Most literature focus on scaling to ensure the correct impact pressure [2], but this is of less importance here and the assumption of incompressible

flow is assumed to be good enough.

Froude scaling is applied by requiring the same Froude number in model and full scale. It is defined as

$$Fr = \frac{U}{\sqrt{gL}}, \tag{18}$$

where U and L are characteristic velocity and length respectively, while g is the gravity acceleration. Taking the velocity as the tank length divided by the sloshing period, T the criteria for scaling the motion period gets

$$T_m = T_f \sqrt{\lambda}, \tag{19}$$

and λ being the scale factor, $\lambda = L_m/L_f$. The subscripts m and f refer to model- and full scale respectively. Translational motion amplitude is scaled the same way, while angle amplitude is the same in model and full scale.

Scaling the motion like this may not be entirely correct without considering the Reynolds number. Although the fluid properties are quite different between natural gas and water, these differences are not within the scope to investigate.

What the thermodynamic response concerns, and condensation due to thermal mixing between liquid and gas, there are additional requirements for scaling. As the liquid subcooling is essential, while the gas superheating may be less important, the liquid *Jakob number* must remain the same. It is defined as the ratio of sensible to latent heat,

$$Ja = \frac{c_{v,L}\left(T_L - T_{sat}\right)}{h_{fg}}. \tag{20}$$

$c_{p,L}$ is the specific heat capacity and h_{fg} is the specific latent heat of formation. This requirement certainly involves fluid properties.

Another requirement is to ensure the same *thermo-mechanical* conditions. It may be enforced by considering an equation of state, like the ideal gas law, $P = \rho RT$. Scaling must satisfy:

$$\left(\frac{P}{\rho_G R T_G}\right)_f = \left(\frac{P}{\rho_G R T_G}\right)_m. \tag{21}$$

R is the gas constant and depends on the type of gas. If the gas is saturated, pressure and gas temperature are not both free variables. This would leave liquid bulk temperature, T_L and tank pressure, P as the only free variables.

LNG consist of 90 % methane. Comparing the properties of methane and water results in a linear relationship of ΔT and pressure. An example shows that a subcooling of $\Delta T_f = 6$ $[^\circ C]$ with liquid methane would need to be $\Delta T_m = 16$ $[^\circ C]$ with water. The influence of pressure is insignificant. If the same is done with Eq. 21, it is found that a pressure of 4-6 [barg] with methane would need to be as much as 15 [barg] with water. This condition is difficult to meet.

It is likely to believe that other factors matters than those mentioned here. For future studies, scaling should be investigated for these applications. This could be done by reducing the scale factor successively by increasing the tank size. Instead of comparing water and methane, the same considerations could be done with nitrogen and water to see if the scaling is satisfactorily. Improving the experimental facilities would be necessary. Another possibility to find the influence of fluid properties on sloshing is to run CFD simulations and systematically by changing viscosity and density.

7. Conclusion

The thermal response in a horizontal aligned pressure vessel of similar form as a marine LNG fuel tank was investigated by conducting experiments with a model scaled tank filled with water. Sloshing tests with a transparent tank has also been performed to study the the characteristic motion for different filling and frequencies. A theoretical analysis of the thermodynamics inside the tank was presented. The theory was implemented into a dynamic system model using the bond graph methodology. The model is based on tuning of parameters making a best fit of the results to extract information without performing steady-state calculations. The applicability of the model was investigated by estimating the PBU heat capacity. An estimate of the necessary heat capacity of the PBU from the measured pressure was presented. Scaling and similarity is discussed in the end of the paper.

The following conclusions can be made:

- Employing numerical integration to perform theoretical analysis is efficient and accurate. It provides the same information as steady-state calculations, but is less tedious.
- The mass flow rate of condensation and the pressure drop rate is proportional to the temperature difference between the saturation temperature and the liquid bulk temperature.
- The thermal equilibrium condition depends on the starting condition, while the pressure drop rate depends on the sloshing intensity. The sloshing intensity may be represented by the proposed parameter, $h_{iL} \cdot A_i$ which is nearly constant during the quasi-steady sloshing event.
- The time to reach the pressure minimum is the same time it takes to even out the temperature gradient on the liquid side.
- The time-instant heat required to maintain pressure was calculated numerically from the measured pressure. Time-averaged values are comparable to the measured ones, but this requires more investigation.
- The predicted heat needed to maintain pressure was significantly higher than the maximum PBU-power available. It is unlikely that an ordinary PBU has enough capacity to maintain pressure even in the case of less severe sloshing.
- Scaling of hydrodynamic motion and thermodynamic state may be considered separately if a two-way coupling due to compressible effects are neglected. Water as a substitute for methane is difficult in practice due to the different fluid properties.

Further work consist in improved formulation of the condensation mass flow rate. The definitions of the heat transfer coefficients must be changed to separate the heat transfer area. Including non-uniform temperature fields in the model would also improve the results. The effect of the heat transfer between fluid and walls should be investigated.

Acknowledgement

The authors would like to thank the staff at the Department of Maritime Technology and Operations for providing lab facilities and materials necessary to perform the experiments. This study is a part of a PhD project funded by NTNU in Ålesund.

References

[1] V. Æsøy, D. Stenersen, Low emission LNG fuelled ships for environmental friendly operations in arctic areas, in: ASME 2013 32nd International Conference on Ocean, Offshore and Arctic Engineering, American Society of Mechanical Engineers, 2013, pp. V006T07A028–V006T07A028.

[2] O. M. Faltinsen, A. N. Timokha, Sloshing, Cambridge University Press, 2009.

[3] E. Grotle, V. Æsøy, E. Pedersen, Modelling of LNG fuel systems for simulations of transient operations, Maritime-Port Technology and Development (2014) 205.

[4] E. W. Lemmon, M. L. Huber, M. O. McLinden, NIST Standard Reference Database 23: Reference Fluid Thermodynamic (2013). doi:http://dx.doi.org/10.18434/T4JS3C.
URL https://www.nist.gov/srd/refprop

[5] M. E. Moran, N. B. Mcnelis, M. T. Kudlac, M. S. Haberbusch, G. A. Satornino, Experimental results of hydrogen slosh in a 62 cubic foot (1750 liter) tank (1994).

[6] J. Lacapere, B. Vieille, B. Legrand, Experimental and numerical results of sloshing with cryogenic fluids, in: Progress in Propulsion Physics, Vol. 1, EDP Sciences, 2009, pp. 267–278.

[7] T. Arndt, Sloshing of Cryogenic Liquids in a Cylindrical Tank under normal Gravity Conditions, Universtität Bremen, 2011.

[8] C. Ludwig, M. Dreyer, E. Hopfinger, Pressure variations in a cryogenic liquid storage tank subjected to periodic excitations, International Journal of Heat and Mass Transfer 66 (2013) 223–234.

[9] E. L. Grotle, K. H. Halse, E. Pedersen, Y. Li, Non-isothermal sloshing in marine liquefied natural gas fuel tanks, in: The 26th International Ocean and Polar Engineering Conference, International Society of Offshore and Polar Engineers, 2016.

[10] S. M. Ghiaasiaan, Two-phase flow, boiling, and condensation: in conventional and miniature systems, Cambridge University Press, 2007.

[11] F. Kreith, R. F. Boehm, Direct-contact heat transfer, Springer Science & Business Media, 2013.

[12] S. Sideman, D. Moalem-Maron, Direct contact condensation, Advances in Heat Transfer 15 (1982) 227–281.

[13] H. B. Mahood, R. B. Thorpe, A. N. Campbell, A. O. Sharif, Experimental measurements and theoretical prediction for the transient characteristic of a two-phase two-component direct contact condenser, Applied Thermal Engineering 87 (2015) 161–174.

[14] J. Joseph, G. Agrawal, D. K. Agarwal, J. Pisharady, S. S. Kumar, Effect of insulation thickness on pressure evolution and thermal stratification in a cryogenic tank, Applied Thermal Engineering 111 (2017) 1629–1639.

[15] D. Karnopp, State variables and pseudo bond graphs for compressible thermofluid systems, Journal of Dynamic Systems, Measurement, and Control 101 (3) (1979) 201–204.

[16] P. O. Moksnes, Modeling two-phase thermo-fluid systems using bond graph, Dr. ing thesis, University of Sciences and Technology, Department of Marine Engineering, Norway.

[17] E. Pedersen, Modelling multicomponent two-phase thermodynamic systems using pseudo-bond graphs, SIMULATION SERIES 33 (1) (2001) 257–263.

[18] J. Thoma, B. O. Bouamama, Modelling and simulation in thermal and chemical engineering: A bond graph approach, Springer Science & Business Media, 2013.

[19] M. Moran, H. Shapiro, Fundamentals of Engineering Thermodynamics, Wiley, 2004.

[20] Controllab Products, 20-sim, `http://www.20sim.com`, [Online; accessed 31-January-2017] (2017).

[21] R. Bass, E. Bowles, R. Trudell, J. Navickas, J. Peck, N. Yoshimura, S. Endo, B. Pots, Modeling criteria for scaled lng sloshing experiments, Journal of Fluids Engineering 107 (2) (1985) 272–280.

Paper VII

Paper 7 - Numerical Simulations of Sloshing and the Thermodynamic Response due to Mixing.

Grotle, Erlend Liavåg; Æsøy, Vilmar. (2017)
Energies. vol. 10(9), 1338.
(http://dx.doi.org/10.3390/en10091338).

energies

MDPI

Article

Numerical Simulations of Sloshing and the Thermodynamic Response Due to Mixing

Erlend Liavåg Grotle * and Vilmar Æsøy

Department of Ocean Operations and Civil Engineering, Faculty of Engineering Science, Norwegian University of Science and Engineering, Larsgårdvegen 2, 6009 Ålesund, Norway; vilmar.aesoy@ntnu.no

* Correspondence: erlend.l.grotle@ntnu.no; Tel.: +47-99649968

Received: 17 August 2017; Accepted: 1 September 2017; Published: 5 September 2017

Abstract: In this paper, we apply computational fluid dynamics (CFD) to study the thermodynamic response enhanced by sloshing inside liquefied natural gas (LNG) fuel tanks. An existing numerical solver provided by OpenFOAM is used to simulate sloshing in a model scaled tank of similar form to an LNG fuel tank. The interface area has been estimated for different sloshing regimes on three different numerical grids representing the tank in 3D. Estimating the interface area is done by performing a grid-independence study. In the most severe sloshing conditions, convergence is not achieved. By combining the results from experiments and CFD, it is found that the interface area and the condensation mass flow rate are in phase for the most severe sloshing condition. The existing CFD solver is modified to determine the pressure drop. The simulation results are compared to the experimental data, and the results are acceptable and thereby show a potential in applying CFD to predict the thermodynamic response due to sloshing. By plotting the temperature contours, indications are found that the exchange of cold bulk and saturated liquid due to sloshing has a significant influence on the thermodynamic response.

Keywords: sloshing; thermal mixing; pressure drop; LNG fuel tank; CFD; OpenFOAM

1. Introduction

LNG as a fuel has proven beneficial for the environment [1]. The number of LNG-fuelled ships has increased in recent years, but operational experience shows that there are still challenges to ensuring reliable operation. One of them is related to the thermodynamic response inside LNG fuel tanks enhanced by liquid sloshing. Sloshing can be characterized as the motion of liquids in containers or vessels [2]. The rapid pressure drop is related to the movement of the tank, filling depth and the temperature of the bunkered LNG. In low-pressure fuel systems, there is no mechanical pump and the tank pressure is the driving force to transport fuel to the gas engines [3]. If the system pressure drops below a specific minimum, the worst consequence is a shutdown of the gas engines [4]. To stabilize the pressure, LNG is vaporized in a closed loop from the bottom to the top of the tank. This principle of using a *pressure build-up unit* (PBU) by the supply of heat is similar to land-based storage of LNG. However, the motions onboard a ship will enhance the transport of thermal energy, which leads to rapid pressure drop.

The potential pressure drop may be explained by looking at the co-existence curve for methane in Figure 1. The pressure drop corresponds to the temperature difference between the equilibrium temperature and the saturation temperature of the operational pressure. The operating pressure corresponds to a T_{sat}, which is initially higher than the bunkered liquid temperature. As the liquid mass is dominating, the final temperature will be much closer to the initial liquid temperature, with a *liquid-side controlled* process. Transportation of the cold liquid bulk and the mixing with the

gas is relevant. This further depends on the sloshing regime and the bunkered LNG temperature. LNG consists of several components, with the major one being methane. The effect of more than one component is excluded in this study.

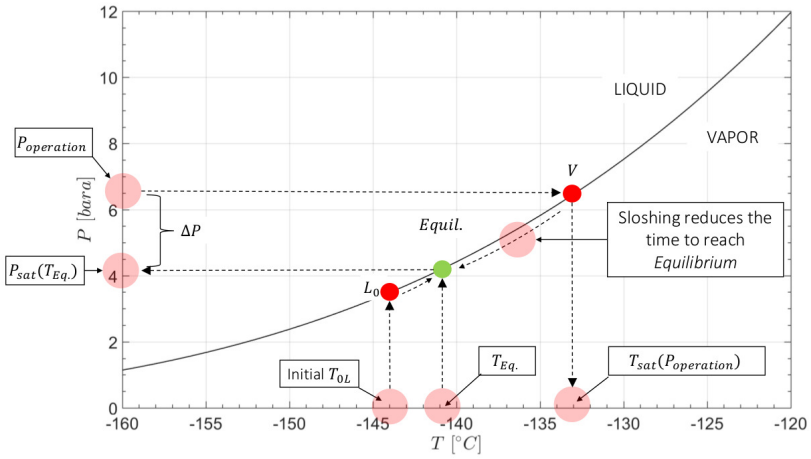

Figure 1. Co-existence curve for methane. The liquid acts as an internal energy sink to the system. Thermal equilibrium results in lower tank pressure. Sloshing reduces the time to reach the final state. The *p*-*T* data was generated using REFPROP v9.1 [5].

Sloshing experiments with liquefied nitrogen LN_2 were conducted by Grotle et al. [6]. The effect of the frequency and initial tank pressure was investigated. It was found that the final state mostly depends on the initial state, while the pressure drop rate depends on the sloshing intensity and may be correlated with the non-dimensional frequency, $f/f_{1,0}$, where $f_{1,0}$ is the first mode natural frequency. The exception is low frequencies, where it takes significantly longer time to reach thermal equilibrium. Heat ingress will become relevant in those cases.

Most studies of sloshing hydrodynamics consider vertically aligned cylindrical tanks for aerospace applications, or rectangular tanks. However, sloshing studies of horizontally aligned cylindrical tanks with spherical heads are limited and are therefore considered in this project.

Moran et al. [7] conducted experiments in a 62 $[ft^3]$ container with liquefied hydrogen. They investigated the thermodynamic response due to sloshing by performing experiments with varying excitation frequency. The pressure collapse magnitude was recorded, as well as the temperature at different locations. Unstable sloshing conditions with an excitation close to the first mode natural frequency was found to have the greatest impact on the pressure drop, while stable sloshing was found to have a minor effect. Lacapere et al. [8] compared experimental results and numerical simulations to investigate the influence of interface heat and mass transfer on the pressure evolution due to sloshing using both liquefied nitrogen (LN_2) and liquefied oxygen (LO_x). Comparison between the numerical simulations and experiments showed that the de-stratification in the liquid is responsible for the large pressure drop. Arndt [9] presented experiments in his Ph.D. thesis and found that the presence of non-condensible gas reduces condensation while evaporation increases. This indicates that condensation is responsible for the majority of the energy transfer that causes the pressure drop. Ludwig et al. [10] conducted several experiments using LN_2 in a vacuum-insulated upright cylindrical tank. All of the experiments were conducted with one translational motion amplitude, except in the last case. The excitation frequency was varied in proximity to the first mode natural frequency, representing regimes that cover the range of stable planar wave motion to swirl waves. The Nusselt

number was introduced to correlate with the sloshing Reynolds number based on wave amplitude and frequency.

Lin et al. [11] studied the effect of jet-induced mixing on the pressure reduction of a thermally stratified liquid hydrogen tank. In literature, this is a more common problem than mixing due to sloshing. Mixing time correlations were developed based on both thermal equilibrium and pressure equilibrium. The mixing time of such problems are typically correlated with jet velocity and diameter.

Obviously, it would be beneficial to predict the pressure response in sloshing events for any tank geometry and internal structures. CFD also offers great possibilities to study any modelled variable and is not limited by the instrumentation. Although the experiments are the most realistic research method, they do include uncertainties.

Many CFD studies dealing with phase change can be found in the literature. Juric and Tryggvason presented a method to compute boiling flows [12]. It is based on the single field formulation where one set of equations is solved. Both complex and simplified jump conditions are presented. The numerical implementation with finite difference discretization is also outlined in the paper. Good accuracy was found from the validation studies. Welch and Wilson [13] developed a volume-of-fluid (VOF) based method to simulate phase change in two-phase flow using simplified jump conditions combined with the Youngs enhancement of the VOF method [14]. Other developments of CFD-modelling with phase change have been performed by Hardt and Wondra [15] and Gibou et al. [16].

An important aspect of such simulation models is how to approximate the mass and energy jump conditions at the interface. The above-mentioned methods are all based on the single field approach, where one set of equations is solved. The numerical implementation of the interface conditions is a difficult issue and requires special consideration. An alternative to the single field approach is the Euler–Euler method, or two-equation models. This is computationally more demanding, and it is uncertain whether the method is suitable for the large deformations of the free surface. Accurate representation of the free surface has proven to be possible with the single-field approach, so an extended VOF-based solver is therefore chosen to be used in this work.

Our aim is to develop a simple but realistic model to study the sloshing event. This is based on the assumption that exchange of liquid from bulk to interface is necessary for condensation to take place, independently of the local condensation mechanisms. The resistance due to thermal mixing is thus considered to be dominating relative to the thermal resistance at the interface. Modelling details of phase change mechanisms is not the aim. Relevant studies that apply to existing CFD methods includes Liu et al. [17,18], who performed CFD studies of pressurization and stratification phenomenon in a cryogenic tank. Similar implementations in OpenFOAM (version 2.1.1, The OpenFOAM Foundation, London, UK) have been done by Haider [19] and Kunkelmann [20] in their Ph.D. thesis. Georgoulas et al. [21] implemented an improved VOF method to simulate bubble detachment in pool boiling.

2. Experimental Work

Experiments have already been conducted in former work to study both sloshing hydrodynamics with a transparent model tank and a pressure tank made of steel to investigate the thermodynamic response. Both tanks have the same geometry. Two experiments were needed because the sloshing can not be observed with the steel tank. Figure 2 shows the experimental set-up for the thermal tank tests. The tank geometry and dimensions are the same.

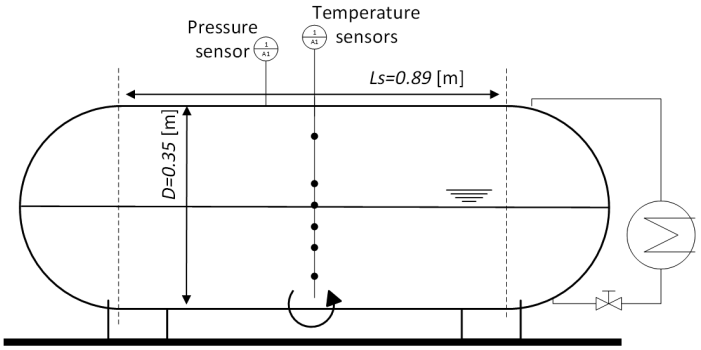

Figure 2. Thermal tank and the instrumentation.

The experimental rig consists of a movable platform with one degree of freedom. The tank rotates around the bottom centerplane of the tank in all tests, and the angle amplitude is equal to three degrees. The motion is created by an electro motor and a crank mechanism. As the crank arm is long compared to the radius, $L_s >> R$, the angle of the platform is approximately $\theta(t) \approx A \cdot sin\,(2\pi f \cdot t)$, where A is the amplitude, f the frequency and t is time. Several fillings and frequencies have been tested with the transparent tank to investigate sloshing characteristics. The thermal test was conducted with one filling and several frequencies. The hydrodynamic tests were conducted with water (and air), while the thermal tank tests with a mixture of liquid water and vapour and minor air content. The fact that a water/air mixture at room temperature is compared to a water liquid/vapor mixture close to the boiling point might be considered slightly controversial. The liquid density is almost unchanged, and $\rho_L/\rho_{L,max}$ varies between 1 and 0.95 at a temperature 10 and 120 °C, respectively. Another issue is the density ratio between the gas and the liquid in each case. Maillard and Brosset [22] presented experimental studies on the influence of the density ratio between liquid and gas considering also volatile conditions. This was found to have an impact on the exchange of momentum between liquid and gas.

The density relationship between the ambient air (in the transparent case) and the vapour is given in Figure 3. It can be seen that the ratio is approximately equal at 120 °C. The gas temperature may be as high as 135 °C so the density ratio is not very different.

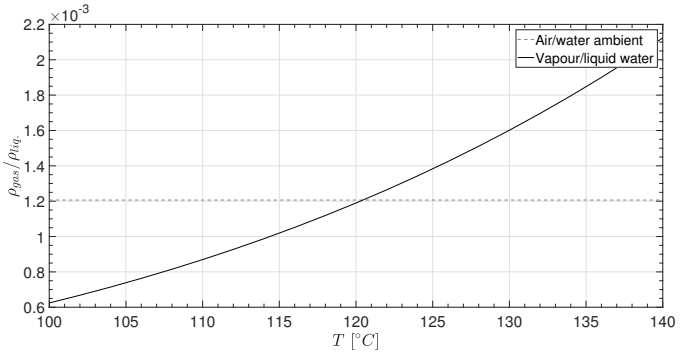

Figure 3. The density ratio between gas and liquid. Comparison between the test conditions with air/water and water vapour/liquid.

Table 1 lists the conditions that are considered in this paper. h is the mean filling depth and D is the diameter. L_s (m) is the straight length of the cylindrical section, f (Hz) is the excitation frequency and $f_{1,0}$ is the first mode natural frequency calculated for a rectangular tank with the same length as the straight cylindrical section. RPM_m is the rotational speed of the electro motor, t_s (s) is the sloshing time and T is the motion period equal to $1/f$, such that t_s/T is the number of sloshing cycles. In case 0, there is no motion and it acts as a reference condition. In case 1, there are only small deformations of the free surface. In case 2, many interacting waves are present and rapid oscillations of the free surface take place. In the last case 3, a liquid jet is found due to the spherical heads. The motion is severe in the last case and breaks up the liquid surface. These characteristics are presented later in the results.

Table 1. Sloshing test conditions.

Case No.	h/D	h/L_s	f (Hz)	RPM_m	$f/f_{1,0}$	t_s/T	Description
0	0.50	0.190	N/A	N/A	N/A	N/A	No motion
1	0.50	0.190	0.29	857	0.427	40	Small deformation
2	0.50	0.190	0.40	1200	0.495	31	Oscillating waves
3	0.50	0.190	0.57	1714	0.840	30	Jet formed

Hydrodynamic tests have been performed to know which frequencies should be investigated in the thermal tank test. The free-surface elevation was measured with an ultrasonic sensor, model Sick UM12 (Sick Inc., Minneapolis, MN, USA). The accuracy of this sensor is $\pm$1% with a repeatability of $\pm$0.15%. It was mounted on the top of the straight cylindrical section on the transparent tank. Videos of all the sloshing tests are recorded, using a GoPro Hero4 camera (GoPro Inc., San Mateo, CA, USA). The free-surface elevation was only possible to measure in tests with low filling because the sensor does not work in contact with water. This disadvantage should be improved in future studies.

Experiments to study the thermodynamic response due to sloshing was performed with an insulated cylindrical pressure tank made of steel. It consists of instrumentation like a pressure sensor and several thermocouples placed vertically in the middle of the tank, as seen in Figure 2. A variant of a pressure build-up unit (PBU) has been installed on the right side of the tank. It consists of a copper element heated with external voltage supply. The heater is placed lower than the mean depth, and the flow is driven by hydrostatic pressure differences. The relationship between mass flux and power supply is measured in advance to know the amount of vapour.

The test procedure consists of initial heating of the liquid from approximately 15–20 °C to 118–119 °C. The liquid temperature must be high to prevent any air content, and $T_{sat} - T_L$ does not get too large. The PBU power to generate vapour has been limited to 1460 W in these tests. To build up the system temperature, it can be switched between pressurisation with the heater and sloshing. The thermal energy is then mixed more efficiently inside the tank. When the system is ready for sloshing tests, the pressure is increased to the desired value. The heater is turned off and the electro-motor starts with a specified frequency and number of periods.

3. Mathematical Models and Numerical Methods

3.1. Problem Description

Numerical simulations have been performed with OpenFOAM (version 1606+, OpenCFD, London, UK). The fluid domain consists of the inner tank with the same geometry as tested in the experiments (Figure 2). Figure 4 shows the definition of the semi-elliptic heads. The crown radius, R_k, and the pull-out length of the head, Z, are all scaled according to the inner diameter, which is 0.3473 m. Both tank heads are connected to a straight cylindrical section in the middle with the length $L_s = 0.89\ m$.

The 3D geometry was constructed with the CAD tool Siemens NX (version 11.0, Siemens PLM Software, Plano, TX, USA). To generate the 3D grid, the tank geometry was exported as a *.stl* file.

The *snappyHexMesh* tool in OpenFOAM is capable of reading this file format. A rectangular mesh was first generated with the *blockMesh* command, and then the final geometry by the use of *snappyHexMesh*. No additional mesh refinement has been done along the walls, but the *no-slip* wall boundary condition was employed on the whole surface of the tank.

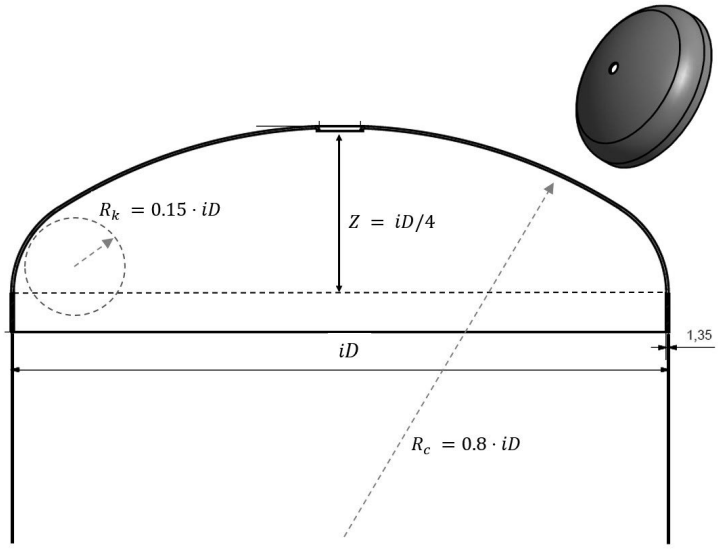

Figure 4. Semi-elliptic heads.

This is a time-dependent problem and there is no tank motion initially. Convergence of the solving process is therefore less dependent on the initial conditions. There is no velocity in the tank and all motion-related variables are set to zero. What is important to specify is the volume of fraction of liquid and the temperature. The first one is executed by using the *setFields* functionality in OpenFOAM. Choosing the mean depth as a starting point is easily done with the *boxToCell* method. The starting temperature profile is the same as found in the experiments. The vertical profile is shown in Figure 5. The gas and liquid properties are kept constant, and the mixture density and viscosity varies with α. The temperature is read as a non-uniform list.

The individual fluid properties of liquid and gas is kept constant and only varied by the volume fraction of liquid. The specific enthalpy of formation is kept constant and equal to 2.257×10^6 [J/kg]. The values are given in Table 2.

Table 2. Fluid properties.

Phase	ρ (kg/m^3)	ν (m^2/s)	c_p (J/kg · K)	k (W/m · K)
Liquid	997.56	8.91×10^{-7}	4180	0.62
Gas	1.18	1.57×10^{-5}	1500	0.03

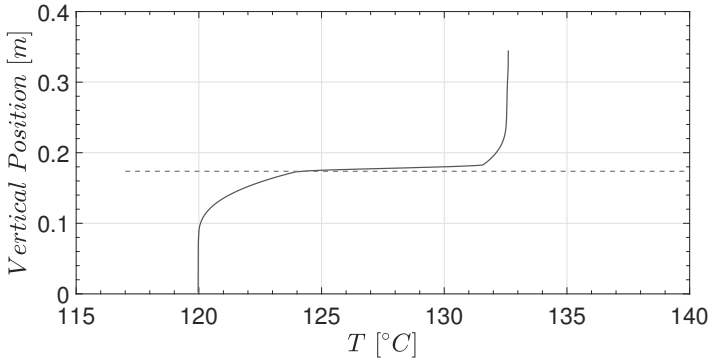

Figure 5. Vertical temperature profile inside the tank at the start of sloshing.

3.2. CFD-Model

It is assumed that the flow is incompressible, such that

$$\nabla \cdot \mathbf{v} = 0, \tag{1}$$

where $\mathbf{v}$ is the mean velocity vector.

The Reynolds-averaged Navier–Stokes equations (RANS) are solved numerically with a pressure-correction algorithm. The equation is written in tensor notation as [23]

$$\frac{\partial}{\partial t}(\rho \mathbf{v}) + \nabla \cdot (\rho \mathbf{v}\mathbf{v}) = -\nabla p + \nabla \cdot \left\{ (\mu + \mu_t) \left[\nabla \mathbf{v} + (\nabla \mathbf{v})^{\mathrm{T}} \right] \right\} + \mathbf{f}_b. \tag{2}$$

ρ is the density, p is the pressure, μ the dynamic molecular viscosity and $\mathbf{f}_b$ are external forces like gravity.

To account for turbulence, the Boussinesq-concept is employed, where turbulence affects the mean velocity field as additional viscosity. The turbulent dynamic viscosity, μ_t, is estimated by the use of the $k-\omega$ SST turbulence model [24–26]. The model equations implemented in OpenFOAM are

$$\frac{\partial}{\partial t}(\rho k) + \nabla \cdot (\rho \mathbf{v} k) = \tilde{P}_k - \beta^* k\omega + \nabla \cdot \{ (\mu + \sigma_k \mu_t) \nabla k \}, \tag{3}$$

$$\begin{aligned} \tfrac{\partial}{\partial t}(\rho\omega) + \nabla \cdot (\rho \mathbf{v}\omega) = \alpha \rho S^2 - \beta \rho \omega^2 + \nabla \cdot \{ (\mu + \sigma_\omega \mu_t) \nabla \omega \} \\ +2(1 - F_1)\rho \sigma_{\omega 2} \tfrac{1}{\omega} \nabla k \cdot \nabla \omega, \end{aligned} \tag{4}$$

$$\mu_t = \frac{\rho a_1 k}{\mathrm{Max}(a_1 \omega, S F_2)}, \tag{5}$$

$$\tilde{P}_k = \mathrm{Min}(P_k, 10\beta^* k\rho\omega); \quad P_k = \mu_t \nabla \mathbf{v} : \left[\nabla \mathbf{v} + (\nabla \mathbf{v})^{\mathrm{T}} \right]. \tag{6}$$

Here, S is the magnitude of the strain rate, F_1 is a blending function, which is zero away from the surface ($k-\epsilon$) and switches to unity inside the boundary layer ($k-\omega$). F_2 is the second blending function. The blended parameters are σ_k, σ_ω, α and β. The model constants, $\beta^*, \sigma_{k1}, \sigma_{k2}, \sigma_{\omega 1}, \sigma_{\omega 2}, \alpha_1, \alpha_2, \beta_1, \beta_2$ and a_1, all have default values, equal to 0.09, 0.85, 1.00, 0.50, 0.856, 5/9, 0.44, 3/40, 0.0828 and 0.31, respectively [26,27].

The ω-equation can be integrated through the wall boundary layer, which is advantageous for the near wall treatment. OpenFOAM offers near wall treatment that can automatically switch between low and high Reynolds number formulations. The solution to this is blending between the analytical solutions of ω in the viscous sublayer and the logarithmic near-wall region [28]:

$$\omega = \left[\omega_{vis}^2 + \omega_{log}^2\right]^{0.5}, \tag{7}$$

$$\omega_{vis} = \frac{6\nu}{0.075y^2}; \quad \omega_{log} = \frac{1}{0.3\kappa}\frac{u_\tau}{y}, \tag{8}$$

where y is the normal distance from the wall face to the cell center of the nearest cell. κ is the von Karman constant. A similar blending is performed for the velocity profile near the wall. The boundary condition for turbulence energy, k, at the wall is a zero gradient.

An additional transport equation is solved to find the volume fraction. The fluid properties in hydrodynamic applications are

$$\rho = \alpha_L\rho_L + (1-\alpha_L)\,\rho_G, \quad \nu = \alpha_L\nu_L + (1-\alpha_L)\,\nu_G, \tag{9}$$

where α_L is the volume fraction of liquid. ρ and ν is the density and kinematic viscosity, respectively. The volume fraction of liquid is transported in the domain by solving the equation

$$\frac{\partial\alpha}{\partial t} + \nabla\cdot(\mathbf{v}\alpha) + \nabla\cdot\{\mathbf{v_r}\alpha\,(1-\alpha)\} = 0. \tag{10}$$

The last term is an artificial compression term, where $\mathbf{U}_r$ is a velocity field suitable to compress the interface. It should act normal at the interface and can be based on the maximum velocity magnitude in the transition region [29]. An advantage of Equation (10) is that its solution for α can be bounded between 0 and 1. This is controlled by the *cAlpha* parameter in the *fvSolution* file. If equal to 1, the compression is conservative and, above 1, it is not. In this paper, the value 1.0 is used in order to obey mass conservation.

The final equilibrium state can be estimated, but the time to reach it is unknown. A method to predict the time to reach the equilibrium condition has been implemented in the existing OpenFOAM solver. The energy equation contains a source term that is activated only at the interface and is proportional to the temperature difference $(T - T_{sat})$. The saturation temperature is taken here as the average of the gas temperature (Appendix A.1). This is reasonable because it has been observed in experiments that the saturation and the gas temperature are very close and vary parallel to each other. The pressure drop rate may thus be calculated from the corresponding saturation temperature. The main assumption is that the pressure drop rate is depending directly on the rate of cooling of the gas by the liquid. Initial temperatures found in the experiments are used in the start of the simulations by interpolating the sensor values onto the grid.

The first step is to implement a thermal transport equation in the *interDyMFoam* solver. The following version is used:

$$\frac{\partial(\rho T)}{\partial t} + \nabla\cdot(\rho\mathbf{U}T) = \nabla\cdot\left[\left(k_{eff}/c_p\right)\nabla T\right] + \dot{S}_T. \tag{11}$$

The thermal conductivity k_{eff} in Equation (11) contains the molecular conductivity as well as the contribution from turbulence, k_t.

$\dot{S}_T$ is the heat source activated only at the free surface. k and c_p are mixture properties found with the volume fraction, and given as

$$\alpha_L k_L + (1-\alpha_L)k_G, \tag{12}$$

$$\alpha_L c_{p,L} + (1-\alpha_L)c_{p,G}. \tag{13}$$

The turbulent thermal conductivity is given in a classical manner as

$$k_t = \frac{\rho c_p \nu_t}{Pr_t}. \tag{14}$$

ν_t is the turbulent kinematic viscosity. The turbulent Prandtl number, Pr_t needs to be taken as a constant value. Here, we have used the value equal to 2, which is slightly larger than normal. This is because turbulence is overproduced at the surface with VOF-based two-phase calculations. The implementation of Equation (11) is given in Appendix A.2.

The source term is expressed almost similar to what was done in [17,18]. The difference is that the source term is activated only at the interface. It is given as

$$\dot{S}_T = r\,\rho\,2\alpha_L\,(1-\alpha_L)\,\frac{T-T_{sat}}{T_{sat}}\,h_{fg}/c_p. \tag{15}$$

r is a constant equal to 0.1 s^{-1}. The term $2\alpha_L\,(1-\alpha_L)$ is a harmonic mean value of the liquid volume fraction. It is zero everywhere else than at the interface. It ensures a smooth transition between the phases. The saturation temperature is updated each time step. A prerequisite for this assumption is that the thermal energy in the gas relative to saturated conditions is negligible compared to the liquid. The pressure is estimated from the saturation temperature, $P(T_{sat})$. This is done by the use of Tetens equation [30],

$$P_{sat} = 0.61078 \cdot exp\left(\frac{17.27\,T}{T+237.3}\right). \tag{16}$$

The units of pressure P and temperature T are kPa and °C, respectively.

3.3. OpenFOAM Solver InterDyMFoam

InterDyMFoam is a solver for two incompressible, isothermal immiscible fluids with optional mesh motion and mesh topology changes including adaptive re-meshing. This is ideally suited for sloshing. Mesh refinement is not performed, only motion of the whole mesh. The VOF method is used to capture the location of the interface, which determines the cells that contain gas or liquid properties.

The rotational amplitude and frequency is given in a tabulated file read by OpenFOAM. The rotational point was specified to be the same as in the experiments, as in Figure 2.

Although OpenFOAM offers a semi-implicit version of MULES [31], the maximum Courant number is limited to 0.5 in all the simulations. This ensures a small time step. When the time step is small, the pressure-velocity coupling is stronger than the nonlinear convective momentum term. It is therefore not necessary to update the velocity more than once per time step. This is essentially the Pressure-Implicit with Splitting of Operators (PISO) algorithm [32] and is chosen in OpenFOAM by setting the *nOuterCorrectors* to 1, and performing several pressure corrections, typically 3. PISO is efficient, and the accuracy is good with the strict Courant number limit. A drawback to PISO is that it is found to be more sensitive to the mesh.

The pressure-velocity coupling is traditionally dealt with using a staggered-grid technique. However, it becomes an issue on non-Cartesian and unstructured grids. In OpenFOAM, a variant of the Rhie and Chow interpolation technique [33] is used, which offers the possibility of formulating the PISO algorithm on a collocated grid. The Rhie–Chow interpolation is different in OpenFOAM, and a summary can be found in [34].

4. Results

4.1. Experiments—Thermodynamic Response with Water

The pressure from the thermal tests are compared in Figure 6. Observations from the hydrodynamic tests are are also added to show the sloshing conditions. It can be seen that, during this time of sloshing, only cases 2 and 3 have enough intensity to reach the equilibrium condition. The pressure development is quite different in all of the cases, where the most rapid pressure drop occurs in case 3. The results are similar to what was found in [6], and the most rapid pressure collapse is found when the sloshing is severe and close to the primary resonance, $f/f_{1,0} = 1$. The rise in

pressure seen after the minimum in case 3 happens because the liquid now is saturated and starts to evaporate. The only dominant energy source is now the heat ingress, as the liquid is no longer subcooled. The sudden stop in the pressure drop was also mentioned by Ludwig et al. [10], but the rise in pressure is only possible with heat ingress.

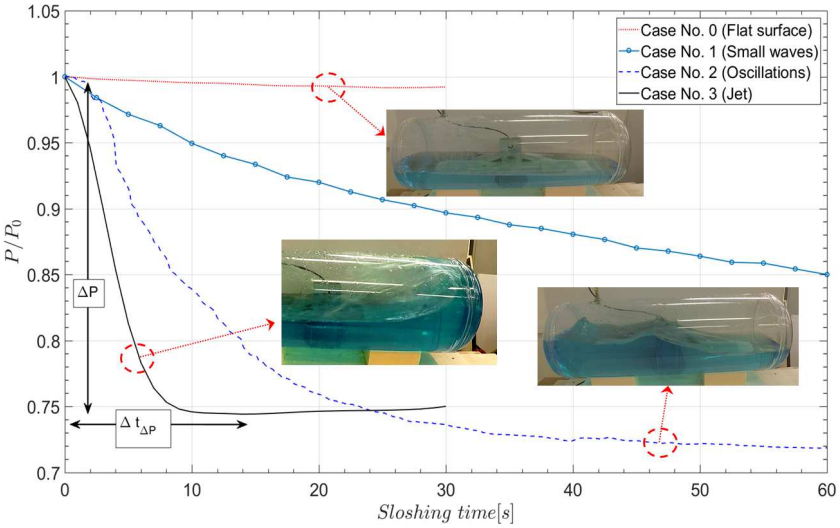

Figure 6. Measured pressure drop and its dependency on the motion frequency.

4.2. Grid Independence Study

Three different grid resolutions have been compared by simulating sloshing hydrodynamics and calculating the interface area for all the cases in Table 1. The no-motion case is also simulated, but only with the coarsest grid. The three grids are presented in Figure 7. The two coarsest grids, (Figure 7a,b are slightly stretched horizontally towards each tank head.

The interface area is supposed as important for the energy exchange between liquid and gas. It is difficult, if not impossible, to obtain it from experiments. To some extent, this is possible with CFD. The area prediction naturally depends on the grid refinement. A way to estimate such unknown variables is to perform a grid-independence study. This does not require us to compare with experimental data.

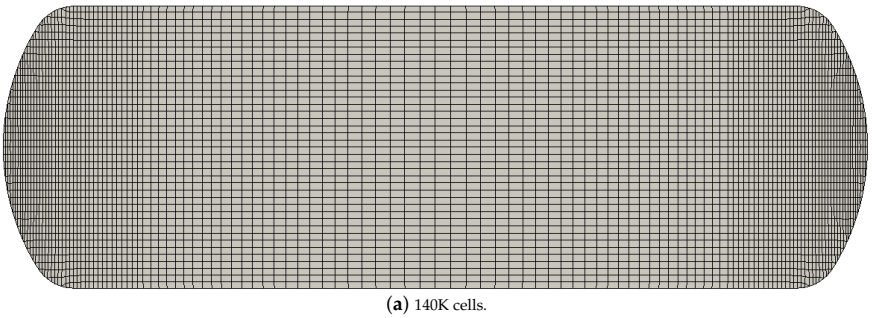

(**a**) 140K cells.

Figure 7. *Cont.*

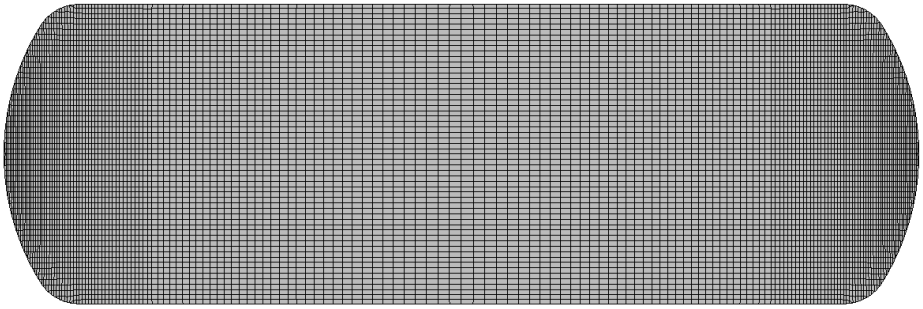

(**b**) 480K cells.

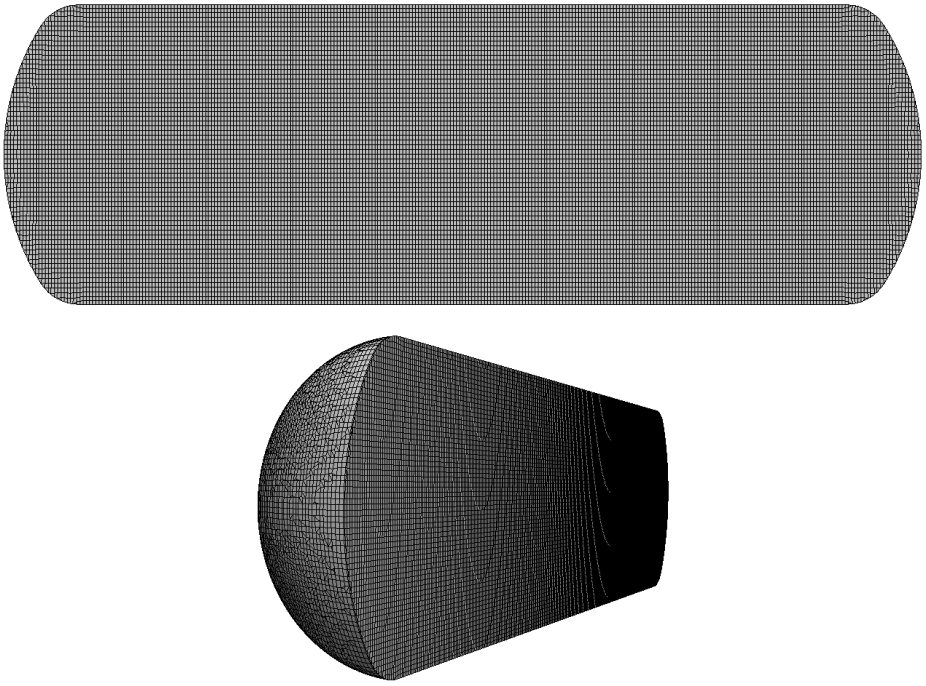

(**c**) 950K cells.

Figure 7. Different mesh used in simulations.

Cases 1–3 in Table 1 have been simulated on all three grids. Simulations have been performed computing on 40 nodes on the high-performance computing (HPC) cluster "Stallo" [35]. Some additional code was added directly into the *interDyMFoam* solver to obtain the area at each time step. The code is given in Appendix A.3. The code basically creates a volume field that equals the magnitude of the volume fraction gradient. The gradient is then integrated all over the domain.

The result is shown in Figure 8. Convergence is not achieved in the most severe sloshing case 3. Although some splashing is found in case 2, the free surface remains continuous most of the time. The jet is thus difficult to resolve with the grid. However, it is not only the peaks that occur every half a period that deviates. The time-averaged surface area is also quite different with each grid. The interface area is larger in case 3 than 1 and 2. However, the percentage increase of the area in cases

2 and 3 seems to be less than expected. The mean surface area in case 3 is approximately 15% larger compared to the undisturbed case for the finest grid.

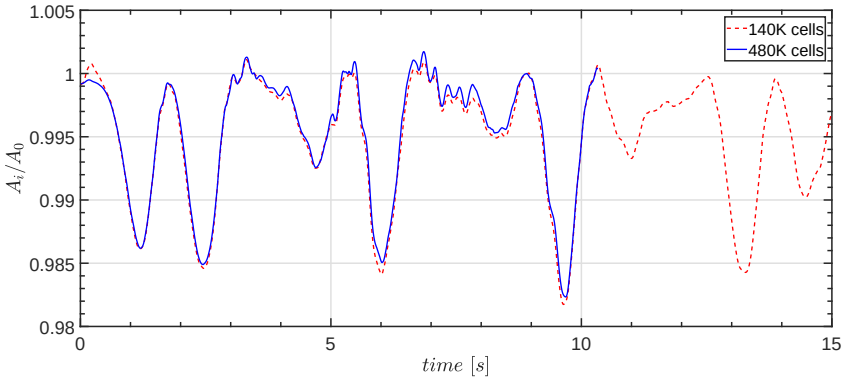

(a) Case 1 (small deformations).

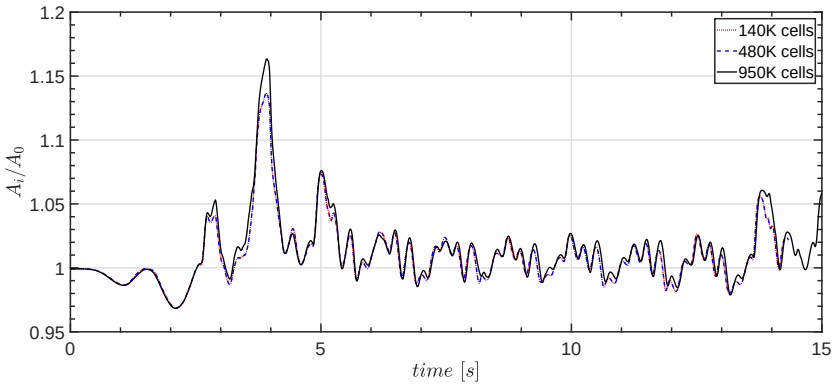

(b) Case 2 (oscillating waves).

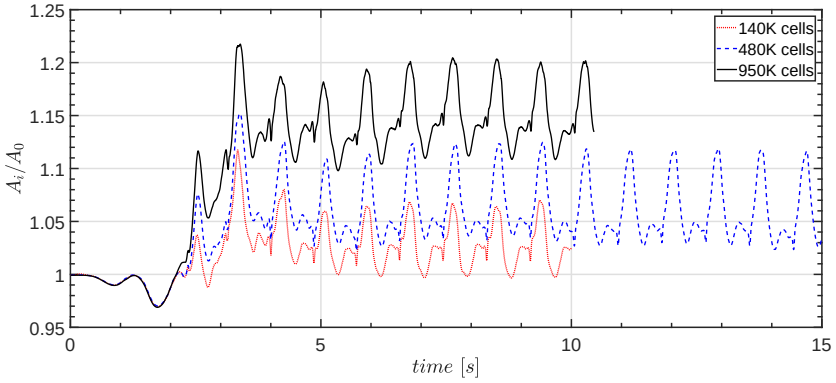

(c) Case 3 (jet).

Figure 8. Simulated interface area, A_i, divided by the undisturbed interface area, A_0, with different grids.

4.3. The Influence of the Liquid Jet

By taking a closer look at the pressure measurements from experiments in case 3 (Figure 9), one can see that the pressure consists of smaller periodic oscillations. This is most pronounced for case 3, but can be seen also in the other cases.

The mass condensation rate is proportional to $-dP/dt$, which can be calculated numerically from the measurements. Assuming that the gas volume is constant, and differentiating the ideal gas law, $pV = mRT$ gives:

$$\frac{dP}{dt} = -\frac{P}{m_G}\frac{dm_L}{dt} + \frac{P}{T_G}\frac{dT_G}{dt}, \tag{17}$$

where m_G is the mass of gas, T_G is the gas temperature and m_L is the mass of the liquid. It has been found by sensitivity studies that the change in gas temperature has a minor influence on the pressure because the gas temperature is nearly saturated. Hence, the last term may be excluded.

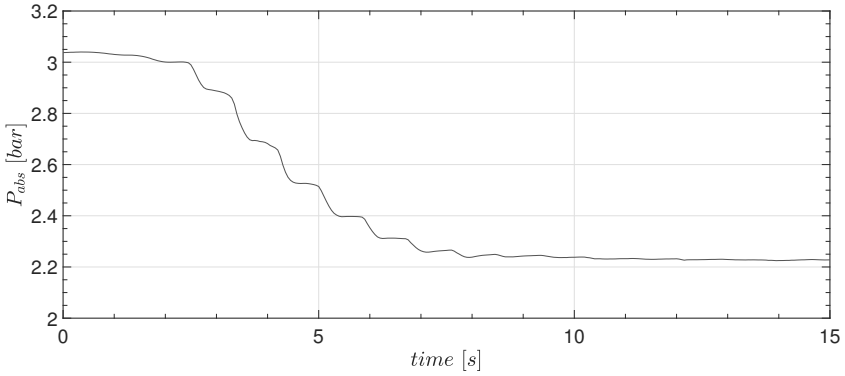

Figure 9. Absolute pressure in case 3 (jet).

The area found from the CFD calculations can be compared to the mass rate of change by normalizing the values and plot over time. The result is shown in Figure 10. The calculated maximum area from CFD is in phase with the maximum values of the mass condensation rate. Only a small phase shift is found in the beginning. As the temperature in proximity to the liquid surface raises, the condensation ceases. It is not sure whether the area increase itself is the only important factor here. From the figures, it is also observed that the jet impacts the surface at the time of the peak values. Another factor that might be important is the transport of cold liquid from the bulk, which is done efficiently with the jet. It also enhances the mixing between liquid and gas, as the gas is trapped between the jet and the liquid surface.

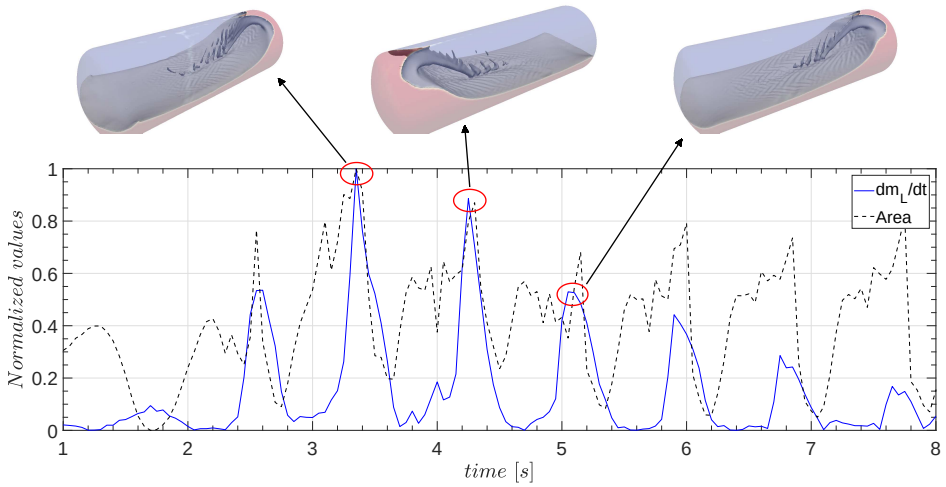

Figure 10. Correspondence of the interface area and condensation mass flux estimated from the measured pressure in case 3.

4.4. Prediction of Pressure and Temperature

Cases 0–3 have been simulated using the finest grid with 951×10^3 cells (Figure 7c). Figure 11 shows the comparison of pressure between CFD and experiments. The agreement is good in cases 2 and 3 (Figure 11b,c), while, in case 1 (Figure 11a), the pressure drop is over-predicted in the analysis. The discrepancy in case 1 may be explained by the fact that the temperature field is diffusive across the gas–liquid interface. Cases with severe sloshing may depend less on this unrealistic diffusion because the turbulence is much more pronounced and "camouflage" the error. This conclusion would require more in-depth studies. As may be observed, the pressure from CFD is slightly lower than the experiments in all cases. The reason is that the actual saturation temperature is slightly higher than the weighted average gas temperature. A prerequisite for the model to be realistic is that the gas is nearly saturated. The difference is irrelevant as the curves are parallel to each other, and the agreement is overall good.

Some plots of the temperature development in the tank are shown in Figure 12. In the column of figures to the left, contour plots of temperature are presented. The white line shows where the vertical profile at the right is plotted inside the tank. The first two Figure 12a,b is showing the wave just in an instant before the jet is formed along the wall. This is early in the sloshing event, and the temperature gradient is steep on both sides.

In the next two pairs of figures, the water hits the roof and the temperature profile is much more uniform. It is seen that the temperature above the interface is close to the initial interface temperature. The jet thus transports cold liquid quite efficiently towards the liquid surface.

In the last figure, the wave is heading towards the opposite end, and the the cooling of the gas is clearly visible from the first time (Figure 12b) to the last (Figure 12f). The gas bulk temperature has dropped four degrees during these few seconds. The results may explain why the pressure is dropping so efficiently close to resonance. The surface area might not be the dominating factor, but rather the transport of liquid bulk towards the surface. The jet enhances the mixing between liquid and gas quite efficiently.

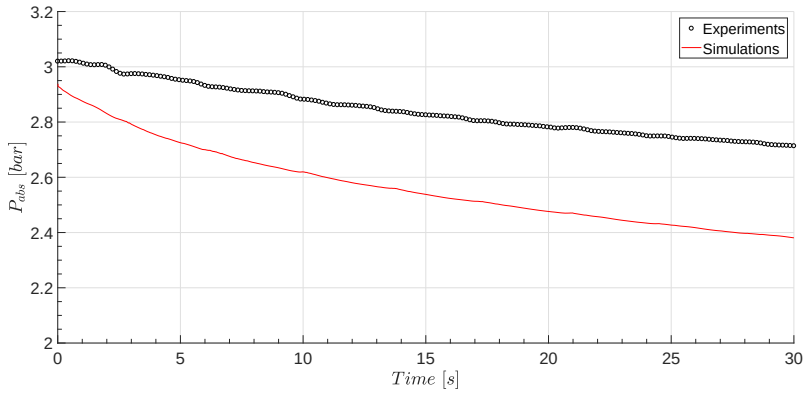

(a) Case 1 (small deformations).

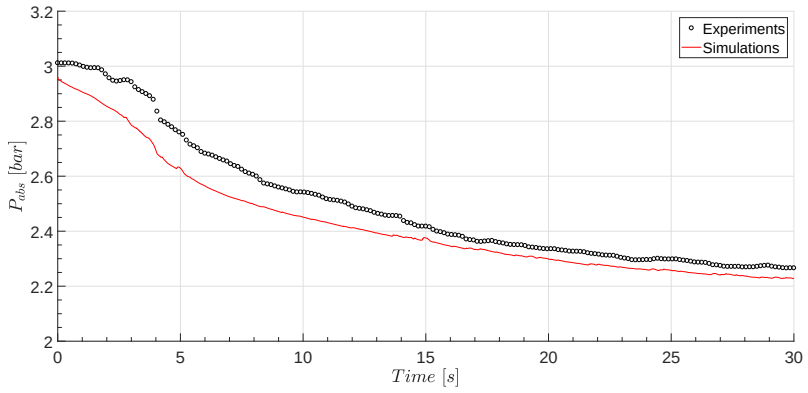

(b) Case 2 (oscillating waves).

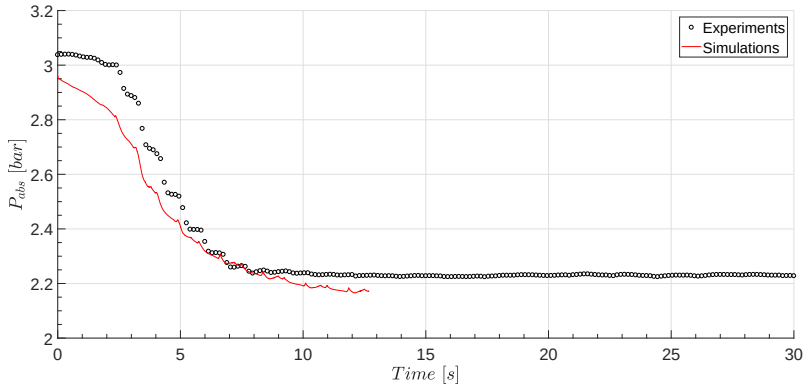

(c) Case 3 (jet).

Figure 11. Simulated pressure drop due to the enhanced thermal mixing in a sloshing tank.

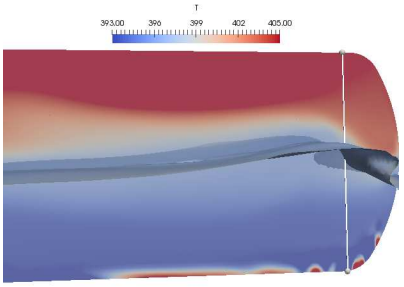

(**a**) Temperature contour at time 3.1 [s].

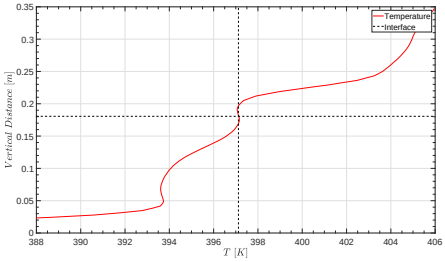

(**b**) Vertical line plot of temperature.

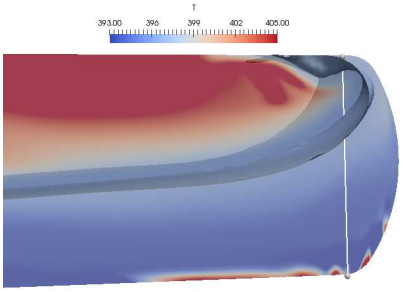

(**c**) Temperature contour at time 3.2 [s].

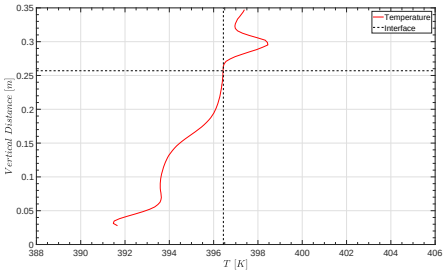

(**d**) Vertical line plot of temperature.

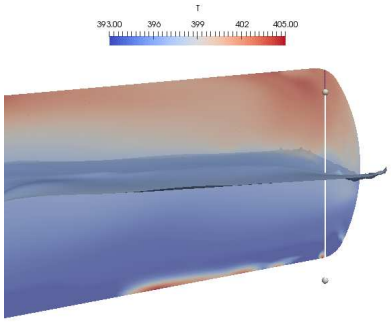

(**e**) Temperature contour at time 3.8 [s].

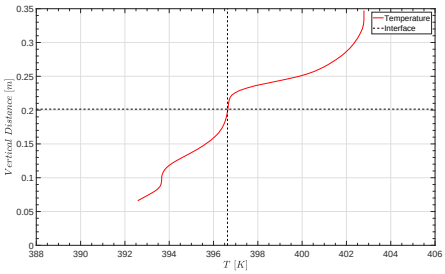

(**f**) Vertical line plot of temperature.

Figure 12. Simulated temperature profile in case number 3. The left column shows temperature contours at different time instants. To the right is the temperature profile along the white marked line inside the tank. The series shows the occurrence of a jet, where, in the last picture, the wave has left and is heading towards the opposite side of the tank. The gas temperature has dropped by 4 °C during these few seconds.

5. Discussion

Although the accuracy of the calculated interface area is quite uncertain for the jet case, the overall impression is that the area has less influence than what was expected. Case 2, which has a moderate pressure drop rate, and for which the area seems to be accurately determined, shows just a minor increase. However, it is pronounced in the beginning, while it ceases after a few seconds. The correspondence between the jet and the mass condensation rate given in Figure 10 still indicates that the area might be responsible for the large pressure drop. Another factor that is likely to be important is the transportation of cold bulk onto the interface area that takes place in a jet event. This was found to be important as shown in the last part of the previous section. If this is the case, it is understandable why the resonant cases results in the enhanced thermal response. It tells us that breaking waves results in rapid loss of pressure.

To estimate the maximum area expected in sloshing, an exercise is performed where the surface area of a liquid drop of a certain diameter equivalent to a percentage liquid volume is calculated. The result in Table 3 give the overall surface area if 10% of the total liquid volume contains the equivalent number of particles of a specified diameter of 1 cm.

The estimated area from CFD is uncertain in case 3 where drops may be expected, and the area may be much greater as seen from Table 3. The free surface in case 2 does not break. It is therefore difficult to tell from the calculated area value if this has a significant effect on heat transfer or not. It is most likely to be a combination of the local heat transfer mechanisms and the bulk mixing. Both are contributing, but the time scales are quite different.

Table 3. Surface area for a number of liquid drops of 1 [cm] diameter equivalent to a percentage of the total liquid volume in the tank. Space between the drops are excluded. The undisturbed surface area is the same as in the large tank, equal to $A_0 = 0.365$ m^2.

% Liquid Volume	Volume [L]	N Drops	Surface Area (m^2) Drops	A_i/A_0
1.0	0.48	907	0.29	0.78
2.5	1.19	2268	0.71	1.95
5.0	2.38	4536	1.43	3.90
10.0	4.75	9072	2.85	7.81
15.0	7.13	13,608	4.28	11.71
20.0	9.50	18,144	5.70	15.62

6. Conclusions

Numerical simulations of sloshing both considering sloshing hydrodynamics as well as thermal mixing have been performed. The tool used is OpenFOAM, and an existing solver was modified to include a transport equation for thermal energy. Simulations with three different excitation frequencies have been performed with 50% filling in the tank. The interface area was calculated with three different grids and compared. Comparison was also made between the calculations and experimental results. The pressure drop from simulations was compared to experimental results in the last part of the paper. The thermal mixing was studied as well.

The following conclusions can be made considering the aforementioned studies:

- The grid independence study indicates that the area can be estimated when the free surface does not break. Grid convergence was not found in case 3.
- The increase of the interface area is approximately 2.5% in case 2 when the sloshing is closer to a quasi-steady condition.
- The interface area is not accurately determined in case 3, but the results indicate that the area is larger than in case 2, but may be less than an increase of 50% relative to the undisturbed area.
- The pressure measurement in case 3 shows correspondence with the sloshing hydrodynamics, and the occurrence of the jet clearly influences the pressure drop.

- Results from simulations with the extended OpenFOAM solver shows acceptable agreement with the measured pressure, and may be used for further investigation. However, it is quite uncertain to what extent the model is applicable for other cases with other components, initial conditions, etc.

Further work must be conducted where the area is calculated with grids of different resolution. Comparison with experimental data should be investigated. The CFD model shows potential, but must be improved further. More detailed development work on CFD and direct-contact heat transfer problems should also be done.

Acknowledgments: The authors would like to thank the staff at the Department of Ocean Operations and Civil Engineering for providing lab facilities and materials necessary for performing the experiments. Thanks to the staff at Notur/Sigma2 for support with the HPC clusters. Implementations in OpenFOAM would not have been possible without the course taught by Håkan Nilsson at Chalmers University in Gothenburg, Sweden and the many tutorials prepared at Chalmers. This open access publication is founded by the publication fund of NTNU.

Author Contributions: The main author of the paper is Erlend Liavåg Grotle. Vilmar Æsøy is a supervisor and has contributed to the paper by reading and correcting.

Conflicts of Interest: The authors declare no conflict of interest.

Appendix A. OpenFOAM Code Snippets

Appendix A.1. Weighted Average of the Gas Temperature

```
Tsat = sum((scalar(1)-alpha1)*T)/sum(scalar(1)-alpha1);
```

Appendix A.2. Energy Transport Equation

```
fvScalarMatrix TEqn
(
    fvm::ddt(rho,T)
  +fvm::div(rhoPhi,T)
  -fvm::laplacian(kappaF/cp,T)
  ==
    fvm::Su(alpha1*(scalar(1)-alpha1)*rho*evap*Tsat, T)
  +fvm::Sp(-alpha1*(scalar(1)-alpha1)*rho*evap, T)
);
TEqn.solve()
```

Appendix A.3. Code to Calculate the Interface Area

```
volScalarField gradGamma = mag(fvc::grad(alpha1));
dimensionedScalar totalSurfaceArea = fvc::domainIntegrate(gradGamma);
```

References

1. Æsøy, V.; Stenersen, D. Low emission LNG fuelled ships for environmental friendly operations in arctic areas. In Proceedings of the ASME 2013 32nd International Conference on Ocean, Offshore and Arctic Engineering, Nantes, France, 9–14 June 2013; p. V006T07A028.
2. Faltinsen, O.M.; Timokha, A.N. *Sloshing*; Cambridge University Press: Cambridge, UK, 2009.
3. Æsøy, V.; Einang, P.M.; Stenersen, D.; Hennie, E.; Valberg, I. LNG-fuelled engines and fuel systems for medium-speed engines in maritime applications. *SAE Tech. Paper* **2011**, doi:10.4271/2011-01-1998.
4. Grotle, E.; Æsøy, V.; Pedersen, E. Modelling of LNG fuel systems for simulations of transient operations. In *Maritime-Port Technology and Development*; CRC Press: Cleveland, OH, USA, 2014; p. 205.
5. Lemmon, E.W.; Huber, M.L.; McLinden, M.O. *NIST Standard Reference Database 23: Reference Fluid Thermodynamic and Transport Properties-REFPROP*, version 9.1; National Institute of Standards and Technology: Gaithersburg, MD, USA, 2013.

6. Grotle, E.L.; Halse, K.H.; Pedersen, E.; Li, Y. Non-Isothermal Sloshing in Marine Liquefied Natural Gas Fuel Tanks. In Proceedings of the 26th International Ocean and Polar Engineering Conference, Rhodes, Greece, 26 June–1 July 2016; International Society of Offshore and Polar Engineers: Mountain View, CA, USA, 2016.
7. Moran, M.E.; Mcnelis, N.B.; Kudlac, M.T.; Haberbusch, M.S.; Satornino, G.A. Experimental results of hydrogen slosh in a 62 cubic foot (1750 liter) tank. In Proceedings of the 30th Joint Propulsion Conference, Indianapolis, IN, USA, 27–29 June 1994.
8. Lacapere, J.; Vieille, B.; Legrand, B. Experimental and numerical results of sloshing with cryogenic fluids. Progress in Propulsion Physics. *EDP Sci.* **2009**, *1*, 267–278.
9. Arndt, T. *Sloshing of Cryogenic Liquids in a Cylindrical Tank under Normal Gravity Conditions*; Universtität Bremen: Bremen, Germany, 2011.
10. Ludwig, C.; Dreyer, M.; Hopfinger, E. Pressure variations in a cryogenic liquid storage tank subjected to periodic excitations. *Int. J. Heat Mass Transf.* **2013**, *66*, 223–234.
11. Lin, C.S.; Hasan, M.; Nyland, T. Mixing and transient interface condensation of a liquid hydrogen tank. In Proceedings of the 29th Joint Propulsion Conference and Exhibit, Monterey, CA, USA, 28–30 June 1993.
12. Juric, D.; Tryggvason, G. Computations of boiling flows. *Int. J. Multiph. Flow* **1998**, *24*, 387–410.
13. Welch, S.W.; Wilson, J. A volume of fluid based method for fluid flows with phase change. *J. Comput. Phys.* **2000**, *160*, 662–682.
14. Youngs, D.L. Time-dependent multi-material flow with large fluid distortion. In *Numerical Methods for Fluid Dynamics*; Academic Press: Cambridge, MA, USA, 1982.
15. Hardt, S.; Wondra, F. Evaporation model for interfacial flows based on a continuum-field representation of the source terms. *J. Comput. Phys.* **2008**, *227*, 5871–5895.
16. Gibou, F.; Chen, L.; Nguyen, D.; Banerjee, S. A level set based sharp interface method for the multiphase incompressible Navier–Stokes equations with phase change. *J. Comput. Phys.* **2007**, *222*, 536–555.
17. Liu, Z.; Li, Y.; Jin, Y. Pressurization performance and temperature stratification in cryogenic final stage propellant tank. *Appl. Therm. Eng.* **2016**, *106*, 211–220.
18. Liu, Z.; Li, Y.; Jin, Y.; Li, C. Thermodynamic performance of pre-pressurization in a cryogenic tank. *Appl. Therm. Eng.* **2017**, *112*, 801–810.
19. Haider, J. Numerical Modelling of Evaporation and Condensation Phenomena-Numerische Modellierung von Verdampfungs-und Kondensationsphänomenen. Ph.D. Thesis, Universität Stuttgart, Stuttgart, Germany, 2013.
20. Kunkelmann, C. Numerical Modeling and Investigation of Boiling Phenomena. Ph.D. Thesis, Technische Universität, Munich, Germany, 2011.
21. Georgoulas, A.; Andredaki, M.; Marengo, M. An Enhanced VOF Method Coupled with Heat Transfer and Phase Change to Characterise Bubble Detachment in Saturated Pool Boiling. *Energies* **2017**, *10*, 272.
22. Maillard, S.; Brosset, L. Influence of DR Between Liquid and Gas on Sloshing Model Test Results. *Int. J. Offshore Polar Eng.* **2009**, *19*, 167–175.
23. Moukalled, F.; Mangani, L.; Darwish, M. *The Finite Volume Method in Computational Fluid Dynamics: An Advanced Introduction with OpenFOAM® and Matlab*; Springer: Berlin, Germany, 2015.
24. Menter, F.R. Two-equation eddy-viscosity turbulence models for engineering applications. *AIAA J.* **1994**, *32*, 1598–1605.
25. Menter, F.R.; Esch, T. Elements of Industrial Heat Transfer Prediction. In Proceedings of the 16th Brazilian Congress of Mechanical Engineering (COBEM), Minas Gerais, Brazil, 26–30 November 2001.
26. Menter, F.; Kuntz, M.; Langtry, R. Ten years of industrial experience with the SST turbulence model. *Turbul. Heat Mass Trans.* **2003**, *4*, 625–632.
27. The OpenFOAM Foundation Ltd. kOmegaSSTBase.H File Reference. 2017. Available online: https://cpp.openfoam.org/v5/classFoam_1_1kOmegaSST.html#details (accessed on 27 August 2017).
28. Menter, F.R.; Carregal Ferreira, J.; Esch, T.; Konno, B. The SST Turbulence Model with Improved Wall Treatment for Heat Transfer Predictions in Gas Turbines. In Proceedings of the International Gas Turbine Congress, Tokyo, Japan, 2–7 November 2003.
29. Rusche, H. Computational Fluid Dynamics of Dispersed Two-Phase Flows at High Phase Fractions. Ph.D. Thesis, Imperial College London (University of London), London, UK, 2003.
30. Murray, F.W. *On the Computation of Saturation Vapor Pressure*; American Meteorological Society: Boston, MA, USA, 1966.

31. Greenshields, C. *OpenFOAM User Guide*, version 4.0; OpenFOAM Foundation Ltd.: London, UK, 2016.
32. Issa, R.I. Solution of the implicitly discretised fluid flow equations by operator-splitting. *J. Comput. Phys.* **1986**, *62*, 40–65.
33. Rhie, C.; Chow, W. Numerical study of the turbulent flow past an airfoil with trailing edge separation. *AIAA J.* **1983**, *21*, 1525–1532.
34. Kärrholm, F.P. *Rhie-Chow Interpolation in Openfoam*; Department of Applied Mechanics, Chalmers University of Technology: Goteborg, Sweden, 2006.
35. Stallo. 2017. Available online: https://www.sigma2.no/content/stallo (accessed on 14 August 2017).

Appendix B

Previous PhD thesis at NTNU MT

Previous PhD theses published at the Departement of Marine Technology
(earlier: Faculty of Marine Technology)
NORWEGIAN UNIVERSITY OF SCIENCE AND TECHNOLOGY

Report No.	Author	Title
	Kavlie, Dag	Optimization of Plane Elastic Grillages, 1967
	Hansen, Hans R.	Man-Machine Communication and Data-Storage Methods in Ship Structural Design, 1971
	Gisvold, Kaare M.	A Method for non-linear mixed -integer programming and its Application to Design Problems, 1971
	Lund, Sverre	Tanker Frame Optimalization by means of SUMT-Transformation and Behaviour Models, 1971
	Vinje, Tor	On Vibration of Spherical Shells Interacting with Fluid, 1972
	Lorentz, Jan D.	Tank Arrangement for Crude Oil Carriers in Accordance with the new Anti-Pollution Regulations, 1975
	Carlsen, Carl A.	Computer-Aided Design of Tanker Structures, 1975
	Larsen, Carl M.	Static and Dynamic Analysis of Offshore Pipelines during Installation, 1976
UR-79-01	Brigt Hatlestad, MK	The finite element method used in a fatigue evaluation of fixed offshore platforms. (Dr.Ing. Thesis)
UR-79-02	Erik Pettersen, MK	Analysis and design of cellular structures. (Dr.Ing. Thesis)
UR-79-03	Sverre Valsgård, MK	Finite difference and finite element methods applied to nonlinear analysis of plated structures. (Dr.Ing. Thesis)
UR-79-04	Nils T. Nordsve, MK	Finite element collapse analysis of structural members considering imperfections and stresses due to fabrication. (Dr.Ing. Thesis)
UR-79-05	Ivar J. Fylling, MK	Analysis of towline forces in ocean towing systems. (Dr.Ing. Thesis)
UR-80-06	Nils Sandsmark, MM	Analysis of Stationary and Transient Heat Conduction by the Use of the Finite Element Method. (Dr.Ing. Thesis)
UR-80-09	Sverre Haver, MK	Analysis of uncertainties related to the stochastic modeling of ocean waves. (Dr.Ing. Thesis)
UR-81-15	Odland, Jonas	On the Strength of welded Ring stiffened cylindrical Shells primarily subjected to axial Compression
UR-82-17	Engesvik, Knut	Analysis of Uncertainties in the fatigue Capacity of

		Welded Joints
UR-82-18	Rye, Henrik	Ocean wave groups
UR-83-30	Eide, Oddvar Inge	On Cumulative Fatigue Damage in Steel Welded Joints
UR-83-33	Mo, Olav	Stochastic Time Domain Analysis of Slender Offshore Structures
UR-83-34	Amdahl, Jørgen	Energy absorption in Ship-platform impacts
UR-84-37	Mørch, Morten	Motions and mooring forces of semi submersibles as determined by full-scale measurements and theoretical analysis
UR-84-38	Soares, C. Guedes	Probabilistic models for load effects in ship structures
UR-84-39	Aarsnes, Jan V.	Current forces on ships
UR-84-40	Czujko, Jerzy	Collapse Analysis of Plates subjected to Biaxial Compression and Lateral Load
UR-85-46	Alf G. Engseth, MK	Finite element collapse analysis of tubular steel offshore structures. (Dr.Ing. Thesis)
UR-86-47	Dengody Sheshappa, MP	A Computer Design Model for Optimizing Fishing Vessel Designs Based on Techno-Economic Analysis. (Dr.Ing. Thesis)
UR-86-48	Vidar Aanesland, MH	A Theoretical and Numerical Study of Ship Wave Resistance. (Dr.Ing. Thesis)
UR-86-49	Heinz-Joachim Wessel, MK	Fracture Mechanics Analysis of Crack Growth in Plate Girders. (Dr.Ing. Thesis)
UR-86-50	Jon Taby, MK	Ultimate and Post-ultimate Strength of Dented Tubular Members. (Dr.Ing. Thesis)
UR-86-51	Walter Lian, MH	A Numerical Study of Two-Dimensional Separated Flow Past Bluff Bodies at Moderate KC-Numbers. (Dr.Ing. Thesis)
UR-86-52	Bjørn Sortland, MH	Force Measurements in Oscillating Flow on Ship Sections and Circular Cylinders in a U-Tube Water Tank. (Dr.Ing. Thesis)
UR-86-53	Kurt Strand, MM	A System Dynamic Approach to One-dimensional Fluid Flow. (Dr.Ing. Thesis)
UR-86-54	Arne Edvin Løken, MH	Three Dimensional Second Order Hydrodynamic Effects on Ocean Structures in Waves. (Dr.Ing. Thesis)
UR-86-55	Sigurd Falch, MH	A Numerical Study of Slamming of Two-Dimensional Bodies. (Dr.Ing. Thesis)
UR-87-56	Arne Braathen, MH	Application of a Vortex Tracking Method to the Prediction of Roll Damping of a Two-Dimension Floating Body. (Dr.Ing. Thesis)

UR-87-57	Bernt Leira, MK	Gaussian Vector Processes for Reliability Analysis involving Wave-Induced Load Effects. (Dr.Ing. Thesis)
UR-87-58	Magnus Småvik, MM	Thermal Load and Process Characteristics in a Two-Stroke Diesel Engine with Thermal Barriers (in Norwegian). (Dr.Ing. Thesis)
MTA-88-59	Bernt Arild Bremdal, MP	An Investigation of Marine Installation Processes – A Knowledge - Based Planning Approach. (Dr.Ing. Thesis)
MTA-88-60	Xu Jun, MK	Non-linear Dynamic Analysis of Space-framed Offshore Structures. (Dr.Ing. Thesis)
MTA-89-61	Gang Miao, MH	Hydrodynamic Forces and Dynamic Responses of Circular Cylinders in Wave Zones. (Dr.Ing. Thesis)
MTA-89-62	Martin Greenhow, MH	Linear and Non-Linear Studies of Waves and Floating Bodies. Part I and Part II. (Dr.Techn. Thesis)
MTA-89-63	Chang Li, MH	Force Coefficients of Spheres and Cubes in Oscillatory Flow with and without Current. (Dr.Ing. Thesis
MTA-89-64	Hu Ying, MP	A Study of Marketing and Design in Development of Marine Transport Systems. (Dr.Ing. Thesis)
MTA-89-65	Arild Jæger, MH	Seakeeping, Dynamic Stability and Performance of a Wedge Shaped Planing Hull. (Dr.Ing. Thesis)
MTA-89-66	Chan Siu Hung, MM	The dynamic characteristics of tilting-pad bearings
MTA-89-67	Kim Wikstrøm, MP	Analysis av projekteringen for ett offshore projekt. (Licenciat-avhandling)
MTA-89-68	Jiao Guoyang, MK	Reliability Analysis of Crack Growth under Random Loading, considering Model Updating. (Dr.Ing. Thesis)
MTA-89-69	Arnt Olufsen, MK	Uncertainty and Reliability Analysis of Fixed Offshore Structures. (Dr.Ing. Thesis)
MTA-89-70	Wu Yu-Lin, MR	System Reliability Analyses of Offshore Structures using improved Truss and Beam Models. (Dr.Ing. Thesis)
MTA-90-71	Jan Roger Hoff, MH	Three-dimensional Green function of a vessel with forward speed in waves. (Dr.Ing. Thesis)
MTA-90-72	Rong Zhao, MH	Slow-Drift Motions of a Moored Two-Dimensional Body in Irregular Waves. (Dr.Ing. Thesis)
MTA-90-73	Atle Minsaas, MP	Economical Risk Analysis. (Dr.Ing. Thesis)
MTA-90-74	Knut-Aril Farnes, MK	Long-term Statistics of Response in Non-linear Marine Structures. (Dr.Ing. Thesis)
MTA-90-75	Torbjørn Sotberg, MK	Application of Reliability Methods for Safety Assessment of Submarine Pipelines. (Dr.Ing.

		Thesis)
MTA-90-76	Zeuthen, Steffen, MP	SEAMAID. A computational model of the design process in a constraint-based logic programming environment. An example from the offshore domain. (Dr.Ing. Thesis)
MTA-91-77	Haagensen, Sven, MM	Fuel Dependant Cyclic Variability in a Spark Ignition Engine - An Optical Approach. (Dr.Ing. Thesis)
MTA-91-78	Løland, Geir, MH	Current forces on and flow through fish farms. (Dr.Ing. Thesis)
MTA-91-79	Hoen, Christopher, MK	System Identification of Structures Excited by Stochastic Load Processes. (Dr.Ing. Thesis)
MTA-91-80	Haugen, Stein, MK	Probabilistic Evaluation of Frequency of Collision between Ships and Offshore Platforms. (Dr.Ing. Thesis)
MTA-91-81	Sødahl, Nils, MK	Methods for Design and Analysis of Flexible Risers. (Dr.Ing. Thesis)
MTA-91-82	Ormberg, Harald, MK	Non-linear Response Analysis of Floating Fish Farm Systems. (Dr.Ing. Thesis)
MTA-91-83	Marley, Mark J., MK	Time Variant Reliability under Fatigue Degradation. (Dr.Ing. Thesis)
MTA-91-84	Krokstad, Jørgen R., MH	Second-order Loads in Multidirectional Seas. (Dr.Ing. Thesis)
MTA-91-85	Molteberg, Gunnar A., MM	The Application of System Identification Techniques to Performance Monitoring of Four Stroke Turbocharged Diesel Engines. (Dr.Ing. Thesis)
MTA-92-86	Mørch, Hans Jørgen Bjelke, MH	Aspects of Hydrofoil Design: with Emphasis on Hydrofoil Interaction in Calm Water. (Dr.Ing. Thesis)
MTA-92-87	Chan Siu Hung, MM	Nonlinear Analysis of Rotordynamic Instabilities in Highspeed Turbomachinery. (Dr.Ing. Thesis)
MTA-92-88	Bessason, Bjarni, MK	Assessment of Earthquake Loading and Response of Seismically Isolated Bridges. (Dr.Ing. Thesis)
MTA-92-89	Langli, Geir, MP	Improving Operational Safety through exploitation of Design Knowledge - an investigation of offshore platform safety. (Dr.Ing. Thesis)
MTA-92-90	Sævik, Svein, MK	On Stresses and Fatigue in Flexible Pipes. (Dr.Ing. Thesis)
MTA-92-91	Ask, Tor Ø., MM	Ignition and Flame Growth in Lean Gas-Air Mixtures. An Experimental Study with a Schlieren System. (Dr.Ing. Thesis)
MTA-86-92	Hessen, Gunnar, MK	Fracture Mechanics Analysis of Stiffened Tubular Members. (Dr.Ing. Thesis)

MTA-93-93	Steinebach, Christian, MM	Knowledge Based Systems for Diagnosis of Rotating Machinery. (Dr.Ing. Thesis)
MTA-93-94	Dalane, Jan Inge, MK	System Reliability in Design and Maintenance of Fixed Offshore Structures. (Dr.Ing. Thesis)
MTA-93-95	Steen, Sverre, MH	Cobblestone Effect on SES. (Dr.Ing. Thesis)
MTA-93-96	Karunakaran, Daniel, MK	Nonlinear Dynamic Response and Reliability Analysis of Drag-dominated Offshore Platforms. (Dr.Ing. Thesis)
MTA-93-97	Hagen, Arnulf, MP	The Framework of a Design Process Language. (Dr.Ing. Thesis)
MTA-93-98	Nordrik, Rune, MM	Investigation of Spark Ignition and Autoignition in Methane and Air Using Computational Fluid Dynamics and Chemical Reaction Kinetics. A Numerical Study of Ignition Processes in Internal Combustion Engines. (Dr.Ing. Thesis)
MTA-94-99	Passano, Elizabeth, MK	Efficient Analysis of Nonlinear Slender Marine Structures. (Dr.Ing. Thesis)
MTA-94-100	Kvålsvold, Jan, MH	Hydroelastic Modelling of Wetdeck Slamming on Multihull Vessels. (Dr.Ing. Thesis)
MTA-94-102	Bech, Sidsel M., MK	Experimental and Numerical Determination of Stiffness and Strength of GRP/PVC Sandwich Structures. (Dr.Ing. Thesis)
MTA-95-103	Paulsen, Hallvard, MM	A Study of Transient Jet and Spray using a Schlieren Method and Digital Image Processing. (Dr.Ing. Thesis)
MTA-95-104	Hovde, Geir Olav, MK	Fatigue and Overload Reliability of Offshore Structural Systems, Considering the Effect of Inspection and Repair. (Dr.Ing. Thesis)
MTA-95-105	Wang, Xiaozhi, MK	Reliability Analysis of Production Ships with Emphasis on Load Combination and Ultimate Strength. (Dr.Ing. Thesis)
MTA-95-106	Ulstein, Tore, MH	Nonlinear Effects of a Flexible Stern Seal Bag on Cobblestone Oscillations of an SES. (Dr.Ing. Thesis)
MTA-95-107	Solaas, Frøydis, MH	Analytical and Numerical Studies of Sloshing in Tanks. (Dr.Ing. Thesis)
MTA-95-108	Hellan, Øyvind, MK	Nonlinear Pushover and Cyclic Analyses in Ultimate Limit State Design and Reassessment of Tubular Steel Offshore Structures. (Dr.Ing. Thesis)
MTA-95-109	Hermundstad, Ole A., MK	Theoretical and Experimental Hydroelastic Analysis of High Speed Vessels. (Dr.Ing. Thesis)
MTA-96-110	Bratland, Anne K., MH	Wave-Current Interaction Effects on Large-Volume Bodies in Water of Finite Depth. (Dr.Ing. Thesis)
MTA-96-111	Herfjord, Kjell, MH	A Study of Two-dimensional Separated Flow by a Combination of the Finite Element Method and

		Navier-Stokes Equations. (Dr.Ing. Thesis)
MTA-96-112	Æsøy, Vilmar, MM	Hot Surface Assisted Compression Ignition in a Direct Injection Natural Gas Engine. (Dr.Ing. Thesis)
MTA-96-113	Eknes, Monika L., MK	Escalation Scenarios Initiated by Gas Explosions on Offshore Installations. (Dr.Ing. Thesis)
MTA-96-114	Erikstad, Stein O., MP	A Decision Support Model for Preliminary Ship Design. (Dr.Ing. Thesis)
MTA-96-115	Pedersen, Egil, MH	A Nautical Study of Towed Marine Seismic Streamer Cable Configurations. (Dr.Ing. Thesis)
MTA-97-116	Moksnes, Paul O., MM	Modelling Two-Phase Thermo-Fluid Systems Using Bond Graphs. (Dr.Ing. Thesis)
MTA-97-117	Halse, Karl H., MK	On Vortex Shedding and Prediction of Vortex-Induced Vibrations of Circular Cylinders. (Dr.Ing. Thesis)
MTA-97-118	Igland, Ragnar T., MK	Reliability Analysis of Pipelines during Laying, considering Ultimate Strength under Combined Loads. (Dr.Ing. Thesis)
MTA-97-119	Pedersen, Hans-P., MP	Levendefiskteknologi for fiskefartøy. (Dr.Ing. Thesis)
MTA-98-120	Vikestad, Kyrre, MK	Multi-Frequency Response of a Cylinder Subjected to Vortex Shedding and Support Motions. (Dr.Ing. Thesis)
MTA-98-121	Azadi, Mohammad R. E., MK	Analysis of Static and Dynamic Pile-Soil-Jacket Behaviour. (Dr.Ing. Thesis)
MTA-98-122	Ulltang, Terje, MP	A Communication Model for Product Information. (Dr.Ing. Thesis)
MTA-98-123	Torbergsen, Erik, MM	Impeller/Diffuser Interaction Forces in Centrifugal Pumps. (Dr.Ing. Thesis)
MTA-98-124	Hansen, Edmond, MH	A Discrete Element Model to Study Marginal Ice Zone Dynamics and the Behaviour of Vessels Moored in Broken Ice. (Dr.Ing. Thesis)
MTA-98-125	Videiro, Paulo M., MK	Reliability Based Design of Marine Structures. (Dr.Ing. Thesis)
MTA-99-126	Mainçon, Philippe, MK	Fatigue Reliability of Long Welds Application to Titanium Risers. (Dr.Ing. Thesis)
MTA-99-127	Haugen, Elin M., MH	Hydroelastic Analysis of Slamming on Stiffened Plates with Application to Catamaran Wetdecks. (Dr.Ing. Thesis)
MTA-99-128	Langhelle, Nina K., MK	Experimental Validation and Calibration of Nonlinear Finite Element Models for Use in Design of Aluminium Structures Exposed to Fire. (Dr.Ing. Thesis)
MTA-99-	Berstad, Are J., MK	Calculation of Fatigue Damage in Ship Structures.

129		(Dr.Ing. Thesis)
MTA-99-130	Andersen, Trond M., MM	Short Term Maintenance Planning. (Dr.Ing. Thesis)
MTA-99-131	Tveiten, Bård Wathne, MK	Fatigue Assessment of Welded Aluminium Ship Details. (Dr.Ing. Thesis)
MTA-99-132	Søreide, Fredrik, MP	Applications of underwater technology in deep water archaeology. Principles and practice. (Dr.Ing. Thesis)
MTA-99-133	Tønnessen, Rune, MH	A Finite Element Method Applied to Unsteady Viscous Flow Around 2D Blunt Bodies With Sharp Corners. (Dr.Ing. Thesis)
MTA-99-134	Elvekrok, Dag R., MP	Engineering Integration in Field Development Projects in the Norwegian Oil and Gas Industry. The Supplier Management of Norne. (Dr.Ing. Thesis)
MTA-99-135	Fagerholt, Kjetil, MP	Optimeringsbaserte Metoder for Ruteplanlegging innen skipsfart. (Dr.Ing. Thesis)
MTA-99-136	Bysveen, Marie, MM	Visualization in Two Directions on a Dynamic Combustion Rig for Studies of Fuel Quality. (Dr.Ing. Thesis)
MTA-2000-137	Storteig, Eskild, MM	Dynamic characteristics and leakage performance of liquid annular seals in centrifugal pumps. (Dr.Ing. Thesis)
MTA-2000-138	Sagli, Gro, MK	Model uncertainty and simplified estimates of long term extremes of hull girder loads in ships. (Dr.Ing. Thesis)
MTA-2000-139	Tronstad, Harald, MK	Nonlinear analysis and design of cable net structures like fishing gear based on the finite element method. (Dr.Ing. Thesis)
MTA-2000-140	Kroneberg, André, MP	Innovation in shipping by using scenarios. (Dr.Ing. Thesis)
MTA-2000-141	Haslum, Herbjørn Alf, MH	Simplified methods applied to nonlinear motion of spar platforms. (Dr.Ing. Thesis)
MTA-2001-142	Samdal, Ole Johan, MM	Modelling of Degradation Mechanisms and Stressor Interaction on Static Mechanical Equipment Residual Lifetime. (Dr.Ing. Thesis)
MTA-2001-143	Baarholm, Rolf Jarle, MH	Theoretical and experimental studies of wave impact underneath decks of offshore platforms. (Dr.Ing. Thesis)
MTA-2001-144	Wang, Lihua, MK	Probabilistic Analysis of Nonlinear Wave-induced Loads on Ships. (Dr.Ing. Thesis)
MTA-2001-145	Kristensen, Odd H. Holt, MK	Ultimate Capacity of Aluminium Plates under Multiple Loads, Considering HAZ Properties. (Dr.Ing. Thesis)
MTA-2001-146	Greco, Marilena, MH	A Two-Dimensional Study of Green-Water

		Loading. (Dr.Ing. Thesis)
MTA-2001-147	Heggelund, Svein E., MK	Calculation of Global Design Loads and Load Effects in Large High Speed Catamarans. (Dr.Ing. Thesis)
MTA-2001-148	Babalola, Olusegun T., MK	Fatigue Strength of Titanium Risers – Defect Sensitivity. (Dr.Ing. Thesis)
MTA-2001-149	Mohammed, Abuu K., MK	Nonlinear Shell Finite Elements for Ultimate Strength and Collapse Analysis of Ship Structures. (Dr.Ing. Thesis)
MTA-2002-150	Holmedal, Lars E., MH	Wave-current interactions in the vicinity of the sea bed. (Dr.Ing. Thesis)
MTA-2002-151	Rognebakke, Olav F., MH	Sloshing in rectangular tanks and interaction with ship motions. (Dr.Ing. Thesis)
MTA-2002-152	Lader, Pål Furset, MH	Geometry and Kinematics of Breaking Waves. (Dr.Ing. Thesis)
MTA-2002-153	Yang, Qinzheng, MH	Wash and wave resistance of ships in finite water depth. (Dr.Ing. Thesis)
MTA-2002-154	Melhus, Øyvin, MM	Utilization of VOC in Diesel Engines. Ignition and combustion of VOC released by crude oil tankers. (Dr.Ing. Thesis)
MTA-2002-155	Ronæss, Marit, MH	Wave Induced Motions of Two Ships Advancing on Parallel Course. (Dr.Ing. Thesis)
MTA-2002-156	Økland, Ole D., MK	Numerical and experimental investigation of whipping in twin hull vessels exposed to severe wet deck slamming. (Dr.Ing. Thesis)
MTA-2002-157	Ge, Chunhua, MK	Global Hydroelastic Response of Catamarans due to Wet Deck Slamming. (Dr.Ing. Thesis)
MTA-2002-158	Byklum, Eirik, MK	Nonlinear Shell Finite Elements for Ultimate Strength and Collapse Analysis of Ship Structures. (Dr.Ing. Thesis)
IMT-2003-1	Chen, Haibo, MK	Probabilistic Evaluation of FPSO-Tanker Collision in Tandem Offloading Operation. (Dr.Ing. Thesis)
IMT-2003-2	Skaugset, Kjetil Bjørn, MK	On the Suppression of Vortex Induced Vibrations of Circular Cylinders by Radial Water Jets. (Dr.Ing. Thesis)
IMT-2003-3	Chezhian, Muthu	Three-Dimensional Analysis of Slamming. (Dr.Ing. Thesis)
IMT-2003-4	Buhaug, Øyvind	Deposit Formation on Cylinder Liner Surfaces in Medium Speed Engines. (Dr.Ing. Thesis)
IMT-2003-5	Tregde, Vidar	Aspects of Ship Design: Optimization of Aft Hull with Inverse Geometry Design. (Dr.Ing. Thesis)
IMT-	Wist, Hanne Therese	Statistical Properties of Successive Ocean Wave

2003-6		Parameters. (Dr.Ing. Thesis)
IMT-2004-7	Ransau, Samuel	Numerical Methods for Flows with Evolving Interfaces. (Dr.Ing. Thesis)
IMT-2004-8	Soma, Torkel	Blue-Chip or Sub-Standard. A data interrogation approach of identity safety characteristics of shipping organization. (Dr.Ing. Thesis)
IMT-2004-9	Ersdal, Svein	An experimental study of hydrodynamic forces on cylinders and cables in near axial flow. (Dr.Ing. Thesis)
IMT-2005-10	Brodtkorb, Per Andreas	The Probability of Occurrence of Dangerous Wave Situations at Sea. (Dr.Ing. Thesis)
IMT-2005-11	Yttervik, Rune	Ocean current variability in relation to offshore engineering. (Dr.Ing. Thesis)
IMT-2005-12	Fredheim, Arne	Current Forces on Net-Structures. (Dr.Ing. Thesis)
IMT-2005-13	Heggernes, Kjetil	Flow around marine structures. (Dr.Ing. Thesis
IMT-2005-14	Fouques, Sebastien	Lagrangian Modelling of Ocean Surface Waves and Synthetic Aperture Radar Wave Measurements. (Dr.Ing. Thesis)
IMT-2006-15	Holm, Håvard	Numerical calculation of viscous free surface flow around marine structures. (Dr.Ing. Thesis)
IMT-2006-16	Bjørheim, Lars G.	Failure Assessment of Long Through Thickness Fatigue Cracks in Ship Hulls. (Dr.Ing. Thesis)
IMT-2006-17	Hansson, Lisbeth	Safety Management for Prevention of Occupational Accidents. (Dr.Ing. Thesis)
IMT-2006-18	Zhu, Xinying	Application of the CIP Method to Strongly Nonlinear Wave-Body Interaction Problems. (Dr.Ing. Thesis)
IMT-2006-19	Reite, Karl Johan	Modelling and Control of Trawl Systems. (Dr.Ing. Thesis)
IMT-2006-20	Smogeli, Øyvind Notland	Control of Marine Propellers. From Normal to Extreme Conditions. (Dr.Ing. Thesis)
IMT-2007-21	Storhaug, Gaute	Experimental Investigation of Wave Induced Vibrations and Their Effect on the Fatigue Loading of Ships. (Dr.Ing. Thesis)
IMT-2007-22	Sun, Hui	A Boundary Element Method Applied to Strongly Nonlinear Wave-Body Interaction Problems. (PhD Thesis, CeSOS)
IMT-2007-23	Rustad, Anne Marthine	Modelling and Control of Top Tensioned Risers. (PhD Thesis, CeSOS)
IMT-2007-24	Johansen, Vegar	Modelling flexible slender system for real-time simulations and control applications
IMT-2007-25	Wroldsen, Anders Sunde	Modelling and control of tensegrity structures.

		(PhD Thesis, CeSOS)
IMT-2007-26	Aronsen, Kristoffer Høye	An experimental investigation of in-line and combined inline and cross flow vortex induced vibrations. (Dr. avhandling, IMT)
IMT-2007-27	Gao, Zhen	Stochastic Response Analysis of Mooring Systems with Emphasis on Frequency-domain Analysis of Fatigue due to Wide-band Response Processes (PhD Thesis, CeSOS)
IMT-2007-28	Thorstensen, Tom Anders	Lifetime Profit Modelling of Ageing Systems Utilizing Information about Technical Condition. (Dr.ing. thesis, IMT)
IMT-2008-29	Refsnes, Jon Erling Gorset	Nonlinear Model-Based Control of Slender Body AUVs (PhD Thesis, IMT)
IMT-2008-30	Berntsen, Per Ivar B.	Structural Reliability Based Position Mooring. (PhD-Thesis, IMT)
IMT-2008-31	Ye, Naiquan	Fatigue Assessment of Aluminium Welded Box-stiffener Joints in Ships (Dr.ing. thesis, IMT)
IMT-2008-32	Radan, Damir	Integrated Control of Marine Electrical Power Systems. (PhD-Thesis, IMT)
IMT-2008-33	Thomassen, Paul	Methods for Dynamic Response Analysis and Fatigue Life Estimation of Floating Fish Cages. (Dr.ing. thesis, IMT)
IMT-2008-34	Pákozdi, Csaba	A Smoothed Particle Hydrodynamics Study of Two-dimensional Nonlinear Sloshing in Rectangular Tanks. (Dr.ing.thesis, IMT/ CeSOS)
IMT-2007-35	Grytøyr, Guttorm	A Higher-Order Boundary Element Method and Applications to Marine Hydrodynamics. (Dr.ing.thesis, IMT)
IMT-2008-36	Drummen, Ingo	Experimental and Numerical Investigation of Nonlinear Wave-Induced Load Effects in Containerships considering Hydroelasticity. (PhD thesis, CeSOS)
IMT-2008-37	Skejic, Renato	Maneuvering and Seakeeping of a Singel Ship and of Two Ships in Interaction. (PhD-Thesis, CeSOS)
IMT-2008-38	Harlem, Alf	An Age-Based Replacement Model for Repairable Systems with Attention to High-Speed Marine Diesel Engines. (PhD-Thesis, IMT)
IMT-2008-39	Alsos, Hagbart S.	Ship Grounding. Analysis of Ductile Fracture, Bottom Damage and Hull Girder Response. (PhD-thesis, IMT)
IMT-2008-40	Graczyk, Mateusz	Experimental Investigation of Sloshing Loading and Load Effects in Membrane LNG Tanks Subjected to Random Excitation. (PhD-thesis, CeSOS)
IMT-2008-41	Taghipour, Reza	Efficient Prediction of Dynamic Response for Flexible amd Multi-body Marine Structures. (PhD-

		thesis, CeSOS)
IMT-2008-42	Ruth, Eivind	Propulsion control and thrust allocation on marine vessels. (PhD thesis, CeSOS)
IMT-2008-43	Nystad, Bent Helge	Technical Condition Indexes and Remaining Useful Life of Aggregated Systems. PhD thesis, IMT
IMT-2008-44	Soni, Prashant Kumar	Hydrodynamic Coefficients for Vortex Induced Vibrations of Flexible Beams, PhD thesis, CeSOS
IMT-2009-45	Amlashi, Hadi K.K.	Ultimate Strength and Reliability-based Design of Ship Hulls with Emphasis on Combined Global and Local Loads. PhD Thesis, IMT
IMT-2009-46	Pedersen, Tom Arne	Bond Graph Modelling of Marine Power Systems. PhD Thesis, IMT
IMT-2009-47	Kristiansen, Trygve	Two-Dimensional Numerical and Experimental Studies of Piston-Mode Resonance. PhD-Thesis, CeSOS
IMT-2009-48	Ong, Muk Chen	Applications of a Standard High Reynolds Number Model and a Stochastic Scour Prediction Model for Marine Structures. PhD-thesis, IMT
IMT-2009-49	Hong, Lin	Simplified Analysis and Design of Ships subjected to Collision and Grounding. PhD-thesis, IMT
IMT-2009-50	Koushan, Kamran	Vortex Induced Vibrations of Free Span Pipelines, PhD thesis, IMT
IMT-2009-51	Korsvik, Jarl Eirik	Heuristic Methods for Ship Routing and Scheduling. PhD-thesis, IMT
IMT-2009-52	Lee, Jihoon	Experimental Investigation and Numerical in Analyzing the Ocean Current Displacement of Longlines. Ph.d.-Thesis, IMT.
IMT-2009-53	Vestbøstad, Tone Gran	A Numerical Study of Wave-in-Deck Impact usin a Two-Dimensional Constrained Interpolation Profile Method, Ph.d.thesis, CeSOS.
IMT-2009-54	Bruun, Kristine	Bond Graph Modelling of Fuel Cells for Marine Power Plants. Ph.d.-thesis, IMT
IMT 2009-55	Holstad, Anders	Numerical Investigation of Turbulence in a Sekwed Three-Dimensional Channel Flow, Ph.d.-thesis, IMT.
IMT 2009-56	Ayala-Uraga, Efren	Reliability-Based Assessment of Deteriorating Ship-shaped Offshore Structures, Ph.d.-thesis, IMT
IMT 2009-57	Kong, Xiangjun	A Numerical Study of a Damaged Ship in Beam Sea Waves. Ph.d.-thesis, IMT/CeSOS.
IMT 2010-58	Kristiansen, David	Wave Induced Effects on Floaters of Aquaculture Plants, Ph.d.-thesis, CeSOS.

IMT 2010-59	Ludvigsen, Martin	An ROV-Toolbox for Optical and Acoustic Scientific Seabed Investigation. Ph.d.-thesis IMT.
IMT 2010-60	Hals, Jørgen	Modelling and Phase Control of Wave-Energy Converters. Ph.d.thesis, CeSOS.
IMT 2010- 61	Shu, Zhi	Uncertainty Assessment of Wave Loads and Ultimate Strength of Tankers and Bulk Carriers in a Reliability Framework. Ph.d. Thesis, IMT/ CeSOS
IMT 2010-62	Shao, Yanlin	Numerical Potential-Flow Studies on Weakly-Nonlinear Wave-Body Interactions with/without Small Forward Speed, Ph.d.thesis,CeSOS.
IMT 2010-63	Califano, Andrea	Dynamic Loads on Marine Propellers due to Intermittent Ventilation. Ph.d.thesis, IMT.
IMT 2010-64	El Khoury, George	Numerical Simulations of Massively Separated Turbulent Flows, Ph.d.-thesis, IMT
IMT 2010-65	Seim, Knut Sponheim	Mixing Process in Dense Overflows with Emphasis on the Faroe Bank Channel Overflow. Ph.d.thesis, IMT
IMT 2010-66	Jia, Huirong	Structural Analysis of Intect and Damaged Ships in a Collission Risk Analysis Perspective. Ph.d.thesis CeSoS.
IMT 2010-67	Jiao, Linlin	Wave-Induced Effects on a Pontoon-type Very Large Floating Structures (VLFS). Ph.D.-thesis, CeSOS.
IMT 2010-68	Abrahamsen, Bjørn Christian	Sloshing Induced Tank Roof with Entrapped Air Pocket. Ph.d.thesis, CeSOS.
IMT 2011-69	Karimirad, Madjid	Stochastic Dynamic Response Analysis of Spar-Type Wind Turbines with Catenary or Taut Mooring Systems. Ph.d.-thesis, CeSOS.
IMT - 2011-70	Erlend Meland	Condition Monitoring of Safety Critical Valves. Ph.d.-thesis, IMT.
IMT – 2011-71	Yang, Limin	Stochastic Dynamic System Analysis of Wave Energy Converter with Hydraulic Power Take-Off, with Particular Reference to Wear Damage Analysis, Ph.d. Thesis, CeSOS.
IMT – 2011-72	Visscher, Jan	Application of Particla Image Velocimetry on Turbulent Marine Flows, Ph.d.Thesis, IMT.
IMT – 2011-73	Su, Biao	Numerical Predictions of Global and Local Ice Loads on Ships. Ph.d.Thesis, CeSOS.
IMT – 2011-74	Liu, Zhenhui	Analytical and Numerical Analysis of Iceberg Collision with Ship Structures. Ph.d.Thesis, IMT.
IMT – 2011-75	Aarsæther, Karl Gunnar	Modeling and Analysis of Ship Traffic by Observation and Numerical Simulation. Ph.d.Thesis, IMT.

Imt – 2011-76	Wu, Jie	Hydrodynamic Force Identification from Stochastic Vortex Induced Vibration Experiments with Slender Beams. Ph.d.Thesis, IMT.
Imt – 2011-77	Amini, Hamid	Azimuth Propulsors in Off-design Conditions. Ph.d.Thesis, IMT.
IMT – 2011-78	Nguyen, Tan-Hoi	Toward a System of Real-Time Prediction and Monitoring of Bottom Damage Conditions During Ship Grounding. Ph.d.thesis, IMT.
IMT- 2011-79	Tavakoli, Mohammad T.	Assessment of Oil Spill in Ship Collision and Grounding, Ph.d.thesis, IMT.
IMT- 2011-80	Guo, Bingjie	Numerical and Experimental Investigation of Added Resistance in Waves. Ph.d.Thesis, IMT.
IMT- 2011-81	Chen, Qiaofeng	Ultimate Strength of Aluminium Panels, considering HAZ Effects, IMT
IMT- 2012-82	Kota, Ravikiran S.	Wave Loads on Decks of Offshore Structures in Random Seas, CeSOS.
IMT- 2012-83	Sten, Ronny	Dynamic Simulation of Deep Water Drilling Risers with Heave Compensating System, IMT.
IMT- 2012-84	Berle, Øyvind	Risk and resilience in global maritime supply chains, IMT.
IMT- 2012-85	Fang, Shaoji	Fault Tolerant Position Mooring Control Based on Structural Reliability, CeSOS.
IMT- 2012-86	You, Jikun	Numerical studies on wave forces and moored ship motions in intermediate and shallow water, CeSOS.
IMT- 2012-87	Xiang ,Xu	Maneuvering of two interacting ships in waves, CeSOS
IMT- 2012-88	Dong, Wenbin	Time-domain fatigue response and reliability analysis of offshore wind turbines with emphasis on welded tubular joints and gear components, CeSOS
IMT- 2012-89	Zhu, Suji	Investigation of Wave-Induced Nonlinear Load Effects in Open Ships considering Hull Girder Vibrations in Bending and Torsion, CeSOS
IMT- 2012-90	Zhou, Li	Numerical and Experimental Investigation of Station-keeping in Level Ice, CeSOS
IMT- 2012-91	Ushakov, Sergey	Particulate matter emission characteristics from diesel enignes operating on conventional and alternative marine fuels, IMT
IMT- 2013-1	Yin, Decao	Experimental and Numerical Analysis of Combined In-line and Cross-flow Vortex Induced Vibrations, CeSOS

IMT-2013-2	Kurniawan, Adi	Modelling and geometry optimisation of wave energy converters, CeSOS
IMT-2013-3	Al Ryati, Nabil	Technical condition indexes doe auxiliary marine diesel engines, IMT
IMT-2013-4	Firoozkoohi, Reza	Experimental, numerical and analytical investigation of the effect of screens on sloshing, CeSOS
IMT-2013-5	Ommani, Babak	Potential-Flow Predictions of a Semi-Displacement Vessel Including Applications to Calm Water Broaching, CeSOS
IMT-2013-6	Xing, Yihan	Modelling and analysis of the gearbox in a floating spar-type wind turbine, CeSOS
IMT-7-2013	Balland, Océane	Optimization models for reducing air emissions from ships, IMT
IMT-8-2013	Yang, Dan	Transitional wake flow behind an inclined flat plate-----Computation and analysis, IMT
IMT-9-2013	Abdillah, Suyuthi	Prediction of Extreme Loads and Fatigue Damage for a Ship Hull due to Ice Action, IMT
IMT-10-2013	Ramìrez, Pedro Agustìn Pèrez	Ageing management and life extension of technical systems- Concepts and methods applied to oil and gas facilities, IMT
IMT-11-2013	Chuang, Zhenju	Experimental and Numerical Investigation of Speed Loss due to Seakeeping and Maneuvering. IMT
IMT-12-2013	Etemaddar, Mahmoud	Load and Response Analysis of Wind Turbines under Atmospheric Icing and Controller System Faults with Emphasis on Spar Type Floating Wind Turbines, IMT
IMT-13-2013	Lindstad, Haakon	Strategies and measures for reducing maritime CO2 emissons, IMT
IMT-14-2013	Haris, Sabril	Damage interaction analysis of ship collisions, IMT
IMT-15-2013	Shainee, Mohamed	Conceptual Design, Numerical and Experimental Investigation of a SPM Cage Concept for Offshore Mariculture, IMT
IMT-16-2013	Gansel, Lars	Flow past porous cylinders and effects of biofouling and fish behavior on the flow in and around Atlantic salmon net cages, IMT
IMT-17-2013	Gaspar, Henrique	Handling Aspects of Complexity in Conceptual Ship Design, IMT
IMT-18-2013	Thys, Maxime	Theoretical and Experimental Investigation of a Free Running Fishing Vessel at Small Frequency of Encounter, CeSOS
IMT-19-2013	Aglen, Ida	VIV in Free Spanning Pipelines, CeSOS

IMT-1-2014	Song, An	Theoretical and experimental studies of wave diffraction and radiation loads on a horizontally submerged perforated plate, CeSOS
IMT-2-2014	Rogne, Øyvind Ygre	Numerical and Experimental Investigation of a Hinged 5-body Wave Energy Converter, CeSOS
IMT-3-2014	Dai, Lijuan	Safe and efficient operation and maintenance of offshore wind farms ,IMT
IMT-4-2014	Bachynski, Erin Elizabeth	Design and Dynamic Analysis of Tension Leg Platform Wind Turbines, CeSOS
IMT-5-2014	Wang, Jingbo	Water Entry of Freefall Wedged – Wedge motions and Cavity Dynamics, CeSOS
IMT-6-2014	Kim, Ekaterina	Experimental and numerical studies related to the coupled behavior of ice mass and steel structures during accidental collisions, IMT
IMT-7-2014	Tan, Xiang	Numerical investigation of ship's continuous- mode icebreaking in leverl ice, CeSOS
IMT-8-2014	Muliawan, Made Jaya	Design and Analysis of Combined Floating Wave and Wind Power Facilities, with Emphasis on Extreme Load Effects of the Mooring System, CeSOS
IMT-9-2014	Jiang, Zhiyu	Long-term response analysis of wind turbines with an emphasis on fault and shutdown conditions, IMT
IMT-10-2014	Dukan, Fredrik	ROV Motion Control Systems, IMT
IMT-11-2014	Grimsmo, Nils I.	Dynamic simulations of hydraulic cylinder for heave compensation of deep water drilling risers, IMT
IMT-12-2014	Kvittem, Marit I.	Modelling and response analysis for fatigue design of a semisubmersible wind turbine, CeSOS
IMT-13-2014	Akhtar, Juned	The Effects of Human Fatigue on Risk at Sea, IMT
IMT-14-2014	Syahroni, Nur	Fatigue Assessment of Welded Joints Taking into Account Effects of Residual Stress, IMT
IMT-1-2015	Bøckmann, Eirik	Wave Propulsion of ships, IMT
IMT-2-2015	Wang, Kai	Modelling and dynamic analysis of a semi-submersible floating vertical axis wind turbine, CeSOS
IMT-3-2015	Fredriksen, Arnt Gunvald	A numerical and experimental study of a two-dimensional body with moonpool in waves and current, CeSOS
IMT-4-2015	Jose Patricio Gallardo Canabes	Numerical studies of viscous flow around bluff bodies, IMT

IMT-5-2015	Vegard Longva	Formulation and application of finite element techniques for slender marine structures subjected to contact interactions, IMT
IMT-6-2015	Jacobus De Vaal	Aerodynamic modelling of floating wind turbines, CeSOS
IMT-7-2015	Fachri Nasution	Fatigue Performance of Copper Power Conductors, IMT
IMT-8-2015	Oleh I Karpa	Development of bivariate extreme value distributions for applications in marine technology,CeSOS
IMT-9-2015	Daniel de Almeida Fernandes	An output feedback motion control system for ROVs, AMOS
IMT-10-2015	Bo Zhao	Particle Filter for Fault Diagnosis: Application to Dynamic Positioning Vessel and Underwater Robotics, CeSOS
IMT-11-2015	Wenting Zhu	Impact of emission allocation in maritime transportation, IMT
IMT-12-2015	Amir Rasekhi Nejad	Dynamic Analysis and Design of Gearboxes in Offshore Wind Turbines in a Structural Reliability Perspective, CeSOS
IMT-13-2015	Arturo Jesùs Ortega Malca	Dynamic Response of Flexibles Risers due to Unsteady Slug Flow, CeSOS
IMT-14-2015	Dagfinn Husjord	Guidance and decision-support system for safe navigation of ships operating in close proximity, IMT
IMT-15-2015	Anirban Bhattacharyya	Ducted Propellers: Behaviour in Waves and Scale Effects, IMT
IMT-16-2015	Qin Zhang	Image Processing for Ice Parameter Identification in Ice Management, IMT
IMT-1-2016	Vincentius Rumawas	Human Factors in Ship Design and Operation: An Experiential Learning, IMT
IMT-2-2016	Martin Storheim	Structural response in ship-platform and ship-ice collisions, IMT
IMT-3-2016	Mia Abrahamsen Prsic	Numerical Simulations of the Flow around single and Tandem Circular Cylinders Close to a Plane Wall, IMT
IMT-4-2016	Tufan Arslan	Large-eddy simulations of cross-flow around ship sections, IMT

IMT-5-2016	Pierre Yves-Henry	Parametrisation of aquatic vegetation in hydraulic and coastal research,IMT
IMT-6-2016	Lin Li	Dynamic Analysis of the Instalation of Monopiles for Offshore Wind Turbines, CeSOS
IMT-7-2016	Øivind Kåre Kjerstad	Dynamic Positioning of Marine Vessels in Ice, IMT
IMT-8-2016	Xiaopeng Wu	Numerical Analysis of Anchor Handling and Fish Trawling Operations in a Safety Perspective, CeSOS
IMT-9-2016	Zhengshun Cheng	Integrated Dynamic Analysis of Floating Vertical Axis Wind Turbines, CeSOS
IMT-10-2016	Ling Wan	Experimental and Numerical Study of a Combined Offshore Wind and Wave Energy Converter Concept
IMT-11-2016	Wei Chai	Stochastic dynamic analysis and reliability evaluation of the roll motion for ships in random seas, CeSOS
IMT-12-2016	Øyvind Selnes Patricksson	Decision support for conceptual ship design with focus on a changing life cycle and future uncertainty, IMT
IMT-13-2016	Mats Jørgen Thorsen	Time domain analysis of vortex-induced vibrations, IMT
IMT-14-2016	Edgar McGuinness	Safety in the Norwegian Fishing Fleet – Analysis and measures for improvement, IMT
IMT-15-2016	Sepideh Jafarzadeh	Energy effiency and emission abatement in the fishing fleet, IMT
IMT-16-2016	Wilson Ivan Guachamin Acero	Assessment of marine operations for offshore wind turbine installation with emphasis on response-based operational limits, IMT
IMT-17-2016	Mauro Candeloro	Tools and Methods for Autonomous Operations on Seabed and Water Coumn using Underwater Vehicles, IMT
IMT-18-2016	Valentin Chabaud	Real-Time Hybrid Model Testing of Floating Wind Tubines, IMT
IMT-1-2017	Mohammad Saud Afzal	Three-dimensional streaming in a sea bed boundary layer
IMT-2-2017	Peng Li	A Theoretical and Experimental Study of Wave-induced Hydroelastic Response of a Circular Floating Collar
IMT-3-2017	Martin Bergström	A simulation-based design method for arctic maritime transport systems

IMT-4-2017	Bhushan Taskar	The effect of waves on marine propellers and propulsion
IMT-5-2017	Mohsen Bardestani	A two-dimensional numerical and experimental study of a floater with net and sinker tube in waves and current
IMT-6-2017	Fatemeh Hoseini Dadmarzi	Direct Numerical Simualtion of turbulent wakes behind different plate configurations
IMT-7-2017	Michel R. Miyazaki	Modeling and control of hybrid marine power plants
IMT-8-2017	Giri Rajasekhar Gunnu	Safety and effiency enhancement of anchor handling operations with particular emphasis on the stability of anchor handling vessels
IMT-9-2017	Kevin Koosup Yum	Transient Performance and Emissions of a Turbocharged Diesel Engine for Marine Power Plants
IMT-10-2017	Zhaolong Yu	Hydrodynamic and structural aspects of ship collisions
IMT-11-2017	Martin Hassel	Risk Analysis and Modelling of Allisions between Passing Vessels and Offshore Installations
IMT-12-2017	Astrid H. Brodtkorb	Hybrid Control of Marine Vessels – Dynamic Positioning in Varying Conditions
IMT-13-2017	Kjersti Bruserud	Simultaneous stochastic model of waves and current for prediction of structural design loads
IMT-14-2017	Finn-Idar Grøtta Giske	Long-Term Extreme Response Analysis of Marine Structures Using Inverse Reliability Methods
IMT-15-2017	Stian Skjong	Modeling and Simulation of Maritime Systems and Operations for Virtual Prototyping using co-Simulations
IMT-1-2018	Yingguang Chu	Virtual Prototyping for Marine Crane Design and Operations
IMT-2-2018	Sergey Gavrilin	Validation of ship manoeuvring simulation models
IMT-3-2018	Jeevith Hegde	Tools and methods to manage risk in autonomous subsea inspection,maintenance and repair operations
IMT-4-2018	Ida M. Strand	Sea Loads on Closed Flexible Fish Cages
IMT-5-2018	Erlend Kvinge Jørgensen	Navigation and Control of Underwater Robotic Vehicles

IMT-6-2018	Bård Stovner	Aided Intertial Navigation of Underwater Vehicles
IMT-7-2018	Erlend Liavåg Grotle	Thermodynamic Response Enhanced by Sloshing in Marine LNG Fuel Tanks